Università degli Studi della Tuscia di Viterbo

Dipartimento di Economia, Ingegneria, Società e Impresa
Dipartimento di Scienze Agrarie e Forestali
Department of Economics, Engineering, Society, and Business
Department of Agricultural and Forestry Sciences

Ph.D. course | Dottorato di ricerca
Engineering for Energy and Environment - XXXVIII cycle

Spaceborne imaging spectroscopy as a tool for urban and regional planning and environmental monitoring

Settore scientifico-disciplinare AGRI-04/C

Ph.D. candidate:
Dott. Gabriele Delogu

Gabriele Delogu

Ph.D. coordinator:
Prof. Andrea L. Facci

Andrea L. Facci

Tutor:
Prof. Lorenzo Boccia

Lorenzo Boccia

A.Y. 2025/26

I hereby declare that the contents and organization of this dissertation constitute my own original work and does not compromise in any way the rights of third parties, including those relating to the security of personal data.

The text was produced with assistance from OpenAI's to check for grammatical correctness, improve clarity of sentences, and refine readability. No content was generated to replace the author's own ideas or arguments. The final responsibility for the content and its accuracy rests entirely with the author.

This declaration is made in accordance with the transparency obligations set out in the European Union's Artificial Intelligence Act.

Viterbo, Italy - November, 2025 Gabriele Delogu

«Un paese ci vuole, non fosse che per il gusto di andarsene via.
Un paese vuol dire non essere soli, sapere che nella gente, nelle piante, nella terra c'è qualcosa di tuo, che anche quando non ci sei resta ad aspettarti.»

Cesare Pavese, La luna e i falò, 1950

Acknowledgment

First and foremost, I wish to thank Professor A. L. Facci, Dean of the PhD program, for his support, and my Tutor, Professor L. Boccia, for his invaluable advice, encouragement, and continuous availability during these years. I am also deeply grateful to the PhD staff and to all my colleagues, whose support and companionship have been an essential part of this experience.

A special thanks goes to Miriam, Alessio, Eros and Cassandra, with whom I have shared not only scientific discussions but also memorable moments of friendship.

I gratefully acknowledge the member of the PRIN project, which funded my doctoral research, and in particular Professor M. N. Ripa and Professor F. Recanatesi for their collaboration and guidance within the project activities.

My sincere thanks also go to Professor D. Pflugmacher and Professor P. Hostert, who welcomed me at Humboldt University of Berlin during my research stay abroad. Their insights, expertise, and generosity have been an invaluable source of learning and inspiration.

Finally, I would like to thank the reviewers of this thesis for their constructive and valuable feedback, which helped to improve the final version of this work.

To all those who have accompanied me on this path, both professionally and personally, and especially to my family, I extend my heartfelt gratitude.

Abstract

Planning plays a central role in balancing human needs with ecological constraints, integrating environmental protection with socio-economic needs. The effectiveness of planning often depends on timely, reliable, and spatially detailed environmental information. In this context, remote sensing has emerged as a powerful ally, strengthening the planning process. This thesis explores the potential of spaceborne imaging spectroscopy to provide information that supports this process, focusing on data from the Italian hyperspectral mission PRISMA.

With reference to urban, agricultural, and forestry contexts the thesis addresses research questions concerning the discrimination of spectrally similar land cover types, the integration of spectral and spatial detail, the use of hyperspectral data for forest tree classification, and the generalization of classification models across a wide ecological gradient. The findings show that PRISMA data provides detailed information, allowing subtle differences between crops to be identified, supporting forest tree mapping, and improving the classification accuracy of tree species in urban context when combined with panchromatic data. Models trained across multiple sites demonstrated effective generalization, foreshadowing the potential of future hyperspectral missions for large-scale monitoring. Together, these results demonstrate how satellite imaging spectroscopy can support planning needs, from forest management to urban trees inventories and agricultural monitoring. At the same time, challenges persist. Mixed land covers remain difficult to classify, and reliable ground-truth data are often scarce. Meeting these challenges will require multi-temporal and multi-sensor approaches, advanced analytical techniques such as spectral unmixing, and new strategies for collaborative field data collection.

Overall, this thesis demonstrates that PRISMA has moved spaceborne hyperspectral remote sensing beyond experimental applications, showing its capacity to bridge the gap between research and practice. Spaceborne imaging spectroscopy emerges as a central component in the evolving landscape of Earth Observation, with the potential to address pressing environmental challenges and inform sustainable planning at multiple scales.

Table of Contents

Chapter 1

General Introduction

This opening chapter introduces the key concepts, objectives, and research questions of the thesis. The chapter begins by outlining the broader research context before presenting the fundamentals of remote sensing, including the basic of technology, the main characteristics of the remote sensing images, the extraction of information, and the role of reference datasets. Then, the chapter focuses on spaceborne imaging spectroscopy, highlighting the distinctive features of the PRISMA hyperspectral mission. After that, the chapter also discusses the function of planning processes and outlines some planning instruments that can benefit from satellite-based information. It concludes by clarifying the thesis aim and research questions, which are further explored in the following chapters.

1.1. Background and research context

Societies around the globe face urgent challenges due to climate change and accelerating environmental degradation. Rising temperatures, altered hydrological cycles, and biodiversity loss are already affecting ecosystems and natural resources, with risks expected to increase significantly in the coming decades (IPCC, 2023). According to the World Meteorological Organization (WMO), several global climate indicators continued to record highs in 2024, confirming the acceleration of climate change (WMO, 2024). For example, the concentration of carbon dioxide reached 420.0 ± 0.1 ppm, which is equivalent to 151% of pre-industrial levels and the global mean near-surface temperature increased by 1.55 ± 0.13 °C above the 1850–1900 baseline, making 2024 the warmest year in the 175-year observational record. These indicators – together with ocean heat content and pH, sea level, glacier mass, and sea-ice extent – hint at intensifying climate disturbances and illustrate the urgent need for comprehensive and systematic environmental monitoring. Moreover, environmental change and socioeconomic development are closely linked and require more robust data and knowledge systems to inform decision-making, as stated in the Global Environment Outlook of the United Nations Environment Programme (UNEP, 2019).

Achieving the global sustainable development goals of the 2030 Agenda requires accurate monitoring of land, water resources, forests, and urban environments (UN General Assembly, 2015). Reliable and spatially explicit information is necessary for planning and management under pressure vital resources, as highlighted in the *State of the World's Forests* and *State of the World's Land and Water Resources* reports by the Food and Agriculture Organization of the United Nations (FAO, 2024, 2021). The European Land Monitoring Service Copernicus explicitly links Earth observation to sustainability goals, highlighting a growing institutional demand for advanced remote sensing technologies to complement the national and regional data (Copernicus, 2023).

Large-scale availability of detailed and up-to-date Land Use (LU) and Land Cover (LC) information, supported by automated processes, can facilitate natural resource conservation and management (Malinowski et al., 2020). Furthermore, using Earth Observation (EO) satellite platform for resource management allows to monitor large areas while reducing per-unit costs (Landgrebe, 2002). This framework presents novel prospects for EO, enabled by cutting-edge spaceborne imaging spectrometers. Upcoming missions, such as CHIME from the European Space Agency (ESA) (Nieke et al., 2023), Surface Biology and Geology (SBG) from NASA (National Aeronautics and Space Administration) (NASA, 2019), and precursor missions, such as PRISMA (PRecursore IperSpettrale della Missione Applicativa - Hyperspectral Precursor of the Application Mission) from the Italian Space Agency (ASI) (Cogliati et al., 2021) and EnMAP (Environmental Mapping) from the German Aerospace Center (DLR) (Storch et al., 2023), are designed to deliver data at high spectral resolution. As detailed next, the wealth of information gathered in narrow intervals across a broad range of the electromagnetic spectrum unveils untapped potential for quantitative mapping of various elements, including vegetation, soil composition, and water quality (Guanter et al., 2015; Shaik et al., 2022). The convergence of multiple hyperspectral missions, as highlighted in Schiavon et al. (2023), will facilitate systematic, global environmental monitoring, which is crucial for informed regional planning and sustainable resource governance.

1.2. Fundamentals of Remote Sensing

One of the most widely adopted definitions of Remote Sensing (RS) is provided by Avery and Berlin (1992), who describe it as the acquisition of information about objects through the analysis of data collected by instruments that are not in direct contact with them. The process could be compared to human vision, where the eyes capture light and the brain processes it to derive knowledge about surrounding objects (Dainelli, 2011). Thus, RS includes a scene with the objects to be detected, a source of energy (typically electromagnetic radiation) and a sensor to record it, as well as methods and techniques to process and interpret the data (Gomarasca, 1997). RS technology allows to generate digital images from an overhead perspective to derive information about Earth's surfaces, using reflected or emitted electromagnetic radiation across the regions of the electromagnetic spectrum (Campbell and Wynne, 2011).

1.2.1. Basics of technology

The nuclear reactions in the Sun produce energy across the full electromagnetic spectrum, and large part of this radiation passes through the atmosphere and reaches the Earth's surface (Campbell and Wynne, 2011). The interaction of solar radiation with atmospheric constituents produces distinctive absorption features, while specific spectral intervals, known as atmospheric transmittance windows, permit energy to reach the Earth’s surface largely unaffected (Gomarasca, 2009; Richards and Jia, 2006). The transmission of electromagnetic radiation can be described as either waves (undulatory theory) or photons (quantum theory) (Dainelli, 2011). According to the wave theory, propagation occurs through sinusoidal variations of the electric field, which generate a time-varying magnetic field. These two fields are perpendicular to each other and to the direction of wave travel. The wavelength (λ), measured in micrometers (μm) or nanometers (nm), is the distance between successive maximum or minimum, while frequency (ν), measured in hertz (Hz), is the number of cycles that pass a point in the time unit (second). The complete range of electromagnetic radiation organized by wavelength and frequency forms the *electromagnetic spectrum*, which is divided for convenience into ranges named based on their source (e.g., gamma rays and X-rays), their extension (e.g., ultraviolet, visible, and infrared), or their application (e.g., radio waves) (Figure 1).

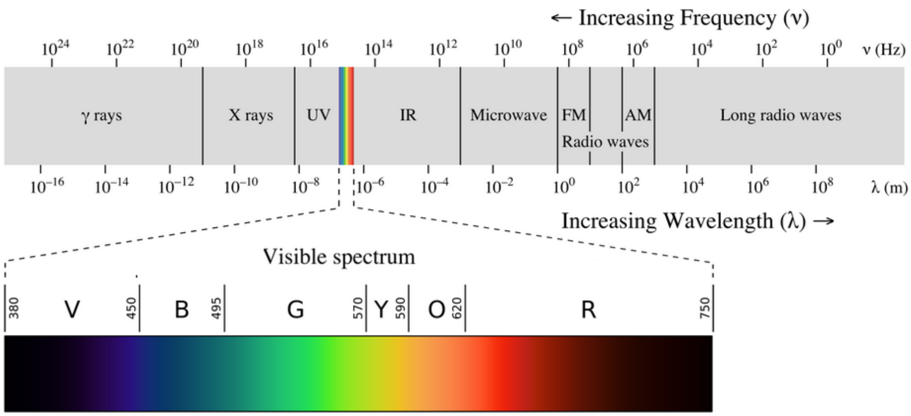

Figure 1: Ranges of the electromagnetic spectrum. Author: Philip Ronan Gringer, licensed under the Creative Commons. The original source has not been modified.

Remote sensing (RS) relies on physical laws that describe how electromagnetic radiation interacts with matter. According to *Kirchhoff's*, *Planck's* and *Stefan–Boltzmann's* laws, any surface with a temperature above absolute zero (>0 K) emits electromagnetic radiation and this emission is influenced by the surface's temperature, and its physical, chemical, and geometric properties, which determine whether the radiation is reflected (r), absorbed (a) and re-emitted, or transmitted (t) (Gomarasca, 1997, 2009). According to the *principle of energy conservation*, these three coefficients are linked by the equation $r+a+t=1$ and depend on the material and roughness of the surfaces and the wavelength (λ) considered (Brivio et al., 2006). *Wien*'s law further explains that the wavelength of maximum emission shifts with changes in temperature, indicating that as the temperature of a black body increases, the peak emission moves to shorter wavelengths (Campbell and Wynne, 2011). Based on these principles, different Earth surfaces exhibit distinct radiative behaviors depending on their material composition and temperature and consequently from the emissivity $\varepsilon(\lambda)$, which makes it possible to identify and distinguish objects through RS.

The purpose of RS is indeed to distinguish objects (e.g. soil, vegetation, water, etc.) on the ground by exploiting their different radiometric behavior at the different wavelengths at which the surfaces beneath can be detect by the sensor (Gomarasca, 1997). Mounted on UAV (unmanned aerial vehicle), aerial, or satellite platforms, the sensor measures the energy emitted by the Earth's surface, even beyond the visible range of the spectrum, and returns an image of the landscape below (Richards and Jia, 2006). This is particularly useful since an image can convey a large amount of information that can be interpreted by humans or computers (Campbell and Wynne, 2011). The radiation measured to form a digital image is referenced to a coordinate system, producing a function $f(x, y)$ which depends not only on the spatial coordinates (x, y) but also on wavelength (λ) at which the signals are recorded (Alparone et al., 2015). Indeed, acquiring measurements at multiple wavelengths across the spectrum enables the comparison and analysis of the behavior of detected objects, allowing them to be distinguished one from another. As stated in Parker & Wolff (1965) cited in (Campbell and Wynne, 2011), every object in nature exhibits a unique distribution of reflected, emitted, and absorbed radiation that can be used to differentiate between objects and infer their properties. This distribution, observed over a range of wavelengths, is referred to as a *spectral response pattern* or *spectral signature* (Campbell and Wynne, 2011). The spectral signature of an object with its radiation values at different wavelengths can be represented as a curve in a two-dimensional space, with wavelengths on the x-axis and observed values on the y-axis (Dainelli, 2011). Although spectral features can provide a basis for object identification, it is important to note that they are not static: spectral signatures vary over time and across space, e.g. the changing of agricultural crops throughout their growth cycle or the differences in the same tree species located in distinct forests (Campbell and Wynne, 2011).

The reflected and emitted radiation is measured using the *optical passive* sensors which use the Sun as input of the system (Richards and Jia, 2006), while *active* sensors like SAR (Synthetic-Aperture Radar) and LiDAR (Light Detection And Ranging) measure the artificial energy sources emitted by the RS platform itself (Campbell and Wynne, 2011). Optical sensors measure *radiance*, the radiant flux per unit area and solid angle measured on a plane perpendicular to the given direction, with units of measurement in Watts per square meter per steradian (Richards and Jia, 2006). The radiation measured by a sensor reflects the combined influence of surface properties, topography, illumination, and atmospheric effects (Alparone et al., 2015). The signal that reach the RS platform results from multiple components: the radiance reflected from the Earth's surface, which carries information about surfaces *reflectance*; solar radiation scattered directly to the sensor without reaching the surface; and radiation that is first scattered toward the ground, then reflected again through the atmosphere before being recorded (Campbell and Wynne, 2011). Thus, reflectance refers to the percentage of incident radiant energy reflected by a surface and depends on both the geometric structure of the surface and the physical and chemical properties of the material. Reflectance values can therefore only be measured after careful pre-processing of the digital image to remove atmospheric effects (Richards and Jia, 2006).

1.2.2. Data characteristics

The radiance (and reflectance) values acquired by the sensor are recorded as positive integer values called DN (*digital numbers*) (Gomarasca, 1997) and associated with discrete elements called *pixels* (picture elements) that, together, form a matrix that constitutes the digital image (or *raster*) (Campbell and Wynne, 2011). The characteristics of remote sensed digital images depend on the type of sensor and are linked to geometric, radiometric, spectral, and temporal resolutions (Brivio et al., 2006):

- The *geometric* (or *spatial*) *resolution* measures the minimum area on the ground, known as IFOV (instantaneous field of view), within which a single radiation value is detected and assigned to a pixel (Dainelli, 2011). The IFOV is the solid angle within which a sensor detects incoming radiation and refers to a single pixel. Meanwhile, the total angle of a scene is defined as field of view (FOV). The IFOV depends on the height of the RS platform, and spatial resolution differs for elements at different FOV positions; however, these differences are negligible for satellite platforms. (Alparone et al., 2015).
- The *Radiometric resolution* is defined as the minimum amount of radiation needed to activate the sensor and result in an electrical signal encoded as a DN (Gomarasca, 2009). The adopted binary encoding system determines the number of DNs values available

to represent the range of detected signals, and it is represented by 2^Q, where Q is the number of bits used for encoding (Dainelli, 2011). The number of bits determines the number of possible values for each pixel, which are then associated with a color scale for representation. The signal-to-noise ratio (SNR) affects radiometric resolution, as a higher SNR allows for a wider dynamic range. It can be improved either by reducing noise or by increasing the energy reaching the sensor; however, because the received energy decreases as spatial and spectral resolution increase, this creates a trade-off between resolution and SNR (Alparone et al., 2015).

- The *Spectral resolution* defines the sensitivity of the instrument to different wavelengths (λ) and their widths, such that each measured interval (*spectral band*) determines a DN value for the same pixel (Dainelli, 2011), i.e. the number of DN values for the same pixel equals the number of spectral bands. When data are recorded across a single spectral interval, usually the whole visible region and the first part of the infrared, the sensor used is called *Panchromatic* (Campbell and Wynne, 2011). While, when data are recorded across multiple bands (e.g., from 3 to 10), the sensor used is called *Multispectral* and provides information spanning the visible and near-infrared ranges, facilitating the differentiation of various surfaces (Govender et al., 2009). However, multispectral data are generally not contiguous along the spectrum and often have a bandwidth of 100–200 nm. When the number of bands exceeds ten, the term *Superspectral* is often used (Alparone et al., 2015). Finally, *Hyperspectral* is a term that refers to a data cube composed of hundreds of contiguous bands with narrow bandwidths ranging from ~1 to ~10 nm across a large portion of the spectrum (i.e., from the visible spectrum [0.4–0.7 nm] to the SWIR spectrum [2.4 nm]) (Thenkabail et al., 2015). Thus, hyperspectral data improves the distinction of surfaces with similar spectral characteristics (Rasti et al., 2020).

- The *Temporal resolution*, finally, refers to the time interval between two acquisitions in the same area. It is not affected by sensor characteristics, rather it is related to the revisit time of the RS platform (Dainelli, 2011), and is crucial in the case of multi-temporal analyses for time series generation, to detect changes on the ground over time (Campbell and Wynne, 2011).

1.2.3. Information extraction

RS data are stored as discrete values within the pixels of a digital image and these values must be transformed into information to support RS tasks such as: identifying objects and surfaces, describing processes, and monitoring changes. For example, one of the most common applications of RS data is the extraction of information to produce thematic maps of land use and land cover (Tassi and Vizzari, 2020). This process can be carried out through *photointerpretation*, which relies entirely on human expertise, or through *quantitative analysis* supported by computers (Richards and Jia, 2006). In the latter case, the process is commonly referred to as *classification* since it involves assigning each pixel to a class (Campbell and Wynne, 2011). Thus, raster classification is the process of extracting semantic information from raw data, i.e. pixel values by assigning each pixel to a class label (Jia, 2022; Sarath, 2014). While photointerpretation can be ambiguous and subjective, automatic classification is a defined, quantifiable, and repeatable process (Brivio et al., 2006). The classification process can be either *pixel-based*, in which the spectral similarities of pixels are determined using the spectral information stored in the image DNs, or *object-based*, in which the shape and texture features of the objects are used to define the pixels class, through a *segmentation* process that divides the image based on homogeneity and spatial contingency criteria (Gao and Mas, 2008). On the other hand, Depending on whether the user contributes by defining the real-world categories to which the image pixels are assigned or only by defining the number of classes to be used for the distribution of pixels, classification can be further divided into *supervised* or *unsupervised* (Dainelli, 2011). Supervised techniques use training data (also called *sample data*, *labelled data*, or *ground truths*) to derive spectral signatures, which are then applied to classify pixels into classes (Pfeifer et al., 2012; Tassi and Vizzari, 2020). Supervised approaches generally are preferred when classifying land cover but they require a sufficient number of accurate training samples (Jamali, 2019). Their effectiveness relies on the assumption that different land cover types exhibit distinct spectral reflectance behaviors (Townshend, 1994).

The level of detail RS data provides, which in turn affects the ability to distinguish between surfaces and objects on Earth, varies with different resolutions. High temporal resolution is recommended for multi-temporal analyses where multiple acquisitions are needed close together in time. High radiometric resolution offers greater sensitivity to spectral details and reduces the risk of image saturation, providing greater accuracy in quantitative analyses (e.g., vegetation indices, soil moisture, biomass), but it does not appear to affect the results so strongly (Miyoshi et al., 2018; Verde et al., 2018). High spatial resolution facilitates the recognition of shapes and textures (Gao and Mas, 2008), while high spectral resolution provides rich radiometric information that defines objects features (Pleniou and Koutsias, 2025; Thenkabail et al., 2004). As mentioned in the previous paragraph, however, as the amount of energy captured and recorded by the sensor depends on the IFOV, satellite systems face an inherent trade-off between spatial and spectral resolution (Alparone et al., 2015). Therefore, the choice between prioritizing spatial or spectral details depends on the application context. For instance, in urban environments with fine-grained heterogeneity, such as varying impervious surfaces, buildings, green spaces, and narrow streets, very high spatial resolution imagery (from 2 meters to decimeters) is essential for precise mapping (Hu et al., 2024; Nguyen-Van-Anh et al., 2021). Conversely, studies aimed at discriminating between spectrally similar vegetation types yield markedly better results using very high spectral resolution data, such as hyperspectral imaging (Goodenough et al., 2003; Vangi et al., 2021; Vanguri et al., 2024).

1.2.4. Reference datasets

The ability to extract reliable information from remotely sensed data is strongly dependent on the availability of field observations that serve as *reference datasets* (Stehman and Foody, 2019; Wu et al., 2019). These data are essential for both training models and validating results in supervised classification, but they also play a critical role to assess the reliability of analytical outputs when unsupervised techniques, photo interpretation, or raster algebra operations between remotely sensed data and spectral bands are used. Ground-based observations accuracy depends on both the calibration of the instruments employed and the thematic consistency of the survey with its objectives. Time is also a decisive factor in field data collection, as mismatches can substantially degrade confidence in results. The closer the survey is conducted to the acquisition of remote sensing data, the more accurate the results will be (Stehman and Foody, 2019; Wu et al., 2019). This synchronicity is particularly crucial when monitoring dynamic objects or phenomena that change rapidly over time. However, field surveys are resource-intensive, logistically demanding, and particularly difficult to conduct in remote or developing regions (Wu et al., 2019).

To address these limitations, new approaches such as *Mobile Crowd Sensing* have emerged (Ferster and Coops, 2016; Fritz et al., 2017; Kerrache et al., 2025). Considered a branch of citizen science, it is based on collaborative data collection using personal mobile devices, particularly smartphones, equipped with increasingly accurate sensors such as GPS and cameras (Ferster and Coops, 2016). This approach allows both expert and non-expert users—including professionals, scientists, and ordinary citizens—to contribute environmental observations (Martinez-Sanchez et al., 2024; van der Velde et al., 2023). Well-established database and applications such as *Flickr* or *iNaturalist* already facilitate this type of crowdsourcing (Li et al., 2013; Rapacciuolo et al., 2021), while new tools, specifically designed for collecting field data helpful for analyzing remotely sensed data, are being developed in academic contexts. For example, *Eye-Land* application (EyeLand App, 2024) created within the Italian project of relevant national interest «*Eye-Land: a crowd-sensing geospatial database for the monitoring of rural areas*», enables users to collect geo-tagged photos and attributes through an extremely simple user interfaces. In the pilot version the users can collect a variety of data about land cover, rural infrastructure, and environmental features by forming networks of volunteer collaborators.

Integrating observations from official sources with those derived from mobile crowd sensing, through user-friendly interfaces and applications that reduce barriers to participation, expands the amount of reference data available. With appropriate preprocessing, such integrated datasets can significantly enhance the potential of remote sensing, supporting both traditional multispectral platforms and newer hyperspectral sensors (Ferster and Coops, 2016; Kosmala et al., 2016).

1.3. Spaceborne imaging spectroscopy

RS technology has evolved rapidly over the years, providing increasingly high-quality data through the improvement of spatial, spectral, radiometric, and temporal resolution (Pandey et al., 2020). However, despite the advantages of very high spectral resolution data, the spaceborne imaging spectroscopy evolution has been fairly slow compared to multispectral satellites, largely due to the challenges of storing and transmitting the huge volumes of data generated by hyperspectral sensors (Filchev, 2014). Even though hyperspectral data from aircraft has been in development since the 1980s, only at the beginning of this century the first hyperspectral satellite mission provided data for civil and scientific purposes (Filchev, 2014). Compared to aircraft (and UAV), satellite data offers superior cost-efficiency, vast-area coverage, frequent systematic acquisitions, operational autonomy, data consistency, and extensive archives, making it a highly effective tool for large-scale, long-term environmental monitoring and planning (Matese et al., 2015; Müllerová et al., 2017; Sozzi et al., 2021). The pioneering Hyperion imaging spectrometer from NASA was among the first instrument to provide satellite data with extremely high spectral resolution, prompting discussions about spaceborne imaging spectrometer at the beginning of the new millennium (Ungar et al., 2003).

The *imaging spectrometry* or *spectroscopy* or *hyperspectral imaging* allows the acquisition of multiple contiguous spectral bands creating multiple spatially co-registered images (Filchev, 2014). Combining classic spectroscopy technology, which investigates material composition by analyzing light-matter interactions, with modern imaging systems allows us to measure a spectrum for each pixel in an image (Qian, 2021). Imaging spectroscopy typically covers wavelengths of the electromagnetic spectrum from 380 to 2500 nm, thus including the visible (400-700 nm), near-infrared (NIR), and SWIR through hundreds of spectral channels (even over 200) with a very narrow bandwidth (5-10 nm) (Hong et al., 2025). Thus, hyperspectral data displayed as a cube with two spatial dimensions (x, y) and one spectral dimension (z) contains a spectrum for each pixel, providing a unique spectral signature of the materials in the scene, enabling precise identification of objects and surfaces (Campbell and Wynne, 2011; Hong et al., 2025). The spectrum contained in a pixel is similar to that acquired in a laboratory with a spectrometer and allows the definition of unique "*fingerprints*" for the surface materials under investigation for various applications (e.g., agricultural, forestry, geological, environmental, etc.), guaranteeing results unobtainable with multispectral data (Filchev, 2014; Qian, 2021).

However, the processing of hyperspectral data is challenging due to its inherently high dimensionality, which hinders the analysis and characterization of the observed objects (Hong et al., 2025, 2019). Reducing data size by eliminating redundant information is achieved through techniques such as principal component analysis (PCA) (Jolliffe, 1986) or band selection (Sawant and Prabukumar, 2020). This is a necessary step to reduce the so-called Hughes phenomenon (i.e., to maintain the accuracy of a classifier, the number of training pixels per class needs to increase as the dimensionality of the data increases) (Alonso et al., 2011; Richards and Jia, 2006). Spectral unmixing techniques are used instead to manage the spectral mixture resulting from spatial resolution, and these techniques involve the identification of endmembers and their fractional abundances within mixed pixels (Palsson et al., 2018; Sánchez and Plaza, 2014). The growing interest in spaceborne imaging spectroscopy has led to recent exploratory missions, such as PRISMA and EnMAP (Cogliati et al., 2021; Storch et al., 2023), which enable further research into these hyperspectral satellite data handling techniques and allows innovative applications in RS (Shaik et al., 2023). These missions are equipped with innovative technologies and sampling capabilities that were not available with the Hyperion sensor (Ustin and Middleton, 2024). PRISMA and EnMAP are pioneering missions paving the way for a new era of hyperspectral satellites for global monitoring (Ustin and Middleton, 2024), anticipating the benefits of future long-term space spectroscopy missions such as CHIME (Copernicus Hyperspectral Imaging Mission) from ESA (European Space Agency) (Nieke et al., 2023) and Surface Biology and Geology from NASA (NASA, 2019).

1.3.1. PRISMA hyperspectral mission

The PRISMA mission is one of the major investments that ASI has made in EO through the use of optical sensors (Loizzo et al., 2018). The satellite platform was placed in orbit on March 22, 2019, and has been operational since January 2020 (Caporusso et al., 2020). The mission provides (on demand) hyperspectral and panchromatic images of the Earth's surface by combining a hyperspectral sensor with a medium-resolution panchromatic camera, allowing innovative remote sensing applications to be tested in resource management, environmental monitoring, and disaster management (Guarini et al., 2018; Loizzo et al., 2018). Indeed, the mission data in these early years has already been used, for example, to forest studies (Gasparini et al., 2024; Vangi et al., 2021); non-photosynthetic vegetation detection and classification (Pepe et al., 2020); geological applications (Tripathi and Garg, 2021); fire fuel detection (Shaik et al., 2022); crop type mapping (Spiller et al., 2021); crop trait identification (Tagliabue et al., 2022); local climate zone mapping (Vavassori et al., 2024), etc.

The PRISMA platform is equipped with an electro-optical instrument that integrates a high spectral resolution spectrometer with a medium spatial resolution panchromatic camera; the PAN/HYP payload employs a pushbroom scanning system (Caporusso et al., 2020). According to the technical documentation (PRISMA, 2020), the PRISMA hyperspectral cube consists of 240 bands, each with a bandwidth of 12 nm or less. These bands span the visible/near-infrared (VNIR) spectrum (400–1010 nm) and the shortwave infrared (SWIR) spectrum (920–2505 nm). The VNIR and SWIR channels overlap between 920 and 1,010 nm to allow better reconstruction of each pixel's spectral signature (Galeazzi et al., 2013). The panchromatic camera ranges from 400 to 700 nm. The swath width at nadir is 30 kilometers, the ground sampling distance (GSD) is 30 meters for the hyperspectral bands and 5 meters for the panchromatic band. The satellite operates operate in a Sun synchronous low Earth orbit with a nominal orbit of 615 km of mean altitude. The radiometric resolution is 12 bits. The temporal resolution implies a re-look time < 7 days (response time < 14 days; revisit time < 29 days) (Caporusso et al., 2020). The data acquisition from PRISMA mission can be requested from the ASI portal (www.prisma.asi.it) after user registration.

The PRISMA products are provided at different levels: Level 0 (L0) (raw data with ancillary satellite instruments data); Level 1 (L1) (top-of-atmosphere (TOA) radiance images, radiometrically corrected and calibrated in physical units); Level 2b (L2b), (spectral radiance transformed into geophysical parameters, geolocated and geocoded at the bottom of the atmosphere); Level 2c (L2c) (geolocated reflectance images at bottom-of-atmosphere; Angstrom correction is applied); Level 2d (L2d) (geocoded version of L2c; images are orthorectified using a DEM). It is important to note that the orthorectification process is done by ASI using the "SRTM90_CGIAR_4.1" DEM (Farr et al., 2007) and the geolocation accuracy may vary up to 200 m within the same scene and between different acquisitions (Baiocchi et al., 2022; De Luca et al., 2024).

The mission was expected to last five years (Loizzo et al., 2018). During the first years of activity, scientific studies in various fields highlighted the opportunities and weaknesses of the PRISMA mission and hyperspectral data in general. (Shaik et al., 2023). Opportunities include, among others, experimenting with satellite spectrometry applications for future operational missions and combining hyperspectral data with co-registered panchromatic or multispectral data from the Sentinel and Landsat missions. However, it is worth noting some weaknesses, such as the presence of bands with a very low SNR, insufficient acquisition frequency in the same area for vegetation phenology studies, and uncertainty in data acquisition scheduling, which does not guarantee satellite data acquisition and does not allow for simultaneous field data collection, especially for rapidly evolving objects (e.g., temporary agricultural crops).

1.4. Planning process

Planning is a cornerstone of sustainable societal development, as it provides a structured framework for balancing human needs with environmental constraints and ensuring long-term resilience in the face of uncertainty (Friedmann, 1998). By anticipating future challenges and coordinating present actions, planning enables the efficient allocation of resources, equitable access to services, and the adaptability of communities to social and environmental change (Davoudi, 2006). Regional and urban planners play a central role in this process: they mediate between economic growth, social equity, and environmental protection, translating broad sustainability goals into concrete land-use policies and spatial strategies (Campbell, 1996). Beyond its technical dimension, planning is also a normative and participatory process, shaping how societies envision their futures and negotiate trade-offs between competing interests (Healey, 1997). In this sense, planners are not merely technicians but stewards of collective well-being, tasked with guiding transitions toward more sustainable, livable, and inclusive environments (Albrechts, 2004).

Effective regional and urban planning hinges on integrating environmental sustainability with socio-economic development, taking into account the ecosystem carrying capacity (Leone, 2019). Forest and agricultural landscapes, together with urban green spaces, play a crucial role in delivering multiple ecosystem services, providing essential benefits for both the environment and human well-being. Forest and agricultural areas play multifunctional roles (e.g., as ecological buffers, biodiversity reservoirs, and livelihood bases) while urban green spaces enhance climate regulation, recreational access, and public well-being. For instance, multifunctional green infrastructure at urban and regional scales supports carbon sequestration, reduces urban heat, improves water regulation, and fosters social cohesion and health benefits (Goodspeed et al., 2022). Planning in these contexts must therefore be grounded in a nuanced understanding of ecosystem dynamics and land-use interdependencies, ensuring that natural and built environments co-evolve sustainably.

Remote sensing technologies have emerged as innovative tools in this planning paradigm. At regional level, satellite time series capture long-term land degradation, vegetation dynamics, and agricultural shifts providing critical data for evidence-based decision-making (Gabriele et al., 2023). In urban settings, Remote Sensing enable precise mapping of urban forests, green spaces, and thermal environments, crucial for tackling urban heat islands and for informed green infrastructure design (Li et al., 2019). The fusion of remote sensing with GIS (Geographic Information Systems) further empowers planners to model land-use scenarios, predict environmental outcomes, and optimize green infrastructure placement in alignment with socio-ecological priorities (Di Palma et al., 2024). In summary, remote sensing fills critical information gaps, offering scalable, repeatable, and high-resolution data across forest, agricultural, and urban green systems. Whether it is tracking land use in rural landscapes or guiding urban green space policies, the planning process could benefit from integrating remote sensing data. Integrating this data with GIS allows planners to simulate scenarios over wide areas, making the planning process more objective (Pelorosso et al., 2009).

1.4.1. Overview of the Italian Planning Instruments

The Italian planning system is historically rooted in the 1942 national planning fundamental law (*Legge urbanistica fondamentale*) (Law no. 1150, 1942), which established a hierarchical framework of instruments on three levels: broad strategic plans (*Piani Territoriali di Coordinamento*), general land-use plans (*Piani Comunali Generali*), and detailed operational plans (*Piani Particolareggiati*). Over the decades, this structure has been complemented by subsequent reforms that progressively integrated environmental considerations. A decisive step was represented by the (Law no. 431, 1985) (also known as *Legge Galasso*), which introduced mandatory landscape plans (*Piani Paesaggistici*) focused on safeguarding landscape values beyond their mere aesthetic dimension, linking cultural heritage with ecological protection. Additional changes occur in the early nineties with the (Law no. 142, 1990) on local authorities, which introduced the new province administrative level, and with the introduction of the new urban planning instruments (*Programmi complessi*), intended to compensate for the lack of suitable tools mainly aimed at managing the redevelopment of abandoned industrial structures and at the regeneration working-class suburbs (Leone, 2019). Further innovation of the planning tools and processes followed by the Italian Constitution reform in 2001 (Italian Constitution, Article 117, 2001), and the emanation of the Italian code of cultural heritage and landscape (Legislative Decree no. 42, 2004). The constitutional reform introduced in Article 117 the broader concept of territorial government (*Governo del territorio*), establishing it as a concurrent legislative matter between the State and the Regions and encompassing urbanism, soil defense, landscape protection, and environmental assessment (Gabriele et al., 2023). The code of cultural heritage and landscape establishes the primacy of landscape plans over other planning instruments and strengthens the role of the State in defining the principles of planning. However, beyond planning levels and specific or general objectives, the number of plans is not pre-determined and vary according to the needs and evolution of societies (Leone, 2019).

1.4.2. Sectorial Plans

Within the multi-level, multi-objective framework introduced above, territorial governance in Italy relies on a set of plans that address broader regional and landscape management objectives, as well as the specific requirements of agricultural, forestry, and urban green systems. These instruments, though sectorial in scope, are increasingly interlinked through the integration of spatial, ecological, and socio-economic data, forming a comprehensive basis for sustainable land-use planning and environmental policy. Altogether, this interconnected system of agricultural, forestry, and urban green planning plans supports the construction of a multifunctional, and ecologically coherent territorial structure, consistent with the objectives of sustainable development and climate adaptation promoted at the European and national levels. Based on different hierarchical levels and planning sectors, a variety of instruments impact land-use planning, landscape, and environmental protection, in particular:

- In rural territories, the Regional Agricultural Plan (*Piano Agricolo Regionale*) represents a central tool for coordinating agricultural development within the broader strategies of territorial governance. It promotes rural resilience and multifunctionality, supporting landscape preservation and the diversification of rural economies beyond strictly productive purposes. Furthermore, the accurate classification and mapping of crops provide an essential knowledge for informed planning process, supporting e.g., the territorialization for the Rural Development Programs (*Programmi di Sviluppo Rurale*), and facilitating the rational management of water resources and agrochemical inputs. As already shown (Leone et al., 2008), the environmental impacts of fertilizers and pesticides are highly variable across territories, reinforcing the importance of geographically differentiated planning information to ensure the sustainability of agricultural systems.
- Complementary to agricultural planning, forest management plays a fundamental role in maintaining ecological integrity and

landscape functionality. The Territorial Forestry Plan (*Piano Forestale di Indirizzo Territoriale*) (Legislative Decree no. 34, 2018) regulates forest resources and coordinates forest management across homogeneous ecological and socio-economic zones. Through the classification of tree species and forest types, it becomes possible to monitor forest distribution, identify conservation priorities, and design targeted interventions, such as reforestation, habitat restoration, or the management of protected areas. These activities not only safeguard biodiversity but also contribute to climate change mitigation and adaptation, aligning with broader international and national environmental objectives.

- At the urban scale, the focus shifts toward the management of green infrastructure as a crucial component of urban resilience and environmental quality. The General Urban Plan (*Piano Regolatore Generale*, also called *Piano Urbanistico Comunale* or *Piano di Governo del Territorio* in some Italian regions) remains the cornerstone of city planning (Gabellini, 2001), regulating zoning, public green spaces, and minimum environmental standards per inhabitant (Ministerial Decree no. 1444, 1968). In parallel, some operational plans, regulations and complementary tools deals specifically with vegetated areas and ecological corridors within urban settlements. For example, Urban Green Space Plans (*Piani del Verde Urbano*) (Law no. 10, 2013), municipal green regulations, and urban sustainable mobility plans (*Piani Urbano della Mobilità Sostenibile*) emphasize the integration of ecological infrastructure into cities and link green networks with pedestrian and cycling corridors (Ministerial Decree no. 397, 2017). In this case, the classification and monitoring of urban tree species facilitate the optimization of green area distribution, improvement of air quality, reduction of heat islands, and prevention of risks associated with extreme meteorological events, while also supporting the maintenance and renewal of urban vegetation, assisting administrations in complying with national and international regulations.

- At regional and landscape-level the Regional Territorial Plan (*Piano Territoriale Regionale*), expected by the introduction of "territorial government" as a concurrent legislative matter between the State and the Regions (Italian Constitution, Article 117, 2001), and the Landscape Regional Plan (*Piano Paesaggistico Regionale*) (Legislative Decree no. 42, 2004), define the broader strategies that guide and harmonize the specific ecological, agricultural, forestry and urban green areas objectives and actions described above. At wide area scale, also the Park Plan (*Piano per il Parco*), established under the national law on protected areas (Law no. 194, 1991), represent a pivotal tool defining zoning and management strategies for parks and reserves, reinforcing the connection between biodiversity conservation and spatial planning. The analytical foundation for landscape and environmental planning is provided by the information on land-use and vegetation data that is often managed through geographic information systems fed with the quantitative analysis of Remote Sensing data. This knowledge enables the design of ecological networks and the management of *Natura 2000* sites (*Habitats Directive - 92/43/EEC*, 1992). Moreover, such planning approaches contribute to hydrogeological risk prevention since land use and soil management represent key determinants of territorial vulnerability (Leone et al., 2019).

1.4.3. The Role of Remote Sensing

The planning process involves a systemic analysis of the territorial structure (*cognitive phase*), followed by the identification of strategic objectives, stakeholders, and timelines (*prognostic phase*), and the drafting of operational tools for implementation (Petroncelli, 2005). Each planning instrument consists of various prescriptive, descriptive, or managerial documents, which are generally supported by thematic maps showing the current situation and plan forecasts. The approval process may vary depending on the type of planning tool and level of planning. In any case, remote sensing technology can play a fundamental role in supporting the planning process by aiding in the preparation of documentation and monitoring the effectiveness of the plan. Remote sensing data provide reliable, up-to-date information on land cover, vegetation health, soil conditions, and urban expansion, offering an essential evidence base for identifying challenges and opportunities (De Toni et al., 2023; Di Palma et al., 2024; Fichera et al., 2011; Santarsiero et al., 2022). The time-series analysis and spatial modeling allows planners to forecast the policy and climate impacts on agricultural productivity (Satalino et al., 2024; Sciortino et al., 2020), forest vulnerability (Recanatesi et al., 2020), or urban green spaces benefits (Shahtahmassebi et al., 2021). Finally, remote sensing facilitates the evaluation of plan effectiveness by tracking land-use changes, compliance with environmental standards, and the long-term evolution of green infrastructure (Fuentes et al., 2021; Recanatesi et al., 2019; Telesca et al., 2023).

The availability of high-resolution multispectral and hyperspectral satellite missions could significantly improve the preparation of the graphical and technical documents needed for planning instruments. Satellite data from missions like PRISMA could be extremely useful when preparing the documentation of the aforementioned Sectorial Plans. In particular:

- In the case of Regional Agricultural Plans and Rural Development Programs, integrating Sentinel and PRISMA data enables the creation of high-quality crop and land use maps at a fine scale with detailed legends, which are essential for producing the Land Use Map (*Carta d'uso del suolo*) and other thematic maps of agricultural suitability, as well as for verifying and monitoring environmental measures. Furthermore, hyperspectral imagery plays a decisive role in mapping soil properties, discriminating crop species, and detecting water or nutrient stress early on. This information feeds into analyses of territorial vulnerability and the reporting documents required during implementation and ex-post evaluation.

- Regarding the Territorial Forestry Plan, satellite-based data enables mapping of vegetation composition and structure, which strengthens the Map of Forest stands (*Carta dei soprassuoli forestali*), by including dominant species, canopy cover, vertical stratification, and fuel load distribution. Time-series analysis enhances risk maps, such as those depicting fire susceptibility, post-disturbance severity, or erosion potential. Hyperspectral satellite data support tree health diagnostics, biotic stress detection, and estimation of forest biomass and carbon stock if combined with active sensors, thereby improving both the National Forestry Inventory (*Inventario forestale nazionale*) and the multi-year management program (*Piano di gestione forestale* o *Piano di assestamento forestale*).
- Urban Green Plans require detailed and continuously updated spatial knowledge on ecological assets. Combining hyperspectral satellite data with very high-resolution multispectral data allows for the automatic delineation of tree crowns, classification of species, and quantification of leaf area, which supports the Inventory of Street Trees (*Inventario delle alberature stradali*) and Maps of public green spaces (*Mappa delle aree verdi*). Moreover, Urban Heat Island maps (*Mappe del microclima urbano*), surface permeability maps (*Mappa delle superfici permeabili*) and climate-regulation ecosystem service assessments derived from thermal and spectral measurements provide information to the Green Management Plan (*Piano di gestione del verde*).
- Wide-area instruments for environmental conservation, including Park Management Plans and Natura 2000 Management Plans, rely

on accurate and periodically updated Habitat Maps (*Cartografia degli habitat e delle specie*), zonation maps (*Mappe di zonizzazione*), pressure and threat maps (*Mappe delle pressioni e minacce*), and constraint and hazard maps (*Mappe di vincolo e pericolo*). Hyperspectral satellite data, thanks to their fine spectral response, facilitate the identification of habitat types, mapping of species of conservation interest, and monitoring of invasive species expansion. Additionally, radar–optical integration improves the detection of hydrological alterations, wetland dynamics, and ground deformation, crucial for the Assessment Studies (*Valutazioni di incidenza*) and monitoring indicators (*Report di monitoraggio ambientale*) established by conservation authorities.

Beyond technical documentation support, remote sensing data strengthens the transparency, efficiency, and adaptability of the Italian planning framework, ensuring that territorial policies are grounded in systematic and reproducible data. Nevertheless, the utilization of remotely sensed data in planning is frequently constrained by the availability of free and continuous distributions, or adequate spatial and/or spectral resolution which impacts the application in contexts necessitating detailed thematic information extraction.

1.5. Aim and research questions

This thesis investigates the potential of spaceborne imaging spectroscopy to support planning processes, building on (1) the societal challenges outlined in Section 1.1, (2) the advantages of remote sensing and hyperspectral data discussed in Sections 1.2 and 1.3, and (3) the integration of such data into planning tools (Section 1.4). The research is guided by a set of questions that highlight both the opportunities and limitations of applying hyperspectral data from the PRISMA mission in real-world contexts.

The first research question examines the ability of hyperspectral sensors to discriminate between land cover types with highly similar spectral signatures, such as different categories of permanent crops. This raises the broader issue of whether the fine spectral resolution of imaging spectroscopy can reliably capture subtle differences in highly fragmented landscapes. Here is included a comparison of different classification algorithms and is assessed what strategies are most effective for handling the challenges of high-dimensional data.

The second research question focuses on the integration of spatial and spectral information, specifically whether enhancing PRISMA hyperspectral imagery with the finer-resolution panchromatic band can improve classification accuracy. A simple pansharpening method is tested to assess its ability to deliver more accurate and actionable information, particularly for municipalities facing policy and management demands about green infrastructures. This approach also explores the potential for applying PRISMA data in urban areas, where accurate mapping of features such as urban trees is essential.

The third research question considers the contribution of hyperspectral data to forest management and monitoring. It investigates whether spaceborne imaging spectroscopy can provide sufficient detail for meaningful classification at the forest-type or even tree-species level, despite the relatively coarse GSD of hyperspectral satellites. This leads to a broader reflection on the trade-off between spectral richness and spatial resolution, and its implications for supporting forest inventories and biodiversity assessments in heterogeneous forest environments.

Finally, the thesis addresses the challenge of model generalization. It asks to what extent predictive models for forest species classification can be transferred across wide ecological gradients under varying environmental conditions. A comparative analysis is also carried out to evaluate PRISMA against multispectral time series from current missions, as well as against forthcoming super-resolution satellite systems. Collectively, the model generalization capabilities and the multi-sensors comparison aim to clarify both the current potential of hyperspectral missions and their role within the rapidly evolving field of Earth Observation technologies.

1.6. Thesis outline

Following the introduction chapter, the thesis is structured into four chapters, each addressing one of the research questions outlined above, and concludes with a synthesis of the main findings and future perspectives.

Chapter 2 investigates the potential of PRISMA data to discriminate ten classes of permanent agricultural crops with similar spectral characteristics, alongside some common land-cover types. To this end, three hyperspectral cubes with varying numbers of bands were tested, and the performances of a Random Forest classifier, an artificial neural network, and a convolutional neural network were compared. The case study covers an entire PRISMA scene of about 900 km^2, primarily located in the province of Caserta, Italy.

Chapter 3 examines how improving the spatial resolution of PRISMA data affects its use in urban settings. Through a case study on the municipality of Naples, Italy, the study compares the classification accuracy of five tree species using the original GDS data against the results obtained after applying pansharpening with the co-registered panchromatic band.

Chapter 4 evaluates the capacity of hyperspectral data to support tree forest classification in a highly biodiverse environment. The analysis focuses on six tree classes based on dominant tree species, assessing the accuracy levels achievable in a heterogeneous forest area mainly corresponding to the Serre Regional Park, Italy.

Chapter 5 addresses the challenge of model generalization across a wide ecological gradient. Single results from six study areas distributed from northern to southern Italy were compared with those obtained from jointly trained models using data from all sites. The chapter also compares PRISMA-based classifications with results from Sentinel-2 (single acquisitions and time series) and simulated data from the forthcoming Landsat Next mission.

The final chapter (Chapter 6) summarizes the key findings from the case studies, discusses the strengths and limitations of spaceborne imaging spectroscopy, and outlines possible directions for future research.

Chapter 2

Using PRISMA hyperspectral data for land cover classification with artificial intelligence support

Gabriele Delogu, Eros Caputi, Miriam Perretta, Maria Nicolina Ripa, Lorenzo Boccia

Published in Sustainability **2023**, 15, 13786.
https://doi.org/10.3390/su151813786

Abstract

Hyperspectral satellite missions, such as PRISMA of the Italian Space Agency (ASI), have opened up new research opportunities. Using PRISMA data in land cover classification has yet to be fully explored, and it is the main focus of this paper. Historically, the main purposes of remote sensing have been to identify land cover types, to detect changes, and to determine the vegetation status of forest canopies or agricultural crops. The ability to achieve these goals can be improved by increasing spectral resolution. At the same time, improved AI algorithms open up new classification possibilities. This paper compares three supervised classification techniques for agricultural crop recognition using PRISMA data: random forest, artificial neural network, and convolutional neural network. The study was carried out over an area of 900 km2 in the province of Caserta, Italy. The PRISMA HDF5 file, pre-processed by the ASI at the reflectance level (L2d), was converted to GeoTiff using a custom Python script to facilitate its management in Qgis. The Qgis plugin AVHYAS was used for classification tests. The results show that CNN gives better results in terms of overall accuracy (0.973), K coefficient (0.968), and F1 score (0.842).

2.1. Introduction

The potential for Earth observation (EO) from space for resource management and optimization emerged in the early 1960s and throughout the 20th century, with the advent of digital computers, pattern-recognition technology, and the first artificial satellites. The ability to monitor large areas, while reducing per-unit costs, is one of the main advantages of space-based technologies (Landgrebe, 2002). Remote sensing (RS) through EO offers the possibility to obtain quantitative information at the pixel level. Having this information helps to understand environmental and socioeconomic trends. Land cover and land use maps can be used for sustainable resource management and the study of climate change phenomena. According to the Eurostat definition, land cover (LC) corresponds to the physical coverage of the land surface, while land use (LU) refers to the socioeconomic use of the land (EUROSTAT, 2022). It is possible to create thematic maps of land cover using different classification methods. Whereas photointerpretation can be ambiguous and subjective, automatic classification is a defined, quantifiable, and repeatable process (Brivio et al., 2006).

Classifying involves assigning a land cover class to all pixels in a digital image. Automatic LULC classification is typically based on the notion that different land cover types have different spectral reflectance behaviors (Townshend, 1994). Classification techniques (e.g., maximum likelihood, decision tree, and neural networks) are then used to define spectral signatures using sample data to discriminate between different classes of selected LULC based on pixel values (Pfeifer et al., 2012; Tassi and Vizzari, 2020). Image classification, which can be supervised or unsupervised, is the process of extracting semantic Information from raw data, i.e., pixel values, by assigning a class label to each pixel (Jia, 2022; Sarath, 2014). When classifying land cover, supervised approaches offer better performance than unsupervised approaches but require a sufficient number of accurate samples (Jamali, 2019).

Machine learning (ML) and deep learning (DL) are two approaches that use artificial intelligence (AI) to classify RS images. Among the classification techniques, support vector machine (SVM), random forest (RF), and maximum likelihood are ML-based algorithms. On the other hand, artificial neural networks (ANNs) can be either ML or DL depending on the layers of the network (Ma et al., 2019). All these methods are common supervised classification techniques that are also used for hyperspectral imagery (HSI) (Lv and Wang, 2020). The use of ANN for image classification and change detection has been a well-known technique for many years. Later, the focus shifted to ML algorithms, such as SVM, that could handle large data sets with few training samples, or such as RF, that were easy to use with good accuracy (Ma et al., 2019). In the last decade, however, with the rise of DL, there has been a renewed interest in ANNs for their ability to produce good results in image analysis, including land cover classification (Ma et al., 2019). These methods are derived from neural networks but have greater computational power. DL methods use deeper layers to extract feature information, particularly in the case of CNN, by considering both spatial and spectral characteristics of images (Ma et al., 2019). DL models provide promising results for object recognition or classification of hyperspectral data, by better handling images with high spatial and spectral resolution (Lv and Wang, 2020; Makantasis et al., 2015).

Multispectral data are a key resource in remote sensing because they provide more than one spectral measurement per pixel (Richards and Jia, 2006). Most multispectral satellites record information in the visible and near-infrared regions of the electromagnetic spectrum, in a number of bands ranging from three to six or more, improving the ability to distinguish man-made surfaces, vegetation, clear and turbid water, rocks, and soil (Govender et al., 2009). However, bands in multispectral sensors are not contiguous across the spectrum and often have bandwidths of 100–200 nm. As a result, unlike hyperspectral sensors, they do not have sufficient spectral resolution to directly identify materials with diagnostic characteristics (Rast and Painter, 2019). Hyperspectral data cover a wide range, from visible (0.4–0.7 nm) to shortwave infrared (SWIR) (2.4 nm) and are useful for detailed land cover legends. The ability to distinguish features with similar spectral signatures is enhanced by the availability of multiple bands (Rasti et al., 2020). In addition to improving the ability to discriminate between similar objects, hyperspectral data make it possible to perform advanced studies, for example, predicting the type and the amount of crops traits by estimating grassland biochemical parameters (Capolupo et al., 2015; Tagliabue et al., 2022).

HSI from aircraft has been in development since the 1980s, but the first hyper-spectral space EO missions for civil and scientific purposes have only been available since the early 21st century (Filchev, 2014). The main providers of space-based hyperspectral data over the last few decades have been Earth Observer-1 (NMP/EO 1) (Ungar et al., 2003), launched under NASA's New Millennium Program in 1999, with the Hyperion spectrometer, and PROBA (Project for On-Board Autonomy), launched in 2001 with the Compact High-Resolution Imaging Spectrometer (CHRIS) developed by the European Space Agency (Barnsley et al., 2004). Among the latest EO hyperspectral missions are PRISMA (Hyperspectral Precursor of the Application Mission) and EnMAP (Environmental Mapping and Analysis Program). EnMAP is a German imaging spectroscopy mission that was launched in April 2022 and recently completed its commissioning phase (Guanter et al., 2015; Storch et al., 2023). PRISMA is developed by the ASI and has been in orbit since March 2019, with commissioning completed in January 2020 (Caporusso et al., 2020). The PRISMA mission is expected to contribute to the advancement of environmental RS by providing hyperspectral data for various applications, such as monitoring of agricultural crops, forest resources, and inland and coastal waters; mapping of natural resources, soil properties, and soil degradation; climate change studies; and environmental research (Cogliati et al., 2021).

Working with HSI raises issues that are well known in the scientific community, related to the size of the data. The very high dimensionality of hyperspectral data, due to the large amount of information recorded in different bands, has some disadvantages: high storage costs, redundancy, and degraded performance (Hong et al., 2019). The dimensionality reduction is addressed using techniques based on band selection or feature extraction, as we will see below. However, the reduction in the size of the data must preserve the most relevant information it contains. To predict the separability of two classes of materials, the statistical distance between two spectral bands must be measured, and one of the most common methods is the Bhattacharyya distance (Landgrebe, 2002). The other issue is related to the notion that the number of samples that are used to train a classifier has an impact on its accuracy. Therefore, in order to maintain accuracy, the number of training pixels per class needs to increase as the dimensionality of the data increases, according to the curse of dimensionality or the Hughes phenomenon (Hughes 1968) (Alonso et al., 2011; Richards and Jia, 2006).

The literature on the use of PRISMA data, particularly in the field of land cover classification, is still limited. Most of the research shows the potential of PRISMA data for specific purposes, such as forest conservation with wildfire fuel mapping (Shaik et al., 2022) or fire detection (Amici and Piscini, 2021), geological applications (Tripathi and Garg, 2021), cryospheric applications (Kokhanovsky et al., 2022), urban surface detection (Cavalli, 2023), and mapping methane point emissions (Guanter et al., 2021). There are also interesting studies in the agricultural field dealing with specific crop or vegetation type discrimination (Pepe et al., 2020; Spiller et al., 2021; Vangi et al., 2021;

Yang et al., 2023). However, the possibility of using PRISMA data to distinguish LULC classes has not been fully investigated.

This research aims to evaluate the possibility of classifying permanent agricultural crops (i.e., orchards, fruit trees, olive groves, etc.) in a highly fragmented agricultural area using PRISMA data. The purpose of this study is to discriminate entities with very similar spectral signatures using HSI. From this point of view, high spectral resolution becomes an advantage. However, the handling of hyperspectral images may not be an easy task due to the high dimensionality of the data (Alonso et al., 2011; Hong et al., 2019). Therefore, as explained in the following sections, two techniques were tested to achieve data dimensionality reduction. For the purposes of the research, it was decided to compare three different classifiers by evaluating the accuracy of their results. In particular, among the consolidate methods for supervised classification tasks, RF, ANN, and CNN were chosen. This choice was made to test the PRISMA data using algorithms with known performance, and which are expected to produce different results (Paoletti et al., 2019). In addition, it was found useful to report the processing time for data of different dimensionality, used as input in each classifier.

2.2. Materials and Methods

The main steps of the proposed methodology are shown in Figure 2. The starting point of the procedure is the selection of the study area. Then, on the one hand, sample data are collected, both in the field and through photointerpretation, for the construction of a training data set, which is also crucial for the selection of the LC classes. On the other hand, the PRISMA satellite cube downloaded from the ASI portal was processed, including dimensionality reduction. Finally, three types of classifiers (RF, ANN, and CNN) were used for the supervised classification of the hyperspectral cube. The classification maps obtained were subjected to an accuracy evaluation phase, which allowed the selection of the best result.

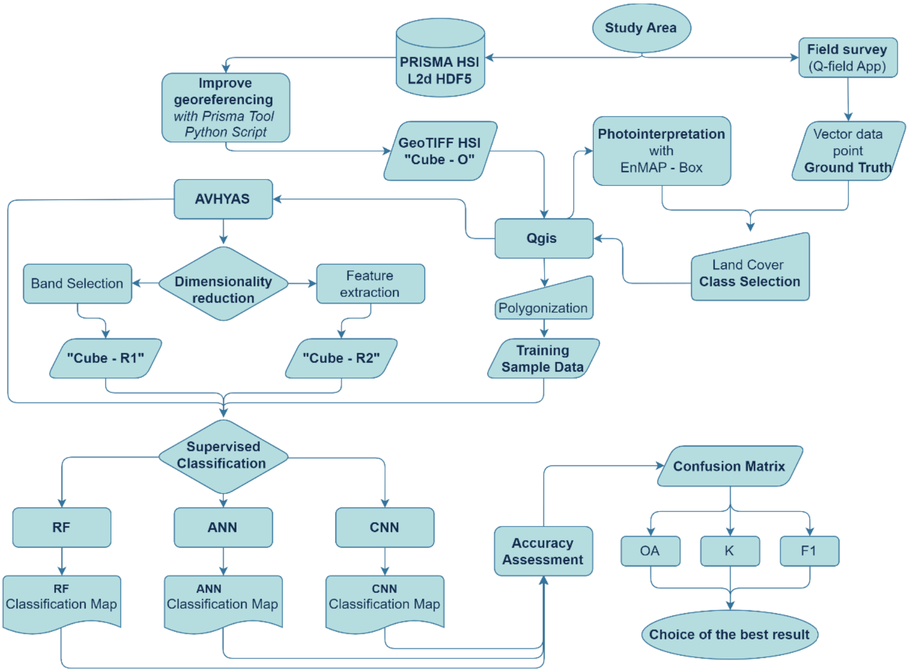

Figure 2: This flow chart shows the main stages of the proposed methodology

2.2.1. Study area

The study area is in Italy, between the provinces of Naples and Caserta, and covers an area of approximately 900 km2 north of the city of Naples, as shown in Figure 3.

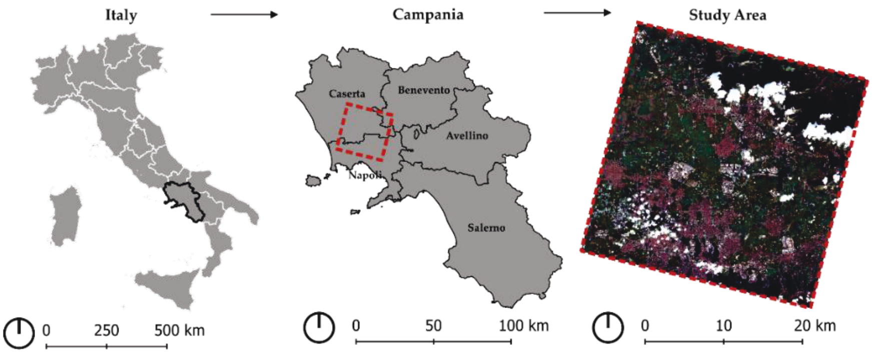

Figure 3: Framing of the Study Area

The area is largely coincident with what was once *Campania Felix* and is still known as "*Terra di lavoro*" (Giordano et al., 2003). This is a large flat agricultural area, on the left side of the *Volturno* River, partially crossed by a network of drainage canals known as *Regi Lagni*. It is an area characterized by a high degree of fragmentation. The complexity of agricultural uses in this area can be derived from the Campania Agricultural Land Use Map (CUAS) data, as shown in Table 1 (CUAS, 2009). The CUAS is an official map, accredited at the conventional scale of 1:50,000. It has been used in this research because it allows, although with unproven accuracy, the surveying of much smaller minimum mappable units than the Corine Project, which has a minimum mapping unit of 25 ha (Büttner et al., 2004). In 2009, the reference year of the CUAS, the area was mainly occupied by arable land (31%), artificial areas (28%), and orchards (18%). This study area is particularly suitable for testing the classification of complex mosaics due to its extreme fragmentation.

Table 1: CUAS surfaces classification - Source Campania Region 2009

CUAS class	Hectares	%
Urbanized Environment and Artificial Surfaces	25,373	28.30
Orchards and small fruit trees	15,931	17.77
Spring-Summer Crops - Vegetable Crops	12,594	14.05
Spring-Summer Crops - Industrial Crops	8,632	9.63
Natural pasture and upland grassland	4,401	4.91
Vernal Fall Crops - Cereals	3,703	4.13
Deciduous forests	3,354	3.74
Spring-Summer Crops - Grain Crops	2,801	3.12
Permanent pasture, meadow	2,588	2.89
Complex cropping and plots	2,512	2.80
Olive groves	2,245	2.50
Protected Crops - Horticultural and Fruit Crops	1,240	1.38
Temporary crops associated with permanent crops	1,180	1.32
Areas with sparse vegetation	655	0.73
Grasslands	649	0.72
Water	508	0.57
Fall Green Crops - Tubers	397	0.44
Shrubs and Bushes	220	0.25
Vineyards	161	0.18
Pastures unused or of uncertain use	138	0.15
Pasture	127	0.14
Poplar groves, willow groves, other deciduous trees	92	0.10
Bare rocks and outcrops	82	0.09
Citrus groves	44	0.05
Coniferous forests	16	0.02
Areas of natural colonization	11	0.01
Other permanent crops or orchards	6	0.01
Areas degraded by fire and other events	3	0.00
Artificially recolonized areas (reforestation)	2	0.00
Mixed broadleaf and coniferous forests	1	0.00
Tot.	89,666	100

Table 2 shows the data obtained from the Corine Land Cover Classification (CLC) (Büttner et al., 2004) for the year 2012. The largest percentage of the study area (30%) is occupied by anthropic areas (code_12 "111" to "142"). Agricultural areas (code_12 "211" to "112") occupy 23%, while areas with permanent tree crops (code_12 "212" to "223") occupy about 17% of the area.

Table 2: CLC surfaces classification - Source Corine project 2012.

CLC class	Code_12	Hectares	%
Non-irrigated arable land	211	20,982	23
Complex cultivation patterns	242	16,687	19
Continuous urban fabric	111	14,062	16
Fruit trees and berry plantations	222	10,641	12
Discontinuous urban fabric	112	6,351	7
Industrial or commercial units	121	3,877	4
Broad-leaved forest	311	3,215	4
Permanently irrigated land	212	3,038	3
Natural grasslands	321	2,399	3
Olive groves	223	1,987	2
Land principally occupied by agriculture […]	243	1,441	2
Annual crops associated with permanent crops	241	1,416	2
Transitional woodland-shrub	324	954	1
Sclerophyllous vegetation	323	553	1
Mineral extraction sites	131	431	0
Pastures	231	411	0
Road and rail networks and associated land	122	368	0
Airports	124	225	0
Water courses	511	195	0
Dump sites	132	157	0
Green urban areas	141	141	0
Construction sites	133	48	0
Burnt areas	334	43	0
Sport and leisure facilities	142	26	0
Coniferous forest	312	18	0
Tot.		89,666	100

Based on the study area configuration, 18 classes were selected for ground truth collection and image classification. As shown in Table 3, the level of detail was decreased or increased starting from the subdivision corresponding to Corine project level III. The level of detail was reduced for classes that were not of interest for the case study if these classes had similar characteristics. Conversely, the level of detail was increased for categories of relevance to the case study, particularly in the case of fruit trees.

Table 3: The following table shows the correspondence between the Level III classification of CLC project and the classes used in this study.

Code_12	CLC Class	Matching class	ID
111	Continuous urban fabric		
112	Discontinuous urban fabric		
121	Industrial or commercial units	Impervious	1
122	Road and rail networks and associated land		
124	Airports		
131	Mineral extraction sites	Bare Soil	2
132	Dump sites		
133	Construction sites	Impervious	1
141	Green urban areas *		
142	Sport and leisure facilities		
211	Non-irrigated arable land	Bare Soil - Crops or low vegetation**	2-3
212	Permanently irrigated land		
221	Vineyards	Vineyards	18
222	Fruit trees and berry plantations	Citrus Grove	9
		Apricot Orchard	10
		Cherry Orchard	11
		Persimmon Orchard	12
		Hazelnut Orchard	13
		Walnut Orchard	14
		Peach Orchard	15
		Poplar orchard	16
223	Olive groves	Olive Grove	17

231	Pastures	Bare Soil - Crops or low vegetation**	2-3
241	Annual crops associated with permanent crops		
242	Complex cultivation patterns		
243	Land principally occupied by agriculture […]		
311	Broad-leaved forest	Woods and Forest	4
312	Coniferous forest		
321	Natural grasslands	Bare Soil - Crops or low vegetation**	2-3
323	Sclerophyllous vegetation	Woods and Forest	4
324	Transitional woodland-shrub		
334	Burnt areas	Bare Soil	2
511	Water courses	Water	7
-	-	Clouds	5
-	-	Shadows	6

* Considering pixel spatial resolution in terms of 30 × 30 m of PRISMA image, it was preferred to assign this class to the class containing impervious surfaces. ** Depending on the case, there could be correspondence for class ID 2 or 3, as this study was not based on multitemporal analysis. Some CLC classes (i.e., Code_12: 211;212;231;241;242;243;321) may correspond to the class "ID 2: Bare soil" or alternatively to the class "ID 3: Crops or low vegetation", depending on the presence or absence of vegetation cover at the time of PRISMA image acquisition (e.g., because some areas have been tilled with agricultural machinery). The authors did not combine the two classes when classifying, but the two classes need to be aggregated to compare them with CLC classes in this table.

2.2.2. PRISMA Hyperspectral Image

According to the technical specification in Guarini et al. (2018) and Loizzo et al. (2018), the PRISMA satellite orbits at an altitude of 615 km and can deliver 223 images per day. The PRISMA spectrometer is integrated with a medium-resolution panchromatic camera and can provide images with high spectral resolution: the radiation reflected from the Earth's surface is recorded in the following spectral ranges:

VNIR (400–1010 nm) and SWIR (920–2505 nm). The hyperspectral cube consists of 240 frames with a bandwidth less than or equal to 12 nm, with a SWAT of 30 km at nadir and a GSD of about 30 m in the hyperspectral and 5 m in the panchromatic. The PRISMA products, available at http://prisma.asi.it/, are provided at different levels (Guarini et al., 2018), in particular:

- **Level 0 (L0)** refers to raw data that include ancillary data from satellite instruments;
- **Level 1 (L1)** are top-of-atmosphere (TOA) radiance images, radiometrically corrected and calibrated in physical units;
- **Level 2b (L2b)**, obtained by L1 product, spectral radiance is transformed into geophysical parameters, images are geolocated and geocoded at the bottom of the atmosphere;
- **Level 2c (L2c)** are geolocated at bottom-of-atmosphere reflectance images; Angstrom correction is applied;
- **Level 2d (L2d)** product is a geocoded version of L2c; images are orthorectified by the ASI using a DEM.

The study area is bounded by 30 × 30 square kilometers corresponding to the scene "PRS_L2D_STD_20191130100450_20191130100454_0001" acquired by the PRISMA satellite on 30 November 2019 and shown in Figure 4.

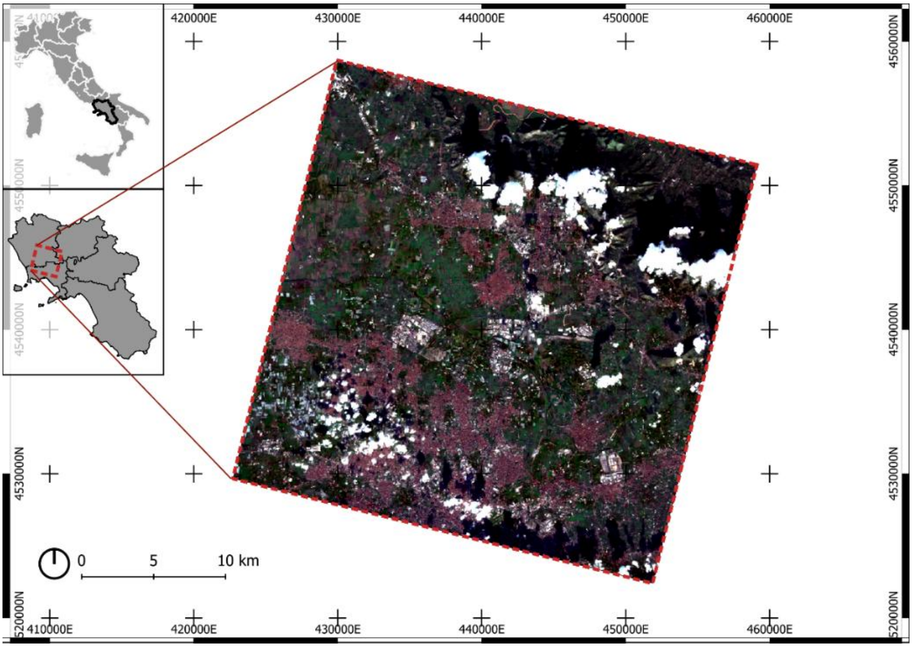

Figure 4: PRISMA scene in natural colors

For this study, it was decided to use the L2d level of the ASI data provided with reflectance values, geocoded and orthorectified. "SRTM90_CGIAR_4.1" is the digital elevation model (DEM) used by the ASI to orthorectify the L2d product of the scene. The STRM acronym stands for "Shuttle Radar Topography Mission" and refers to the joint mission of NASA and the German and Italian space agencies that started in 2000, with the goal of obtaining a high-quality global digital elevation model (Farr et al., 2007). Version 4.1 of the SRTM DEM is distributed by the Consortium for Spatial Information (CGIAR-CSI) (Boncori and Peter, 2016). It is important to note that global DEMs are generally less accurate than local DEMs and may contain errors, the main sources of which are the post-processing or generation techniques used (Capolupo, 2021). The area chosen for this study is largely flat, so negligible errors in altitude can be accepted. However, it was observed that the geocoded data were also not very accurate in spatial distribution (+/−300 m in latitude and +/−150 m in longitude). In addition, functionality to handle the HDF5 format of PRISMA data was not implemented in all mainstream software until a few years ago. For these reasons, a Python script (*Prisma Tool*) was developed (LARP, 2023a). The Prisma Tool allows data to be converted from HDF5 to the more common GeoTiff format, making the data easier to use in GIS software. At the same time, it allows for better georeferencing of images through the input of the correct vertex coordinates.

Dimensionality reduction

As mentioned above, hyperspectral data have great potential for distinguishing features with similar spectral signatures but also some disadvantages related to data dimensionality. Dimensionality reduction techniques can generally be divided into two types: those based on feature extraction and those based on band selection. Those based on feature extraction, such as principal component analysis (PCA), which selects a subset of features with high variance from the original data, involve a loss of information. This is why feature selection is the preferred dimensionality reduction technique in HSI, where a subset of bands is selected without loss of their physical meaning (Zhang et al., 2018). Several techniques have been proposed in the literature to solve the band selection challenge (Sawant and Prabukumar, 2020).

In this case study, starting with the original 240-band cube (Cube-O, where “O” stands for original), two different methods were used.

- The first is based on an approach like supervised band selection techniques that allow us to choose which bands to keep. This step was aimed at eliminating bands corresponding to atmospheric windows with low or zero radiance values, rather than greatly reducing the size of the data. Random spectral signatures associated with different types of surfaces were compared as shown in Figure 5. In accordance with previous approaches (Flynn et al., 2020; Zhang et al., 2018), the bands with the lowest signal-to-noise ratio and atmospheric water vapor absorption were selected for removal. Through this process, a new hyperspectral cube of 156 bands (Cube-R1, where “R1” indicates the first reduction) was derived from the original 240 bands. The bands removed were those related to the ranges 1290–1490 nm, 1700–2050 nm, and 2350–2495 nm.

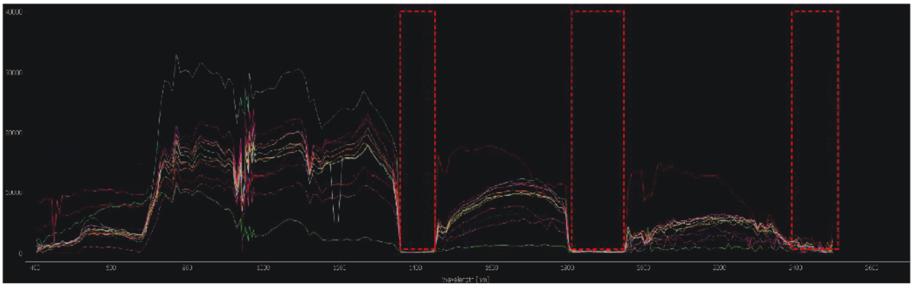

Figure 5: Random spectral signature of the original PRISMA Cube-O; the red rectangles correspond to the area in which the bands with the lowest values have been removed. Authors’ elaboration using Qgis with the EnMAP-Box plugin described in the following section

- The second method is based on the application of the statistical method of PCA (Jolliffe, 1986), which is widely used in the scientific community (Sawant and Prabukumar, 2020) to reduce the cube dimension, removing bands that are strongly correlated to others. The original hyperspectral cube was used as input data. At the end of the processing, 20 principal components were selected, preserving a percentage of variance in the data of 98.7% (Cube-R2, where “R2” indicates the second reduction). The AVHYAS plugin described in the following section was used for PCA.

It is worth noting that the Cube-R2 obtained through the PCA has kept a high percentage of the variance that was computed on Cube-O. PCA, which is very useful to distinguish between classes that are very different from each other, could mask the information recorded in the original data about small differences between similar classes. For the classification task, the authors decided to alternatively test the two images (Cube-R1 and Cube-R2) obtained using the models described above to evaluate this issue.

2.2.3. Software used

Qgis has been used as an open-source GIS software for the purpose of this study. This software is an official project of the Open-Source Geospatial Foundation (OSGeo) (OSgeo, 2023) and is one of the most widely used open-source GIS software worldwide due to its ability to easily implement a variety of functions through plugins. Qgis offers several plugins for supervised classification of satellite images.

However, the ability to classify hyperspectral data, especially using DL-based approaches such as neural networks, is still limited. A solution is offered by the Advanced Hyperspectral Data Analysis (AVHYAS) plugin (Lyngdoh et al., 2021). The AVHYAS plugin has been developed by the Space Applications Centre (SAC) of the Indian Space Research Organization. It is a HSI processing and analysis plugin based on Python-3. The plugin extends the existing Qgis GDAL functionality. It uses several modules such as Tensor-Flow for DL and Scikit-Learn for machine learning. The purpose of the plugin is to exploit the visualization capabilities of Qgis by integrating them with the most advanced techniques available in the literature for hyperspectral data management and classification. The ability to experiment with different supervised classification techniques based on ML and DL within the same application was another reason for choosing AVHYAS.

Another very useful plugin was EnMAP-Box, developed by the Humboldt University of Berlin and the University of Greifswald, to handle data from the German hyperspectral satellite EnMAP (Van Der Linden et al., 2015). This plugin constituted the starting point for the development of the AVHYAS plugin mentioned above. It combines the visualization capabilities of Qgis with the ability to manage and process hyperspectral data, as in the previous case. Some of its main features are listed below. The plugin further provides (i) the ability to easily visualize HSI, both as a two-dimensional image and as a hyperspectral cube; (ii) the exploration of high-dimensional data and hyperspectral libraries; and (iii) the collection of spectral signatures in spectral libraries. It also allows data to be processed using some of the most popular algorithms in the scientific community (i.e., support vector machines or RF-based raster classification, regression, and clustering approaches from the scikit-learn library).

For field sample data collection, the QField mobile application (QField App, 2023) has been used; it is based on Qgis and was developed specifically for field work. The main goal is to help users perform the tasks required in the field, such as data collection and storage.

2.2.4. Sample data

In order to apply supervised classification techniques, it was necessary to collect a dataset of labeled data, to be used both for training the classifiers and testing the results. In addition, as mentioned above, the number of training samples affects the accuracy of a classifier. Using a large number of bands requires a large number of observations to maintain classification accuracy (Alonso et al., 2011). Since it was chosen to maintain a large number of bands as the input data, a consistent number of ground truths was collected. Specifically, three sets of labeled data were used. Each set was collected at different times and in different ways.

(A) The first set was collected on 23 October 2019. The coordinates of the collected points, corresponding to the centroids of the agricultural plots, were obtained using differential GPS and then entered into a CSV file. The CSV file, which also included attributes related to the type of LC, was then imported into GIS software. Using the coordinates in the attribute table, the points were automatically georeferenced. Thus, a vector datum of the points was obtained, which in turn made it possible to derive polygon vector data, considering the perimeter of the cultivated areas. Photointerpretation and geotagged images collected during the survey made this step possible. During the first survey, 160 control points were surveyed and classified simultaneously as the satellite image was acquired. Of these, 106 involved agricultural parcels, which in turn were divided into 43 points for permanent crops and 63 for temporary crops. Figure 6 shows the preservation of the canopy for almost all the permanent crops and trees classified in this study at the time of the first survey. This study is not based on a multitemporal analysis of the study area. The classification was made on the basis of a November image. During this period, the canopy of the trees may have had a low number of leaves. However, the leaves of the plants selected for this study were not yet in the phase of leaf abscission, as can be seen in the photos below.

Figure 6: Photos representative of some of the classes of interest (ID from 9 to 18) in this study collected during the field survey on 23 October 2019.

(B) Later, research was suspended due to the COVID-19 pandemic. However, it was necessary to increase the number of labeled data to have more confidence in the statistical validation of the results. It was assumed that ground truths could still be integrated for the arboriculture sector after three years of image acquisition. In the survey, great care was taken in the estimation of the probable date of planting from the tree characteristics. In this way, only plantings that were older than the date of the satellite image was included in the survey. The second survey took place in April 2023 and allowed the detection of 150 additional ground truths. This brings the total number of GCPs related to permanent cultures to 180. In this case, the QField app was used during the survey to collect point vector data directly in the field, using the AGPS of a smartphone. In an attempt to open up to the world of citizen science and crowdsensing data collection, this type of approach was preferred over the traditional one. The accuracy of AGPS provided by common smartphones was considered adequate for this study, given the 30 m spatial resolution of the PRISMA image. Using the QField app, the collected points could be entered directly into the GIS environment in their correct location (QField App, 2023). This is possible through the activation of a satellite base map and smartphone localization in the app during the survey. The georeferenced vector point datum was then used to derive a polygon datum using the same methodology as the first labeled dataset (A).

(C) Photointerpretation also allowed for the addition of new classes such as clouds, shadows, and water. It also increased the area for some of the classes already present, such as impervious surfaces, bare soil, and temporary agricultural surfaces. Photointerpretation was performed using the results of different false-color compositions of the PRISMA image. A total of six different false-color band compositions were used. The main objective was to improve the ability to distinguish between bare soil and temporary or permanent vegetation by photointerpretation. The selection of the bands is based on the combination method of the raster layer styling panel of the Qgis EnMAP-Box plugin (Van Der Linden et al., 2015). Table 4 shows the RGB bands used for each composition, and Figure 7 shows the resulting maps.

Table 4: This table shows the bands used in false color composition to obtain the maps 1 to 6, shown in Figure 7.

		Red channel		Green channel		Blue channel	
	MAP	band	nm	band	nm	band	nm
Natural color	1	34	0669.5	22	0562.5	13	0492.5
False color	2	34	0669.5	50	0833.4	22	0562.5
Color Infrared	3	50	0833.4	34	0669.5	22	0562.5
Agriculture	4	128	1616.5	50	0833.4	13	0492.5
Healthy vegetation	5	50	0833.4	128	1616.5	13	0492.5
Recent Harvest	6	193	2198.8	50	0833.4	22	0562.5

Figure 7: Maps resulting from False Color Combination: 1 - Natural color; 2 - False color; 3 - Color Infrared; 4 – Agriculture; 5 - Healthy vegetation; 6 - Recent Harvest.

Table 5 shows the dimensions in hectares of the surfaces in the sample dataset by class and group.

Table 5: Ha surfaces of labeled data distinguished by class and group: A: ground truths surveyed in 2019; B: ground truths surveyed in 2023; C: labeled data obtained by photointerpretation.

ID	Class	A	B	C	Tot.
1	Impervious	8.23	0.00	203.85	212.08
2	Bare soil	26.35	8.75	86.81	121.90
3	Temporary crops	19.83	1.29	47.29	68.41
4	Woods and forest	6.49	0.82	42.60	49.91
5	Clouds	0.00	0.00	176.35	176.35
6	Shadows	0.00	0.00	217.53	217.53
7	Waters	0.52	0.00	17.90	18.42
8	Greenhouses	1.97	0.00	27.65	29.62
9	Citrus groves	0.00	2.88	0.00	2.88
10	Apricot orchard	0.73	9.28	0.00	10.00
11	Cherry orchard	0.00	4.34	0.00	4.34
12	Persimmon orchard	4.53	8.82	0.00	13.35
13	Hazelnut orchard	0.00	18.14	0.00	18.14
14	Walnut orchard	5.99	12.61	0.00	18.60
15	Peach orchard	4.87	1.44	0.00	6.32
16	Poplar orchard	2.16	2.73	0.00	4.89
17	Olive groves	11.29	5.40	0.00	16.70
18	Vineyard	1.11	3.68	0.00	4.79
Tot.		94.07	80.18	819.98	994.23

2.2.5. Supervised classification techniques

The primary purpose of this study is to evaluate the possibility of using PRISMA data to classify land cover classes, in particular different types of orchards, as mentioned in the introduction. For this purpose, three of the most common classification techniques (Lv and Wang, 2020; Paoletti et al., 2019) were investigated: RF, ANN, and CNN. Classification tests were performed in Qgis 3.14.1 software using the AVHYAS plugin (Lyngdoh et al., 2021). The different techniques were tested by classifying the same study area. The images used as input were both the one corresponding to the Cube-R1 with 156 bands and the one corresponding to the Cube-R2 obtained by the PCA. The same number of labeled data was used in each test run. In the case of neural networks, the training data set was randomly divided into training (70%) and test (30%) sites by AVHYAS prior to each test run. For random forests, k-fold cross-validation with 3 iterations was used for validation. The AVHYAS plugin provides some of the most common networks in the literature (Paoletti et al., 2019) through a dedicated DL classification module. Reflecting the evolution of the literature, 13 different neural network architectures are available within this module. The default setting was used in the selection of some parameters for the proposed study since the aim was not to define the optimal scenario in the use of this tool. In addition to different input data, the number of trees for the RF algorithm and the number of epochs for the neural networks differed between tests.

Random Forest

The RF algorithm developed by Breiman in 2001 is an ML-based approach (Breiman, 2001). Classification is based on individual decision trees working as an ensemble. A random subset of labeled samples is used to train each tree. The randomization of the training data reduces the probability of error as the number of trees increases. Each tree expresses only one vote per instance, and the final classification is given by the majority of votes from all trees (Breiman, 2001; Lim et al., 2019). The choice of the number of trees affects the classification result. Considering similar works, a suitable number to balance accuracy and time spent is around 500 (Naidoo et al., 2012; Sothe et al., 2020). However, in this study, six different tests with 100, 500, and 1000 trees were performed, alternately using both Cube-R1 and Cube-R2 as input, to test the performance of the used data.

Artificial Neural Network

Some tests were carried out with a classification approach based on the ANN, using the model of the basic network proposed by the plugin. In this case, the "Baseline (Fully Connected NN)" model was chosen. This is a sequential model of a fully connected network with 3 hidden layers, where each neuron is fully connected to all those in the previous layer. The learning rate has been left at the default value of 0.0001. This value, considered small, is slower in that it requires more epochs for training, but it is generally more suitable for dealing with complex problems (Wilson and Martinez, 2001). A total of 6 trials were run. The number of epochs chosen from time to time was 10, 50, and 100, where Cube-R1 was used as input in 3 cases, and Cube-R2 was used in the remaining 3 cases. Some tests were performed using an ANN-based classification approach using the DL module available in AVHYAS (Lyngdoh et al., 2021).

Convolutional Neural Network

The utility of using CNNs for HSI classification has been widely described in the literature (Pandian et al., 2022; Paoletti et al., 2019; Sothe et al., 2020). Thanks to specific convolutional kernels, CNN can use both spatial and spectral information to classify images. In the present work, among the models available in the AVHYAS plugin, the "Hu (1D CNN)" was used. This model is based on the one proposed by Hu et al. (2015). The architecture of the network is similar to the one shown in Figure 8. It is a one-dimensional network and considers only spectral signatures by using a convolutional layer and a fully connected layer. The default value for the learning rate, which was kept in this case, is 0.01. Six trials were run with the number of epochs 10, 50, and 100. Cube-R1 and Cube-R2 were used alternately as input data.

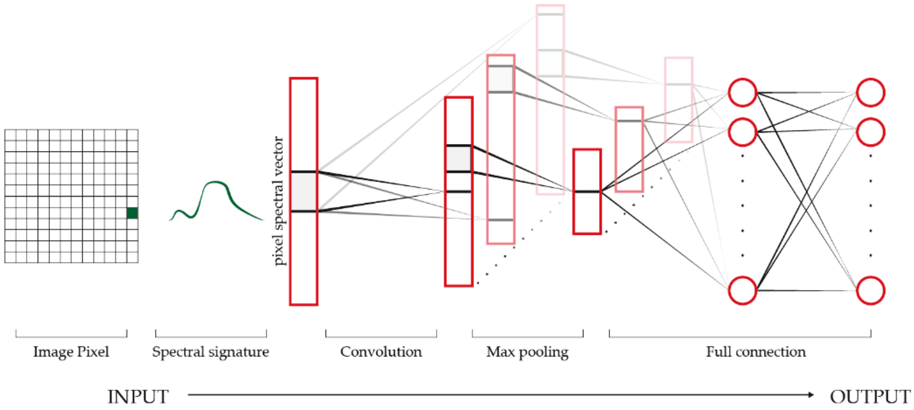

Figure 8: This figure shows a CNN architecture similar to the one proposed by Hu (2015) - authors' elaboration based on Hu et al. (2015).

2.2.6. Accuracy assessment

In case studies involving the use of remotely sensed data to produce land cover maps, assessment of the accuracy of the resolutions is essential. For quantitative assessment of the accuracy of the results, an error matrix can be generated, which can be used for a number of descriptive and analytical statistical analyses. The most common terms are overall accuracy (OA), kappa coefficient (K) (Cohen 1960), user's accuracy (UA), and producer's accuracy (PA) (Congalton, 2001). OA is the percentage of correctly classified pixels and is given by the ratio of the number of correctly classified pixels to the total number of test pixels used. Cohen's K is a measure of the agreement between the predicted values and the actual values. This metric measures how much better the classification that was made is in comparison to a classification made by chance. UA estimates the commission error and indicates the probability that a pixel predicted to be in a certain class actually belongs to that class. PA estimates the omission error and indicates the probability that a pixel belonging to a given class has been correctly classified. Another statistical indicator used is the F1 score, which is the harmonic mean between precision and recall for each class, varying from 0 (worst case) to 1 (best case) (Grandini et al., 2020).

The error matrix automatically generated by the AVHYAS plugin in the final report was used to evaluate the results in this case study. The classification results were evaluated globally in terms of OA and K. Results for individual classes were evaluated in terms of UA, PA, and F1 score. In the case of random forest, cross-validation was used, so the validation was carried out on the total number of labeled pixels. In the case of neural networks, 30% of the randomly selected pixels for the test phase were used to validate the results.

2.3. Results

This section presents the results of the classification techniques used. For each one of the three methods of classification used (RF, ANN, and CNN), the results are very different in terms of OA, K, and F1 score indices and also for PA, UA, and F1 evaluated for each class. Table 6 shows a comparison of the best results of the methods used for classification in terms of global accuracy (OA, K, and F1) for all the classes and running time (h).

Table 6: RF, ANN, and CNN comparison.

	Input Data	OA	K	F1	h
RF	Cube-R2 (20 PCA)	0.89	0.87	0.60	0.1
ANN	Cube-R1 (156 bands)	0.96	0.96	0.77	67.2
CNN	Cube-R1 (156 bands)	0.97	0.97	0.84	2.4

Figure 9 shows a comparison graph between the RF, ANN, and CNN performances in terms of the F1 score obtained for the classes of permanent agricultural cover that are mainly considered in this study (ID from 9 to 18).

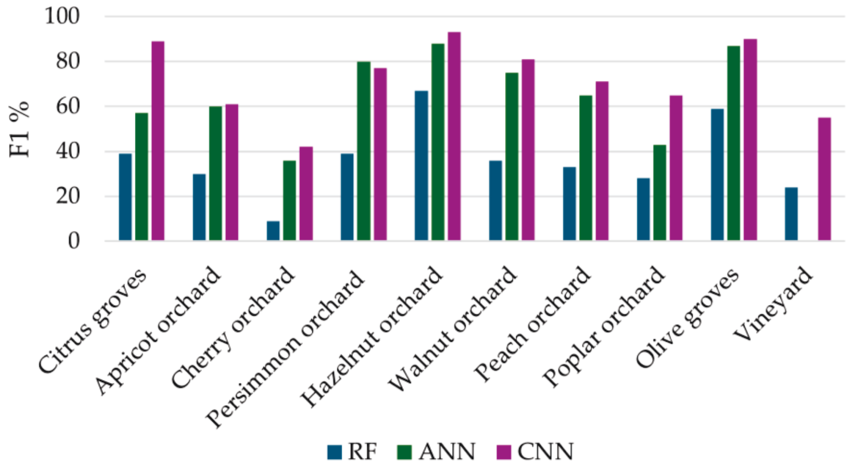

Figure 9: RF, ANN, and CNN comparison in terms of F1 score for classes of interest (ID from 9 to 18).

The following pages report the values of the best results obtained in the different tests using RF, ANN, and CNN. In the first table of each subsection, in addition to OA and K, the data used as input and the processing time are also reported. The second table in each paragraph shows the results for each of the classes considered and the area in *Ha* obtained.

Table 7 shows the overall values for the best result of the RF algorithm obtained with the PCA-derived Cube-R2. Figure 10 shows the resulting classification map, while a detail is shown in Figure 11.

Table 9 shows the overall values for the best result obtained with ANN, using Cube-R1 with 156 bands as input. OA and K index values are very high but not homogeneous, because they are influenced by the results obtained in the cases of the first eight classes. Figure 12 shows the resulting classification map, while a detail is shown in Figure 13.

Table 11 shows the global values for the best result obtained with CNN, using Cube R1 with 156 bands. Figure 14 shows the resulting classification map, while a detail is shown in Figure 15.

Table 7: RF classification results, overall evaluation.

Input	n. Trees	OA	K	F1	Hours
Cube-R2	500	0.887	0.867	0.603	0.052

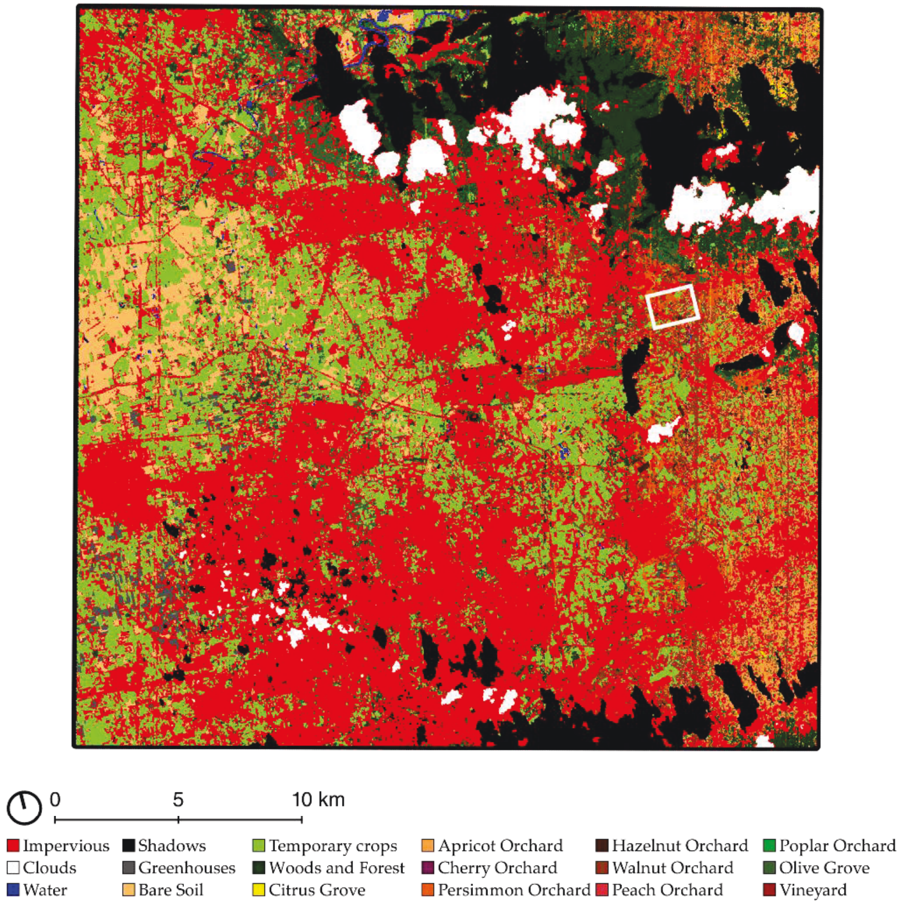

Figure 10: Random forest classification results. White rectangle corresponds to detail shown next

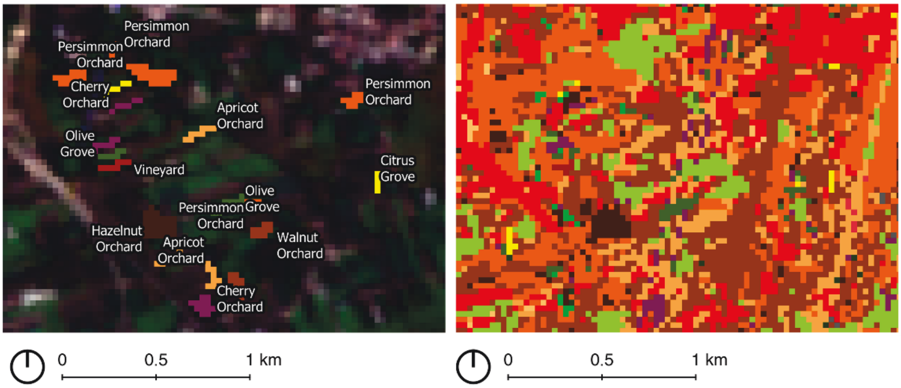

(a) (b)

Figure 11: This figure suggests a detail from Figure 10 that corresponds to the white rectangle. The visual comparison is between (a) pixels used as labeling data to train the classifier and test the results and (b) detail of RF classification results

Table 8 shows the values by class for the best result obtained with the RF algorithm.

Table 8: RF classification results, per class evaluation

ID	Class	UA [%]	PA [%]	F1 [%]	Ha
1	Impervious	93	88	91	37,203
2	Bare soil	92	96	94	4922
3	Temporary crops	83	80	81	16,671
4	Woods and forest	84	81	83	5444
5	Clouds	100	100	100	2698
6	Shadows	99	99	99	53,888
7	Waters	72	99	84	225
8	Greenhouses	91	88	90	1002
9	Citrus groves	27	69	39	103
10	Apricot orchard	31	28	30	2690
11	Cherry orchard	6	16	9	123
12	Persimmon orchard	40	38	39	2402
13	Hazelnut orchard	72	62	67	377
14	Walnut orchard	40	33	36	3539
15	Peach orchard	29	38	33	342
16	Poplar orchard	18	71	28	213
17	Olive groves	59	60	59	2566
18	Vineyard	14	78	24	78

Table 9: ANN classification results, overall evaluation.

Input	n. Epochs	OA	K	F1	Hours
Cube-R1	100	0.963	0.956	0.766	67.166

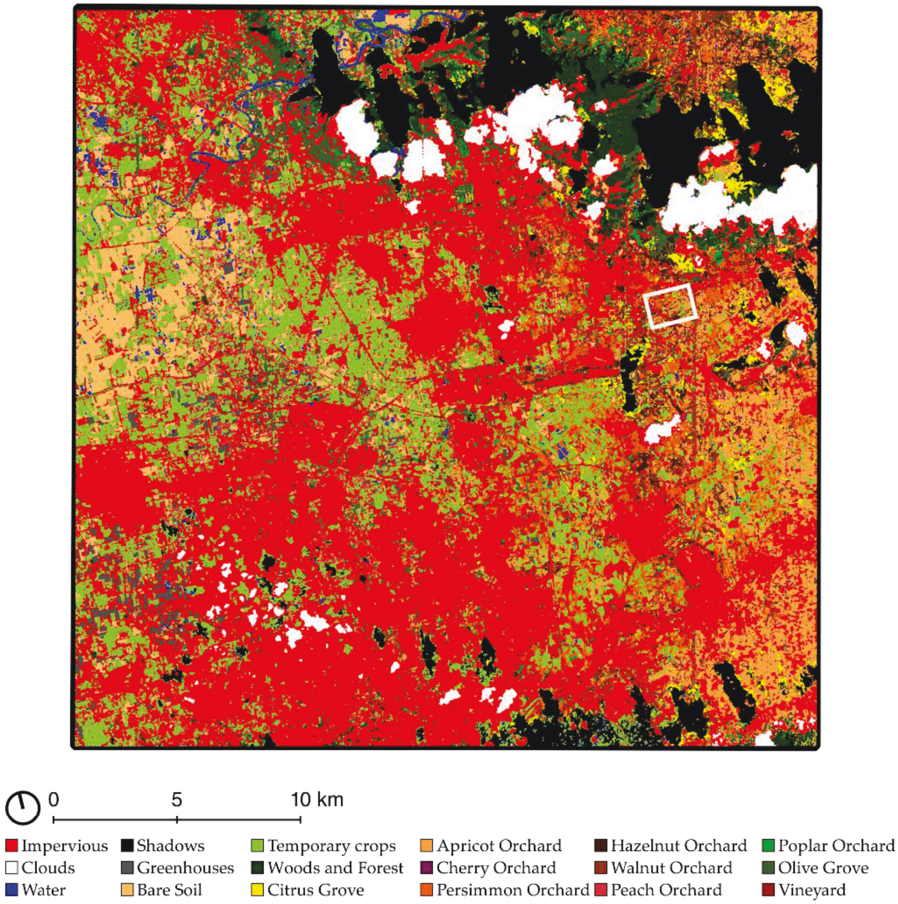

Figure 12: Artificial neural network classification results. White rectangle corresponds to detail shown next

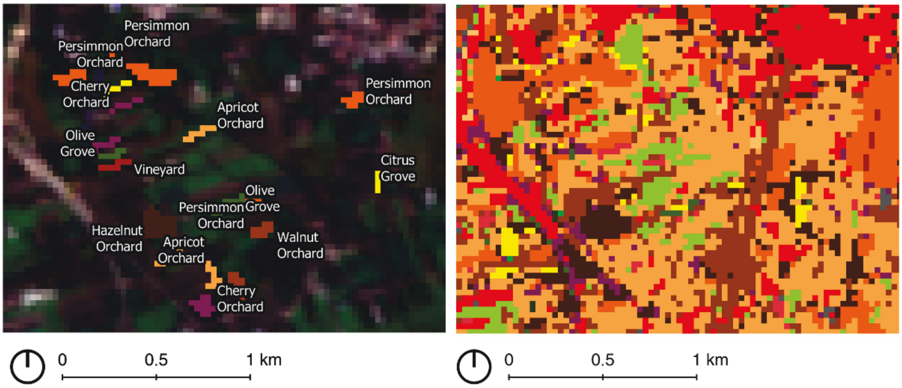

(a) (b)

Figure 13: This figure suggests a detail from Figure 12 that corresponds to the white rectangle. The visual comparison is between (a) pixels used as labelling data to train the classifier and test the results and (b) detail of ANN classification results

Table 10 shows the values by class for the best ANN scores.

Table 10: ANN classification results, per class evaluation

ID	Class	UA [%]	PA [%]	F1 [%]	Ha
1	Impervious	100	98	99	34,668
2	Bare soil	99	100	99	4628
3	Temporary crops	94	96	95	13,118
4	Woods and forest	97	99	98	2500
5	Clouds	100	100	100	3247
6	Shadows	99	100	100	51,221
7	Waters	98	100	99	664
8	Greenhouses	96	100	98	1275
9	Citrus groves	60	55	57	1224
10	Apricot orchard	91	45	60	6589
11	Cherry orchard	29	50	36	297
12	Persimmon orchard	77	83	80	3375
13	Hazelnut orchard	98	79	88	1703
14	Walnut orchard	71	79	75	3296
15	Peach orchard	64	67	65	2209
16	Poplar orchard	35	55	43	862
17	Olive groves	87	87	87	2852
18	Vineyard	0	0	0	540

Table 11: CNN classification results, overall evaluation

Input	n. Epochs	OA	K	F1	Hours
Cube-R1	100	0.973	0.968	0.842	2.399

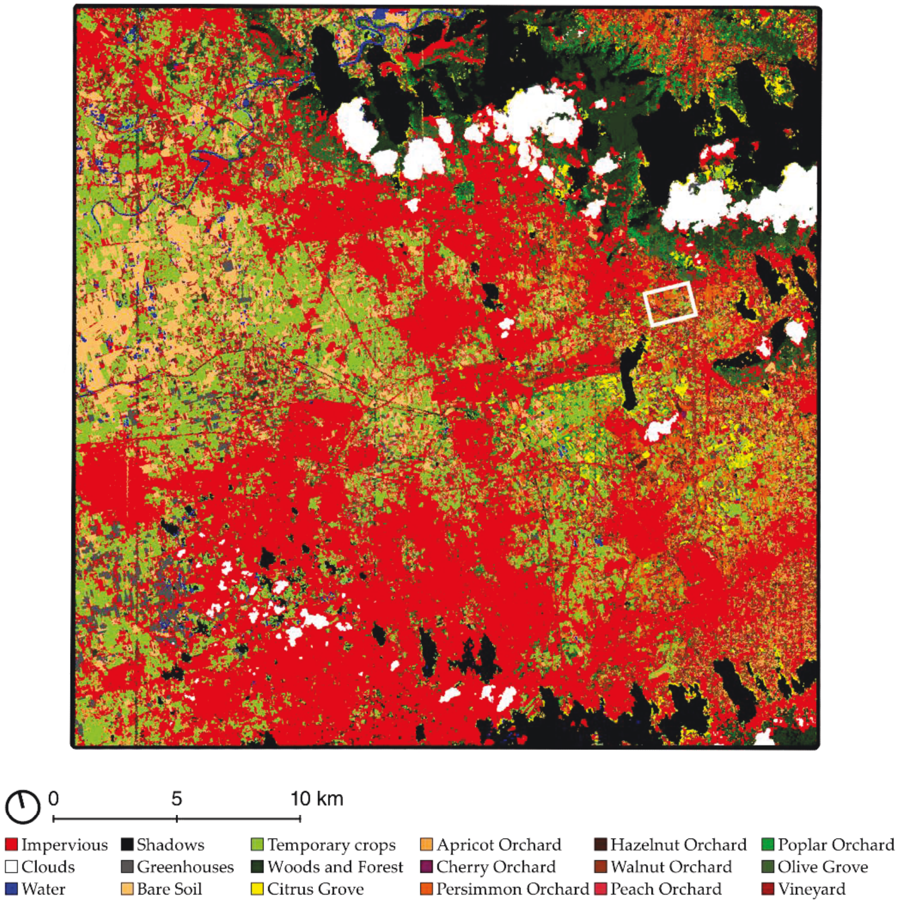

Figure 14: Convolutional neural network classification map. White rectangle corresponds to detail shown next

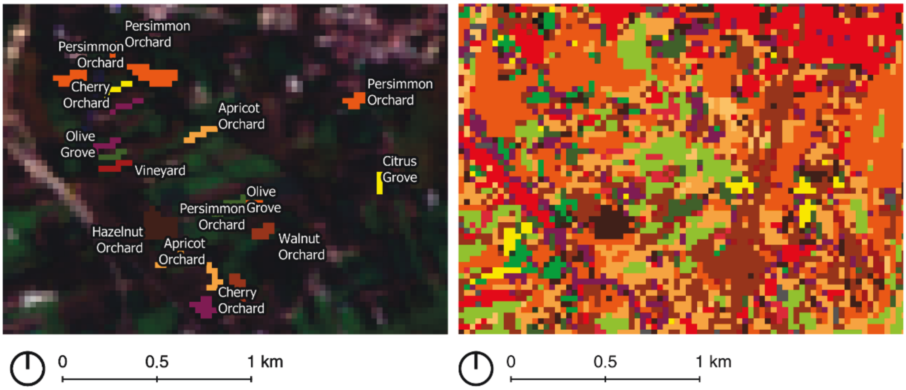

(a) (b)

Figure 15: This figure suggests a detail from Figure 14 that corresponds to the white rectangle. The visual comparison is between (a) pixels used as labeling data to train the classifier and test the results and (b) detail of CNN classification results.

Table 12 shows the values by class for the best result with CNN.

Table 12: CNN classification results, per class evaluation.

ID	Class	UA [%]	PA [%]	F1 [%]	Ha
1	Impervious	99	100	99	30,850
2	Bare soil	99	100	100	5429
3	Temporary crops	99	95	97	13,956
4	Woods and forest	98	96	97	4290
5	Clouds	100	100	100	3050
6	Shadows	100	100	100	53,105
7	Waters	100	100	100	570
8	Greenhouses	99	98	98	1733
9	Citrus groves	80	100	89	1217
10	Apricot orchard	53	71	61	3533
11	Cherry orchard	36	50	42	622
12	Persimmon orchard	77	77	77	2571
13	Hazelnut orchard	93	93	93	718
14	Walnut orchard	84	79	81	3778
15	Peach orchard	68	75	71	1778
16	Poplar orchard	76	57	65	1643
17	Olive groves	96	85	90	3396
18	Vineyard	40	86	55	2027

2.4. Discussion

Land cover classifications based on multispectral data allowed us to distinguish more general land cover classes. The use of hyperspectral data has advanced the identification of detailed maps of LULC. However, as noted in the introduction, most of the research focuses on temporary crops (Pandian et al., 2022; Spiller et al., 2021; Zhang et al., 2010) or a few tree species (Bandyopadhyay et al., 2023; Lim et al., 2019). The results show that a detailed legend for land cover maps can be obtained by supervised classification using HSI. In particular, it is possible to extend the classification to the fourth level, starting from the third level of CLC. This study shows how the PRISMA data can be used to distinguish between many types of permanent crops. In this case study, CLC class "222 - Fruit and berry plantations" was divided into eight subclasses. The results show that in the case of CNN, using Cube-R1, the F1 score is higher than 0.7 for the following classes: hazelnut orchard: 0.93; olive groves: 0.90; citrus groves: 0.88; walnut orchard: 0.81; persimmon orchard: 0.77; peach orchard: 0.71. Based on these results, it can be said that the main objective of this study has been demonstrated. Supervised classification using HSI provides an opportunity to obtain a detailed legend for land cover maps. Furthermore, to understand the actual applicability of the data in the application domain, the worst-case scenario was assumed (non-multitemporal analysis with a single autumn image), but even in this case, the results were very interesting. It is also true, as the photos in Figure 6 show, that the climatic conditions of the study area were conducive to the maintenance of the canopy over a longer period of time.

Among the different techniques used for the classification, the best choice seems to be the use of CNN. In terms of OA, K, PA, UA, and F1, this technique gave the best global result and per-class evaluation.

However, the classification with the RF algorithm gave interesting global results (OA: 0.887; K: 0.867; F1: 0.603), using Cube-R2, but not comparable to those of the neural networks. It is an excellent alternative for land cover mapping with aggregated classes due to its very fast computation times. Indeed, excellent results were obtained with F1 scores above 80% for impervious, bare soil, temporary crops/low vegetation, and woods and forests. With respect to the classes of interest (ID from 9 to 18), the best results concern the classes hazelnut orchard (67%) and olive grove (59%).

Classification with ANN produced excellent overall results (OA: 0.963; K: 0.956; F1: 0.766) using Cube-R1. The F1 score, which is higher than in the RF case, for some of the classes of interest (ID from 9 to 18), such as cherry and poplar groves, is less than 60% and 0% in the case of vineyards. It may be possible to obtain better results for these classes with an image from a different season. But in the case of olive, hazelnut, and persimmon groves, results higher than 80% in terms of F1 seem to be very favorable. Among the disadvantages, it is necessary to highlight the onerous cost of calculation in terms of hours spent.

In the case of convolutional neural networks, using Cube-R1 as in the previous case, the OA and global K coefficients are very high (OA: 0.973; K: 0.968; F1: 0.842). This is because they are influenced by the very high level of accuracy in the case of aggregated classes such as impervious. However, in this case also, UA, PA, and F1 values are higher compared to the previous techniques. The convolutional network seems to guarantee better classification results, especially for the following classes: hazelnut, olive, persimmon, and walnut. On the contrary, for cherry, vineyard, and apricot, the classification is less accurate. For the classes of interest (ID from 9 to 18), the classification output shows percentages higher than 70% in terms of the F1 score in 6 out of 10 cases (hazelnut orchard: 0.93; olive grove: 0.90; citrus grove: 0.88; walnut orchard: 0.81; persimmon orchard: 0.77; peach orchard: 0.71).

Convolutional technology produces an overall F1 score that is almost 10% better than ANN and 25% better than RF. When evaluating the results obtained in the classes of interest (ID from 9 to 18), CNN guarantees almost 30% better F1 results compared to RF in all classes. Compared to ANN, there are improvements of more than 20% in the vineyard, citrus, and poplar classes; they are equivalent for the apricot and persimmon classes; while for all the others, there are slightly better results with CNN.

Based on the results obtained, it has been proven that the convolutional network guarantees excellent results with PRISMA hyperspectral data, especially with the cube resulting from the band selection (Cube-R1) and with a number of epochs equal to 100.

2.5. Conclusion

This study shows that the HSI data, by achieving very high classification results in terms of F1 scores for some classes, can discriminate between different types of permanent crops (ID from 9 to 18). As shown before, the results in terms of F1 score are higher than 0.70 in 6 out of 10 cases (hazelnut orchard—0.93; olive grove—0.90; citrus grove—0.88; walnut orchard—0.81; persimmon orchard—0.77; peach orchard—0.71). This shows that satellite imagery can be used for level IV classification and confirms studies based on PRISMA data to distinguish crops (Spiller et al., 2021), vegetation (Pepe et al., 2020), or forest types (Vangi et al., 2021).

The most promising technology for this kind of application is based on neural network methods, especially CNNs (CNN F1 results are almost 30% better compared to RF for permanent crops). Indeed, various studies have demonstrated the potential of CNNs for hyperspectral data classification compared to other techniques (Hu et al., 2015; Pandian et al., 2022; Paoletti et al., 2019; Sothe et al., 2020). The best results were obtained with CNN using Cube-R1 (156 bands). This confirms that strong dimensionality reduction is not necessary when using DL-based methods (Yang et al., 2023).

When dealing with high dimensionality of data, methods based on ML have limitations (Friedman, 1997). This aspect necessitates information reduction, which inevitably has an impact on the ability to discriminate classes with similar characteristics. However, as shown in Naidoo et al. (2012), better results can be obtained with focused band selection.

The processing times may not be relevant for a case like this, where only a single data set is processed. However, this aspect could become crucial for multitemporal analyses or when experiments are carried out with different sample data. Although the best results were obtained with CNN, this method is more time consuming than RF. In fact, the main disadvantages of this method are the computational time and computer power consumption (Huang et al., 2002; Sothe et al., 2020). However, it is important to note that the algorithms have been used on open-source tools, so most of the processing/analysis is single-threaded. The time required could be significantly reduced as open-source software evolves to a multithreaded perspective.

In terms of reducing the high dimensionality of the data, the best results were obtained using Cube-R1 derived by band selection. Eliminating bands in the three regions of the spectrum where the transmittance is low is always useful (Flynn et al., 2020; Sawant and Prabukumar, 2020; Zhang et al., 2018). Data obtained with this method preserve more than 150 bands of the original 240. It guarantees good results when used as input for neural networks, but not for RF. Feature extraction using the PCA method is essential in this case. Starting from the original Cube-O, PCA can significantly reduce data dimensions while preserving a high percentage of variance. Therefore, it is useful for discriminating between very different classes, but as stated in the previous paragraphs, it tends to overlook the few differences between similar classes.

As mentioned in the introduction, there is to date a lack of studies using PRISMA for LULC classification. The reasons are mainly due to the difficulties in accessing and managing the data. However, future improvements are expected in both data availability, partly due to new hyperspectral missions such as EnMAP (Storch et al., 2023), and data quality, using higher-accuracy DEMs for orthorectification. This would improve the reflectance accuracy, and thus even more accurate classifications are likely. It is expected that the interest in HSI will increase soon, especially because of the possibilities and advantages in the field of natural and agricultural land classification and monitoring.

The analysis of multi-seasonal imagery will certainly be a possible future application of PRISMA hyperspectral data for land cover mapping. The most promising way seems to be the use of convolutional networks. Future tests will certainly favor CNN by including different models for the network architecture. A chance to improve the results could certainly be achieved by making use of 3D CNNs that take advantage of the combination of spatial and spectral information (Arun and Akila, 2023). Also, a different dimensionality reduction method with more specific band selection may be used. This would allow for better results with ML algorithms that are less time-consuming, such as RF, or less sensitive to the Hughes phenomenon, such as SVM (Melgani and Bruzzone, 2004).

Chapter 3

Testing the Impact of Pansharpening Using PRISMA Hyperspectral Data: A Case Study Classifying Urban Trees in Naples, Italy

Miriam Perretta, **Gabriele Delogu**, Cassandra Funsten, Alessio Patriarca,
Eros Caputi, and Lorenzo Boccia

Published in Remote Sens. **2024**, 16, 3730.
https://doi.org/10.3390/rs16193730

Abstract

Urban trees support vital ecological functions and help with the mitigation of and adaption to climate change. Yet, their monitoring and management require significant public resources. remote sensing could facilitate these tasks. Recent hyperspectral satellite programs such as PRISMA have enabled more advanced remote sensing applications, such as species classification. However, PRISMA data's spatial resolution (30 m) could limit its utility in urban areas. Improving hyperspectral data resolution with pansharpening using the PRISMA coregistered panchromatic band (spatial resolution of 5 m) could solve this problem. This study addresses the need to improve hyperspectral data resolution and tests the pansharpening method by classifying exemplative urban tree species in Naples (Italy) using a convolutional neural network and a ground truths dataset, with the aim of comparing results from the original 30 m data to data refined to a 5 m resolution. An evaluation of accuracy metrics shows that pansharpening improves classification quality in dense urban areas with complex topography. In fact, pansharpened data led to significantly higher accuracy for all the examined species. Specifically, the Pinus pinea and Tilia x europaea classes showed an increase of 10% to 20% in their F1 scores. Pansharpening is seen as a practical solution to enhance PRISMA data usability in urban environments.

3.1. Introduction

According to the United Nations' 2018 *World Urbanization Prospects Report*, the proportion of the world's population living in urban areas is expected to exceed 68% by 2050 (United Nations, 2019), with this figure rising to 86% in developed regions. Consequently, cities must address their social and environmental vulnerabilities regarding the challenges posed by climate change (Alonzo et al., 2014; Gouldson et al., 2016; Laino and Iglesias, 2023). In urban environments, vegetation plays a pivotal role in terms of its ecological functions and its potential as a nature-based solution to the adverse consequences of climate change (Alonzo et al., 2014; Fu et al., 2022; Tanoori et al., 2024; Verde et al., 2024). Trees, in particular, perform important services such as improving air quality, reducing runoff and erosion, and lowering surface temperatures (Alonzo et al., 2014; Dian et al., 2016; Nowak et al., 2014). They also contribute to the aesthetics of the landscape and provide habitats and ecological corridors for a variety of species, increasing connectivity between areas of significant biodiversity (Malkoç, 2024; Morin et al., 2022; Valeri et al., 2021). Furthermore, trees have been shown to promote social cohesion (Mullaney et al., 2015) and economic growth (Thompson et al., 2021). There is also a growing interest in the carbon storage functions of urban trees and peri-urban forests (Pretzsch et al., 2023). Policy at all levels, from international to local, has come to recognize the importance of urban trees for human and ecosystem wellbeing and makes demands on public administrations to increase, monitor, and manage urban tree cover accordingly (UNITED NATIONS, 2021). For example, the United Nation's Sustainable Development Goal (SDG) 11.7 ("Sustainable Cities and Communities - Goal 11," 2015) and the *New Urban Agenda* (*New urban agenda*, 2017) both call for increasing equitable access to public green spaces. At a national level, the future fourth Italian National Inventory of Forests and Forest Carbon Pools, planned for 2025, will include an increased focus on urban forests (CREA, 2023). The National Biodiversity Future Center (NBFC) (Cena and Labra, 2024; "Urban environment and health - NBFC," n.d.), established as part of Italy's post-COVID-19 National Recovery and Resilience Plan (NRRP) (Fabbrini, 2022), is at the forefront of tackling biodiversity loss in Italy, which threatens essential ecosystem services.

However, implementing such policies is no simple feat. In increasingly complex governance systems, it often requires the coordination of very diverse stakeholders, including professionals and department directors working for municipal administrations, employees of private companies receiving public tenders, workers who carry out management tasks as a requirement for receiving public income or as rehabilitation, and non-profit associations, organizations, and citizens that adopt green spaces or volunteer their time for its upkeep (Comune di Napoli, 2021a). Such a complex sharing of responsibility for urban and peri-urban trees and forests depends on efficient and up-to-date monitoring.

Government agencies can improve their ability to monitor environmental resources and biodiversity conservation by using innovative tools and techniques. Indeed, information on the spatial distribution of tree species and vegetation maps are particularly useful for biodiversity monitoring (Casavecchia et al., 2020; Vihervaara et al., 2017). The availability of land cover information and the classification of urban tree species could be greatly facilitated by remote sensing (RS) with different data sources, such as very high resolution imagery, light detection and ranging (LiDAR) technology, and hyperspectral imagery (HSI) (Alonzo et al., 2014; Morin et al., 2022). The spatial resolution, radiometric resolution, and temporal resolution of imagery has increased with technological developments along with the availability of a growing number of satellite platforms (Filchev, 2014). Moreover, thanks to spectroscopy satellite missions, such as The Hyperspectral Precursor of the Application Mission (PRISMA) or the Environmental

Mapping and Analysis Program (EnMAP) hyperspectral mission, very high spectral resolution has been achieved (Qian, 2021).

PRISMA, launched by the Italian Space Agency (ASI) in 2019, and EnMAP, launched by the German Aerospace Agency in 2022, are both in operational phases (Caporusso et al., 2020; Storch et al., 2023). Both high spectral resolution imaging spectroscopy missions produce data with a 30 km swath width. PRISMA is a first-generation model to test and advance hyperspectral imaging technology for practical applications (Cogliati et al., 2021). EnMAP is quite similar and is also an experimental satellite (Guanter et al., 2015). By exploiting a very high spectral resolution, both missions provide additional information compared to multispectral missions, with which synergistic applications are expected (Caporusso et al., 2020; Guanter et al., 2015). Hyperspectral data are widely used for tree classification (Fassnacht et al., 2016) because they provide more accurate results (Dalponte et al., 2012). In particular, PRISMA data have shown excellent results in spectral separability compared to multispectral data (Vangi et al., 2021). Other platforms are also expected to become available soon, such as CHIME (Copernicus Hyperspectral Imaging Mission for the Environment), developed by the European Space Agency (Qian, 2021).

Hyperspectral data at a spatial resolution of 30 m × 30 m are excellent for classifying images in natural environments (Vangi et al., 2021). However, this spatial resolution is not ideal in urban environments, where images are typically composed of spectrally mixed pixels (Rosentreter et al., 2017), canopies are fragmented, and are often made up of different species grouped close together (Alonzo et al., 2014). Viable techniques that overcome these limitations and increase the potential of using HIS for urban classification include spectral unmixing and subpixel analysis (Palsson et al., 2018; Rosentreter et al., 2017). Recent developments in EO technology have also introduced alternatives that improve the spatial resolution of hyperspectral data using pansharpening, if the panchromatic band is available, or hypersharpening when data are fused with higher spatial resolution data, if available (Acito et al., 2022; Alparone et al., 2024).

Previous studies (Acito et al., 2022; Alparone et al., 2024; De Luca et al., 2024) have explored the potential of hypersharpening by showing that it is appropriate to use multispectral data with a medium resolution satellite, such as Sentinel 2, for data fusion with hyperspectral data. This technique requires both overlapping acquisition dates, as well as very reliable geocoding and the spatial alignment of the two datasets (De Luca et al., 2024). Pre-processed products that are easily and directly usable are provided by satellite data distribution agencies. For example, ASI distributes the L2D PRISMA data, an atmospherically corrected and orthorectified reflectance data (Cogliati et al., 2021). Of course, the orthorectification process is an essential step in data fusion involving products from different sensors, especially regarding areas with complex topography. Moreover, despite the convenience of L2D level preprocessing, the PRISMA technical documentation ("PRISMA Algorithm Theoretical Basis Document (ATBD)", 2020) guarantees a planimetric accuracy of no more than 200 m for standard preprocessing without ground control points (GCPs). Thus, fusing data from different satellites in urban areas poses significant challenges related to such factors as the presence of buildings and complex topography. Unless spatial misalignments are carefully addressed to avoid unreliable approximations, these procedures produce outcomes that are not always predictable and may be more complex compared to pansharpening.

In hypersharpening, algorithms must work with a sharpening image that was acquired by a different satellite and consequently shifted in time and taken from a different angle (Alparone et al., 2024, 2015). The use of coregistered panchromatic images would avoid these problems. It should be noted that pansharpening only improves the spatial resolution since it only uses the panchromatic band (Alparone et al., 2024). It is therefore of interest to understand whether the pansharpening techniques often used to improve image interpretation can also be used to improve data classification. One of the objectives of the PRISMA satellite, which is a precursor to the application mission, is to test the feasibility of pansharpening hyperspectral data using a coregistered pan image (Cogliati et al., 2021; Galeazzi et al., 2013), which can provide greater reliability and simplicity of use. This paper aims to respond to this challenge and show a case study example of a practical application.

Specifically, this study's main objectives are:

1. To evaluate the contribution of pansharpening to improving image classification accuracy using hyperspectral data so that it is also useful in an urban setting;
2. To apply the method to a real-world problem, specifically urban tree monitoring, through a simple pansharpening application that only uses the more easily accessible panchromatic band.

To achieve the first objective, results derived using an unrefined PRISMA image with a 30 m ground sampling distance (GSD) are compared to results obtained from classifying an enhanced PRISMA image that has a 5 m spatial resolution achieved through pansharpening. For this comparison, each result is statistically evaluated according to several accuracy metrics and ground truth points (GTPs).

To achieve the second objective, the study classifies the most common tree species in a selected region within the metropolitan city of Naples, Italy. Due to its high settlement density and relatively low amount of urban green spaces, Naples depends on the many services provided by urban trees and has been carrying out several initiatives over the past few years to improve and manage their urban tree cover. Tree inventories are an important tool in this regard but take up a significant amount of the public authority's resources, which could be used more efficiently with improved knowledge of trees' spatial distribution.

In order to carry out its objectives, the study is laid out as follows: Section 1 contains the preceding introduction describing relevant background information and identifying research objectives and contributions; Section 2 describes the materials and methods employed, beginning with a brief presentation of the study area, followed by a detailed explanation of the data preparation, the pansharpening method, and the classification procedure, including the related selection of ground truths (GTs) and classes; Section 3 contains the results, presenting the accuracy values obtained with the original image (GSD 30 m) and the enhanced image (GDS 5 m); Section 4 discusses key findings in the context of the literature and concludes with the investigation's main contributions, their implications for research and for practice, their limitations, and some suggestions for future directions.

Finally, this study makes the following contributions:

- It introduces a novel application using pansharpening techniques to improve classification performance by enhancing the spatial resolution of PRISMA hyperspectral data and demonstrates its efficiency with a case study example;
- It demonstrates a practical real-world use of pansharpened image classification for urban tree monitoring, which could help municipalities that are currently struggling to meet international and national policy demands.

3.2. Materials and Methods

3.2.1. Study area

The study area, shown in Figure 16, is an urban area located in the western part of the city of Naples, the regional capital of Campania in southern Italy. This study area presents an interesting opportunity to test out pansharpening in an urban area. Naples shares many struggles in managing urban trees common throughout southern Europe.

The metropolitan city of Naples has a population of just under 3,000,000 individuals (Istat 2023), and is spread over 1171 km^2 with an extremely high population density of 2519 residents per km^2 (ISTAT, 2011). In the European Commission's 2023 *Quality of Life in European Cities Perception Survey*, only 66% of participating residents reported being satisfied with their city, placing Naples 5th from the bottom in an investigation of 83 cities across the European Union (EU), European Free Trade Association (EFTA), the United Kingdom, the western Balkans, and Türkiye (European Commission, 2023). Aside from poor satisfaction with employment, safety, government, healthcare, public transport, and cultural facilities, Naples also stood out as ranking 8th from last for noise (only 38% of participants were satisfied with the noise level), 5th from last for satisfaction with cleanliness (25% satisfied), 6th from last for being a good place for older people to live (only 55% of participants agreed), 4th from last for being a good place for families with young children (only 58% agreed), and 2nd from last for satisfaction with public spaces (45% satisfied). All of these components contributing to quality of life are strongly related to the presence of urban green spaces, which provides opportunities for cohesion, abates noise, and improves city decor, among other benefits. That is why the Sustainable Development Goal (SDG) target 11.7 specifically aims to "provide universal access to safe, inclusive, and accessible green and public spaces, in particular for women and children, older persons, and persons with disabilities" ("Sustainable Cities and Communities - Goal 11," 2015). Most relevantly, Naples scored absolutely last for satisfaction with green spaces in the city (only 31% of residents were satisfied), with the report identifying a strong correlation between accessibility and spatial distribution.

Specifically, as of the city's last Tree Audit in 2021, the municipality of Naples included 5,554,236 m^2 of green spaces, which were challenging to maintain due to diminishing staff, which fell by 77% between 2016 and 2021 (Comune di Napoli, 2021b). Although the city was responsible for 50 public parks, only 36 of these were open to the public. However, at the time of the audit, the municipality was active in approving the financing and construction of several renovations and new parks, as well as for other urban greening measures.

In terms of tree cover, the municipality estimated having about 40,000 trees, based on a partial inventory of 28,213 specimens. A total of 9% of these were found to be at high or extreme risk of collapsing. In fact, between 2016 and 2021, 2791 trees had to be removed, mainly due to collapses or damage caused by extreme weather events. During the same time span, only 707 new trees were planted. However, at the time of the report, the city had just approved a plan to plant 5600 trees, replacing collapsed or unstable specimens, and adding new trees to city streets and public parks (Comune di Napoli, 2021b).

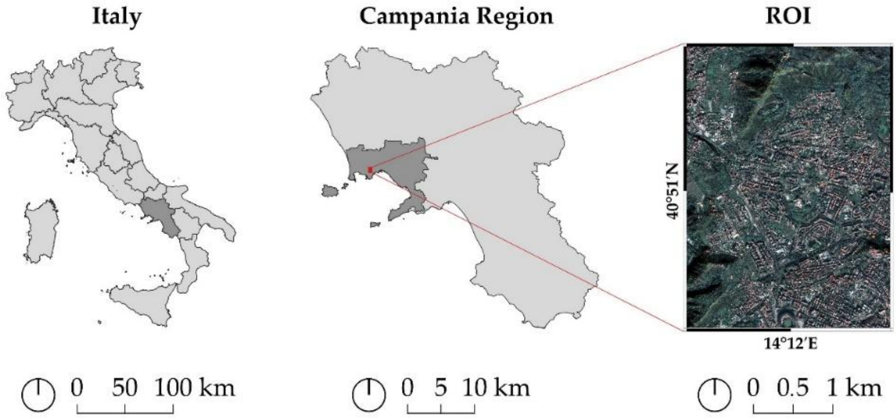

Figure 16: Study area—Region of interest (ROI).

The specific region of interest (ROI) that is analyzed in this study is a 2 × 3 km rectangle, with an additional 200 m buffer applied to avoid edge effects and potential errors in subsequent processing. Various reasons have led to the selection of this specific ROI as an emblematic case for an investigation into urban tree distribution. First of all, it meets the requirements of being in an urban context characterized by a densely built environment interspersed with vegetation and a significant presence of tree cover, as shown in Figure 17 (based on an analysis by the authors using the 10 m spatial resolution ISPRA 2021 Land Cover Map (ISPRA, 2021). The ROI is approximately 57% occupied by artificial surfaces, 19% by low vegetation, and the remaining 24% by tree vegetation). Furthermore, this area is characterized by a complex topography, with an elevation ranging from about 14 m a.s.l. to about 460 m a.s.l.

Finally, data coming from different sources were available for the area that could be used synchronously in order to test out the experimented classification method. In particular, for research purposes, the Public Greenery office of the Municipality of Naples made a particularly accurate forest inventory available containing the tree species present throughout the ROI, collected between 2016 and 2022 (A. Pepe, personal communication, March 2024). This information was used as a dataset for GTs. For the same area, a very high resolution (VHR) Pléiades image acquired on 11/17/2018 is available, along with a Digital Terrain Model (DTM) and a Digital Surface Model (DSM) collected between 2009 and 2012 and distributed by the Metropolitan City of Naples ("Città Metropolitana di Napoli - SIT," n.d.).

The ROI is within an HSI PRISMA view acquired on 11/04/2020. From a temporal perspective, the Pléiades and PRISMA images can be considered contemporaneous with the GTs, while the information contained in the DTM and DSM is about eight years older. This time interval was deemed acceptable for distinguishing between areas with low vegetation and wooded areas. The actual presence of trees was verified through photointerpretation of the VHR image to ensure the validity of the information contained in the DSM.

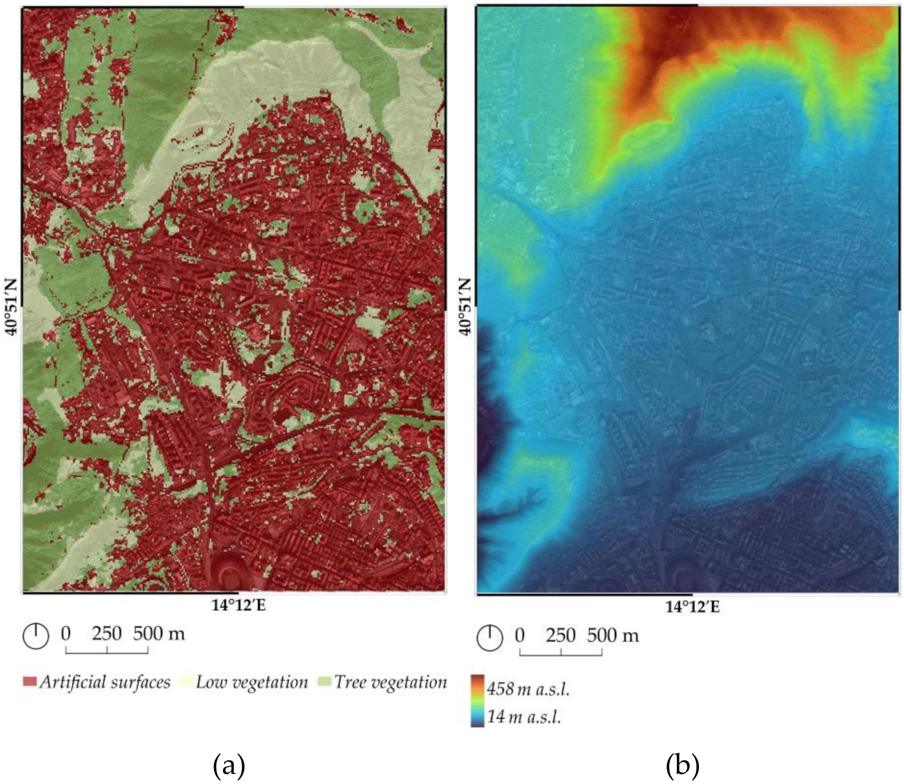

Figure 17: This figure shows the principal land cover class present and the altitude of the ROI: (a) using the ISPRA 2021 Land Cover Map; (b) using the DTM of the metropolitan city of Naples.

3.2.2. Pre-Processing and Identification of the Forested Areas

The methodology used for data preparation can be divided into two separate phases. In the first phase, the Pléiades image underwent preprocessing and then was used within the ROI in combination with the DTM and DSM difference to define a clipping mask that only included wooded areas and excluded low vegetation. In the second phase, a subset of the HSI was selected, both spectrally by eliminating the bands without information, and spatially by applying step one's filter with the clipping mask of the wooded areas.

Multispectral Dataset

All multispectral data from the Pléiades satellite is made up of four multispectral (MS) bands (blue = 0.43–0.55 μm; green = 0.50–0.62; μm; red = 0.59–0.71 μm; near-infrared = 0.74–0.94 μm), with a spatial resolution of 2 m, and a panchromatic band with a 0.5 m resolution that covers wavelengths between 0.47 and 0.83 μm of the visible spectrum (Perko et al., 2018).

The first phase of data preparation involved preprocessing the Pléiades image acquired on 11/17/2018 using PCI Geomatica 2017 software. Atmospheric correction was performed for both the multispectral and panchromatic bands using the ATCOR module, and pansharpening was carried out using the "High Performance Image Fusion" algorithm to achieve a 0.5 m resolution and spatial enhancement of the MS bands. Orthorectification of the image was accomplished using the OrthoEngine module with *Toutin's* mathematical model, utilizing GCPs and the DTM of the metropolitan city of Naples with a 1 m resolution. The processed data were then clipped to the ROI, resulting in the multispectral dataset (MS_DS) used for the subsequent phase.

In the second phase, a preliminary classification of the area was performed to distinguish trees from the rest of the land cover. The availability of the VHR MS_DS was crucial for this operation because the hyperspectral data alone, with a GSD of 30 m, would pose significant scale limitations in detailing individual tree canopies. Therefore, the MS_DS was segmented using eCognition Essential 1.30 software with the Multiresolution Segmentation algorithm. The segmented areas corresponding to tree canopies were separated from other segments in two steps.

The first step involved the separation of only vegetated areas, using the normalized difference vegetation index (NDVI) and only selecting areas with NDVI > 0.2, through the Threshold

Segmentation/Classification algorithm. NDVI, calculated as a ratio between near-infrared and red spectral reflectance, leverages the way photosynthesizing leaves reflect light. On land, NDVI values range from 0 to 1, where 0 indicates no plant cover, and 1 represents dense, healthy vegetation. Following Casalegno et al. (2017), an NDVI threshold (> 0.2) was used to detect all vegetation, including areas with lower photosynthetic activity.

The second step involved the separation of trees from grasslands and shrubs using the same algorithm but based on the normalized difference between the DSM and the DTM (nDSM) and only selecting vegetated areas with a height greater than 5 m. A DSM is a 3D model of the Earth's surface representing everything visible, including objects such as buildings and vegetation. A DTM is a 3D representation of the Earth's surface including bare-ground topography but excluding objects such as buildings and vegetation. This difference can be used to filter images for analysis, selecting only objects above the terrain. The vector data obtained at the end of this procedure containing polygons of the wooded areas was subsequently rasterized with a spatial resolution of 0.5 m and used as a clipping mask for the hyperspectral dataset (HSI_mask). The HSI_mask is shown in Figure 18.

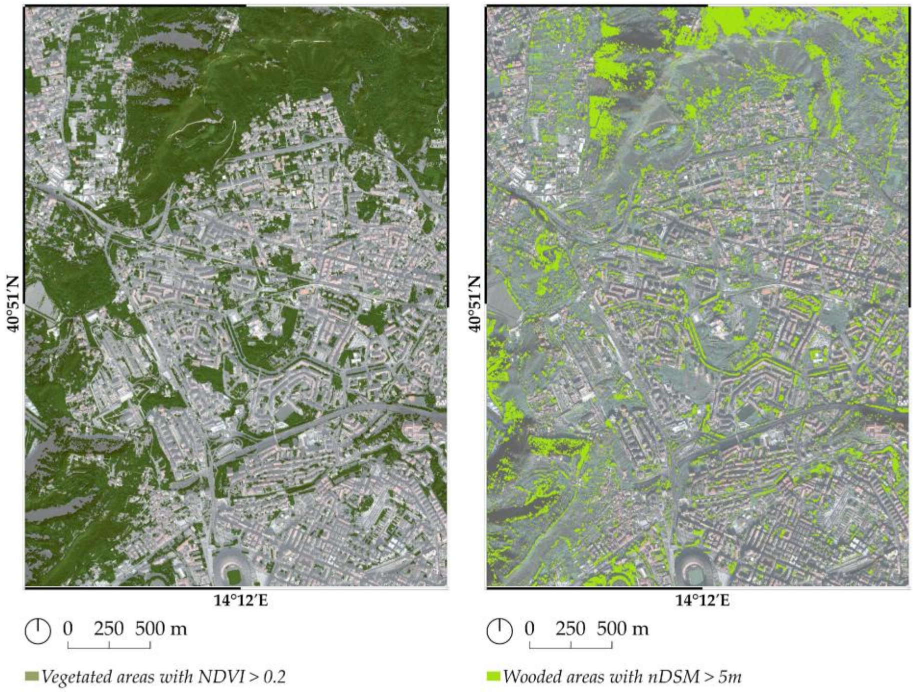

(a) (b)

Figure 18: This figure shows the main step used to separate tree canopies from other land covers using the MS Pléiades data: (a) map of vegetated areas with NDVI > 0.2; (b) map of vegetated areas higher than 5 m.

Hyperspectral Dataset

PRISMA data are made up of 66 bands in the visible and near-infrared (VNIR) range (400–1010 nm), 174 bands in the shortwave infrared (SWIR) range (920–2505 nm), which partially overlap, and one panchromatic (PAN) band (400–700 nm). The spatial resolution of the VNIR and SWIR is 30 m, while it is 5 m for the PAN. This study uses a level 2-D product. The data were first processed with a Python script (Prisma Tool) (LARP, 2023b) developed by the authors and freely available.

Using the Prisma Tool, the HDF5 file provided by ASI was converted into the GeoTiff format while simultaneously improving the georeferencing of the four corners of the view. As expected from the literature, three windows in the infrared range were completely opaque due to water vapor and other atmospheric gasses, causing a low signal-to-noise ratio. Thus, the data were filtered based on a statistical analysis using R software (v. 4.4.1), by removing the bands in the intervals from 1361 nm to 1449 nm, 1803 nm to 1949 nm, and 2483 nm to 2497 nm. This resulted in a hyperspectral dataset composed of 205 bands (HS_DS).

Pansharpening and Subsetting

Using QGIS (v. 3.34), two separate procedures were carried out to derive two HSI datasets from the HS_DS for classification purposes. For the first HSI (HSI1), the original spatial resolution of 30 m was maintained unaltered. For the second HSI (HSI2), the spatial resolution was increased to 5 m using the panchromatic band, as explained in detail below. Both HSIs were clipped after a precautionary buffer of 1 km was created around the ROI to avoid errors in the subsequent spatial alignment operations harmonizing the various datasets (HS1, HS2, MS_DS, HSI_mask, and GT points).

HSI1 was obtained through a simple merging of the 205 bands from the PRISMA data. To generate HSI2, four distinct steps were required. In step 1, the 36 bands in the PAN range (400–700 nm) with a GSD of 30 m were selected and merged into a single multiband raster file, keeping the value of the pixels contained in each band separate. In step 2, pansharpening was performed on the merged bands from step 1 using the PAN band as the sharpening band. This was accomplished using the GDAL library in QGIS and the Cubic resampling algorithm (4×4 Kernel), resulting in a new image with a GSD of 5 m. In step 3, the remaining 169 bands of the HS were merged, as in step 1, and their spatial resolution was reduced to 5 m through a downscaling operation, creating 36 new pixels for each pixel with a GSD of 30 m. In step 4, the pixel values contained in each of the original pixels with a

GSD of 30 m in the 169 bands were preserved and reassigned to the 36 new pixels generated within each original pixel. The images produced in step 2 and step 4 were merged into a new multiband raster file, producing HSI2. Figure 19 shows HSI1 and HSI2 before applying the HSI_mask.

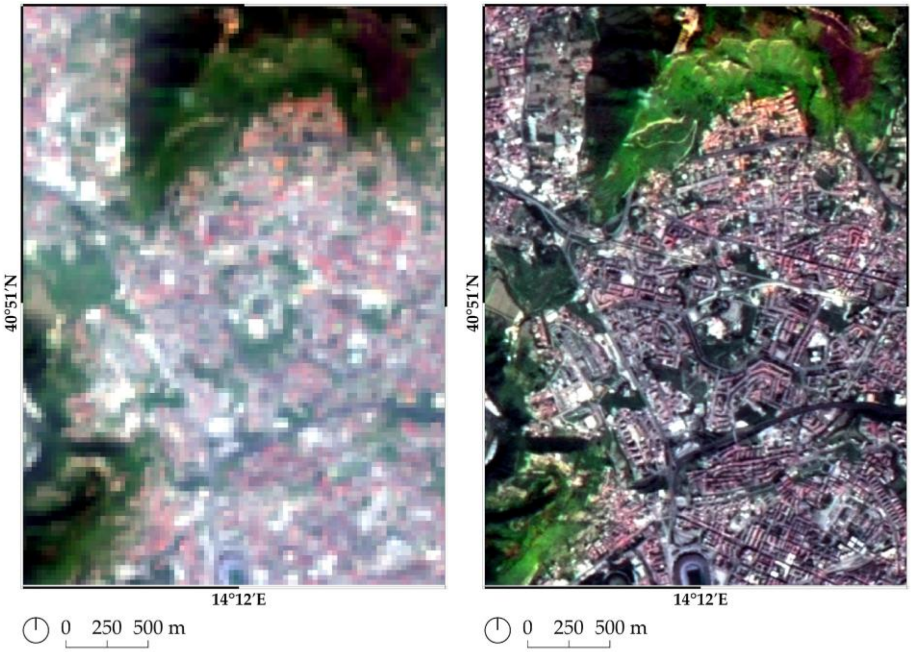

(a) (b)

Figure 19: This figure shows the two PRISMA HSIs clipped on the ROI in natural colors: (a) HSI1 with 30 m spatial resolution; (b) HSI2 with 5 m spatial resolution.

Both HSI1 and HSI2 were subjected to a georeferencing procedure. This was carried out to align the grids of both raster images and ensure that they matched the clipping mask of the wooded areas. The operation was carried out in QGIS using Polynomial 2 as the transformation type and Nearest Neighbor as the resampling method. The GCPs used in this process were collected using the Pléiades VHR image as a reference image.

Finally, a subsetting selection of HSI1 and HSI2 was performed using the HSI_mask as a filter to remove all pixels that were not of interest for classification. In the selected subset, all HSI1 and HSI2 pixels were retained where at least 30% of the pixel area was covered by the HSI_mask surface, and thus could be considered as corresponding to wooded areas. After trials with 40% and 50%, the 30% threshold was selected as the best trade-off for achieving good classification accuracy while retaining a high number of wooded areas or individual trees. In this way, the values for pixels in wooded areas were preserved, and the No-Data class was assigned to the portions of the HSI1 and HSI2 images corresponding to areas not of interest.

3.2.3. Classification Task

Ground Truth Dataset

The municipality of Naples' Office of Public Greenery keeps a vector point data-base of the tree specimens located in the urban area, including street trees and trees within public parks. There are approximately 1400 points within the ROI, representing 72 different species. The main purpose of this study is to compare the classification results of HSI1 and HSI2. For this reason, it was deemed appropriate to select the species for classification based on their frequency in the GTP dataset. The five species represented by more than 50 points are listed in Table 13, with the exception of *Ligustrum lucidum*. Other species represented by less than 50 points were not included in the classification, as they were represented by an insufficient number of points to validate the results. The *Ligustrum lucidum* class was excluded due to the small size of the specimens present in the study area. Also, all of the points representing the genus *Eucalyptus* spp. (*Eucalyptus globulus*, *Eucalyptus* sp.) were grouped into a single class included in the classification.

Table 13: This table contains the number of GTPs within the ROI used as reference data for the classification task.

Species	GTPs
Pinus pinea	424
Tilia × europaea	310
Platanus × acerifolia	103
Quercus ilex	51
Eucalyptus spp.	50
Total	938

The positions of the 996 GT points were verified one by one using MS_DS as a basemap and, where necessary, the points were placed correctly on their corresponding crown. The number of labeled pixels used as reference data in the following classification procedure is a little less than the number of GT points listed in the table above and slightly varies in the classification of HSI1 and HSI2, as the values in the Supplementary Materials show. This variation is due to the rare cases in which multiple points from the GTP dataset were located within a single pixel of the 30×30 m grid for HSI1 or the 5×5 m grid for HSI2. In these rare cases, a single labeled pixel was derived from multiple GT points.

HSI1 and HSI2 Classification

Deep learning models were used to classify HSI1 and HSI2, as they are able to learn nonlinear features of hyperspectral data compared to traditional machine learning algorithms (Ghasemi et al., 2024; Signoroni et al., 2019; Sothe et al., 2020). The classification of the PRISMA image was performed using a convolutional neural network (CNN) model with a structure that has been shown to be particularly suitable for land cover studies (Delogu et al., 2023; Lou et al., 2024; Ma et al., 2019).

Specifically, the classification procedure used the plugin AVHYAS in the open-source software Qgis 3.14. The AVHYAS plugin proposes various models of CNN; in this study, the model proposed by Hu et al. was chosen for its good results working with hyperspectral data (Delogu et al., 2023; Hu et al., 2015). It consists of five layers: the first layer represents the pixel spectral vector; followed by a convolutional layer; the max pooling layer; the fully connected layer; and the output layer.

The GT points were divided into three groups with different percentages. Thirty percent of the 938 points were reserved for the final classification test and separated from the remaining 70%, which was further divided into 70% for CNN training and 30% for model validation. The random selection of points for each of the three groups was repeated in a five-fold process assigning points to the training, validation and testing phases for both HSI1 and HSI2, corresponding to ten separate classification trials. The experimentation phase was conducted in successive iterations, where, under the same conditions, different points were selected for the training, validation, and test groups, alternating the two input HSIs.

In AVHYAS, the learning rate and the number of epochs were the only parameters that were changed during CNN tuning, while the other parameters were left at their default settings. Choosing the learning rate is important because if it is too small, it can slow down the process of adjusting the network weights to find the best solution, and there is a risk of ending up in a local minimum with a non-ideal solution. Conversely, if the learning rate is too high, a search for the minimum gradient that reduces the error rate may skip the ideal solution. An ideal learning rate of 0.001 was chosen, which is one of the most widely used values in the literature (Jena et al., 2021), based on the accuracy of the obtained results. The number of epochs was set to 200, which was empirically found to be an optimal number based on the accuracy achieved during validation. However, this number sometimes turned out to be lower due to an automatic arrest of the process to avoid overfitting the data. Both HSI1 and HSI2 images were classified using the same set of GTPs in each trial.

The quality of the classification was evaluated using some of the most common accuracy metrics: Overall Accuracy (OA), Kappa Coefficient (K), User Accuracy (UA), and Producer Accuracy (PA) (Congalton, 2001). Additionally, the F1 score (F1) was calculated, which is a metric derived from the harmonic mean between UA and PA and is more suitable in the case of an unbalanced label dataset among the various classes (Grandini et al., 2020; Naidu et al., 2023).

3.3. Results

This section presents the results obtained from classifying the two images, HSI1 (30 m GSD) and HSI2 (GSD 5 m). At the beginning of each trial, different points were randomly assigned to the validation and test groups, separating them from the points used for training. Specifically, the percentages of the 938 points allocated to the three different groups are: 30% for the final test of the results, 49% for training the CNN, and 21% for validating the classification model. In this way, two confusion matrices were generated for each trial, one for validation and one for testing, from which the accuracy metrics were measured. The twenty confusion matrices generated from the five trials are included in the Supplementary Materials along with the OA, K, UA, PA, and F1 values. For brevity, this section only reports the values related to the test phase of the results, which is deemed most representative of the trials conducted.

Table 14 contains the OA and the inter-rater reliability K coefficient obtained for every trial (T) relative to the test phase. The OA ranges in the results in the last row show that, on average, HSI2 achieves an accuracy value that is 0.14 points higher compared to HSI1. Similarly, the K values show an inter-rater reliability coefficient of 0.2 higher for the HSI2 image that has undergone pansharpening.

Table 14: This table relates to the test phase and shows the OA and K values obtained for every trial (T), the relative average values for each HSI and the interval between HSI1 and HSI2 metric averages.

	OA					
	T1	T2	T3	T4	T5	Av.
HSI1	0.65	0.67	0.65	0.60	0.61	0.64
HSI2	0.83	0.82	0.74	0.79	0.74	0.78
Interval						0.14
	K					
	T1	T2	T3	T4	T5	Av.
HSI1	0.48	0.47	0.46	0.32	0.34	0.41
HSI2	0.74	0.72	0.59	0.67	0.59	0.66
Interval						0.25

UA and PA are very useful for assessing the underestimation or overestimation of individual classes [58]. They complement commission error and omission error metrics. The values of these metrics for each test in the validation phase and in the test phase are shown in the Supplementary Materials. Table 15 shows the average value of UA and PA obtained in the test phase for all the trials performed with HSI1 and for all the trials performed with HSI2. In general, it is evident that the UA and PA values in-crease when the HSI2 image is used. The reasons for this improvement are related to the application of the pansharpening technique and will be discussed below. One aspect that must be emphasized here is that with the use of the HSI2 image, there is a reduction in both inclusion errors (commission errors) and exclusion errors (omission errors). This is driven by a substantial increase in both UA and PA. In fact, for the classes *Pinus pinea* and *Tilia × europaea*, for which the PA values are slightly higher than the UA values, the HSI2 image makes it possible to reduce the commission error margin, thus reducing the overestimation. For the other classes, where the UA values are greater than the PA values and thus underestimation occurs, a reduction in the omission error is obtained compared to the use of HSI1. The classes *Pinus pinea* and *Tilia × europaea* are slightly overestimated, while all the other classes are underestimated, using both HSI1 and HSI2. This phenomenon is probably related to the number of GTs, which is higher for *Pinus pinea* and *Tilia × europaea*, allowing a higher representativeness and avoiding the omission error.

Table 15: This table refers to the test phase and shows the average values of UA and PA. The average is calculated for the 5 trials using HSI1 and the 5 trials using HSI2.

Species	HSI1		HSI2	
	UA	PA	UA	PA
Pinus pinea	0.65	0.88	0.79	0.89
Tilia × europaea	0.63	0.67	0.84	0.86
Platanus × acerifolia	0.31	0.11	0.68	0.60
Quercus ilex	0.27	0.12	0.35	0.27
Eucalyptus spp.	0.56	0.14	0.82	0.34

Table 16 shows the results in terms of F1 related to the test phase of the five classification trials (T) conducted using the two images, HSI1 and HSI2. Furthermore, the table shows the average F1 obtained per class, along with the range that indicates the improvement generated by the use of pansharpening. The improved accuracy of the results demonstrates the effectiveness of pansharpening. With the higher resolution of the HSI2 image, the classifier can more accurately identify the spectral signature of tree species and assign pixels to the correct class. In contrast, the lower resolution of the HSI1 image makes this task more challenging, complicating the classification process. The pansharpening method makes it possible to emphasize the spectral characteristics of surfaces, even if only in the panchromatic range, by sharpening the values contained in the lower resolution pixels without altering the shape of the spectral signatures' curve. This makes it possible to distinguish pixels containing a mixed signature from several materials.

Table 16: This table refers to the test phase and shows the F1 values by class obtained with HSI1 and HSI2 in each trial (T), the relative average values for each HSI and the interval between HSI1 and HSI2 metric averages.

Species	HSI1 (F1)						HSI2 (F1)						
	T1	T2	T3	T4	T5	Av.	T1	T2	T3	T4	T5	Av.	Interval
Pinus pinea	0.75	0.78	0.74	0.71	0.73	0.74	0.86	0.86	0.81	0.83	0.81	0.84	0.10
Tilia × europaea	0.68	0.69	0.65	0.61	0.60	0.65	0.89	0.86	0.84	0.86	0.79	0.85	0.20
Platanus × acerifolia	0.40	0.22	0.00	0.00	0.14	0.15	0.75	0.79	0.32	0.68	0.62	0.63	0.48
Quercus ilex	0.41	0.00	0.00	0.00	0.18	0.12	0.50	0.47	0.11	0.29	0.00	0.27	0.15
Eucalyptus spp.	0.40	0.50	0.00	0.15	0.00	0.21	0.64	0.40	0.53	0.48	0.25	0.46	0.25

The fluctuations in F1 across the different trials show how the selection of GTPs for testing can lead to varying results, especially when the test is conducted with a relatively small number of points. The columns of average values indicate that higher F1s are achieved for classes with a greater number of GTPs. Even in cases where the F1 remains at very low thresholds, a substantial improvement can still be observed following pansharpening with HSI2, as evident from the last column. The classification results of all experiments with HSI1 and HSI2 are shown in Figure 20.

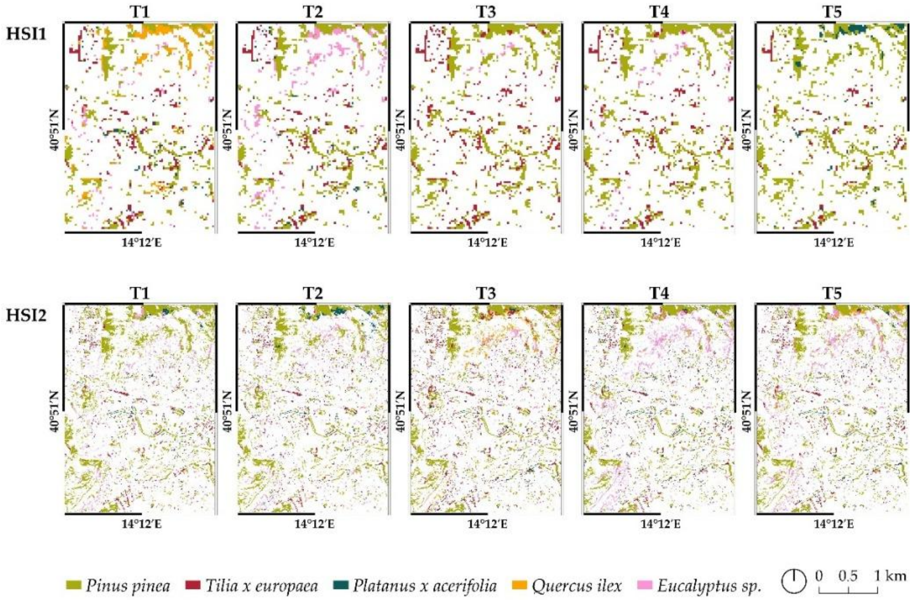

Figure 20: Classification results obtained in all trials (T) using HSI1 and HSI2.

3.4. Discussion

The investigation's results demonstrate that the direct use of pansharpening by taking advantage of the coregistered panchromatic data can lead to excellent classification results (OA from 0.64 to 0.78) in urban areas with complex topography, dense settlement patterns, and fragmented green areas (ISPRA, 2021). The UA and PA values can be increased, and both the commission error and the omission error can be reduced by using the improved hyperspectral data. The result is an improvement in the reliability of the classification map.

These key findings clearly show that the operation alone significantly improves the quality of the classification, given that the same conditions and software are used. For the classes under investigation with a larger number of GTs, the F1 value increased on average from 0.74 to 0.84 for the *Pinus pinea* class, and even more significantly went from 0.65 to 0.85 for the *Tilia × europaea* class. The classification of these two species benefits from a high number of GTs, and therefore the results confirm the efficiency of the proposed method. It can be stated that the application of pansharpening in an urban environment can lead to a considerable improvement in classification accuracy. Although other species with fewer GTs show even more pronounced improvements, these are less significant due to the smaller sample size of GTs.

The improved accuracy metrics (OA, K, UA, PA, and F1) show that pansharpening can be an affordable alternative for high spatial resolution hyperspectral data. The proposed method enhances spatial resolution by applying pansharpening to the hyperspectral bands in the range covered by the panchromatic band (400–700 nm), leaving the values recorded by the hyperspectral sensor in the other bands unchanged. The reconstruction of the details of the spectral signature and the spatial patterns is definitely more effective with the use of multispectral data over several intervals of the spectrum (De Luca et al., 2024). However, the pansharpening operation allowed the spatial distribution of the different surfaces to be highlighted without altering the shape of the spectral signature curve, especially in the mixed pixels of the 30 m resolution data. This process resulted in a better distinction of the spectral signature of the studied classes and improved classification accuracy. Thus, to improve the spatial resolution of the data without using laborious techniques, pansharpening the PRISMA data with the coregistered panchromatic band is a viable and accessible option.

One of the most promising applications of remote sensing technology is environmental resource and biodiversity monitoring. Research has been conducted evaluating the accuracy of image classification based on various data sources, including very high resolution imagery, nDSM, and HSI (Alonzo et al., 2014; Morin et al., 2022). Recent advancements in spectroscopy satellite missions, such as PRISMA, have made this last option much more accessible. However, existing open-access satellites provide images at a relatively coarse resolution (30 m or lower), which works quite well in larger natural environments (Vangi et al., 2021). However, a finer resolution is necessary in urban environments where images are typically composed of spectrally mixed pixels (Rosentreter et al., 2017), and canopies are fragmented and often made up of different species grouped close together (Alonzo et al., 2014).

Satellite HSIs typically have a spatial resolution of about 30 m and consist primarily of spectrally mixed pixels in urban contexts (Rosentreter et al., 2017). Hyperspectral data with higher spatial resolution can be acquired from airplane field missions with sensors such as CASI with a 2–5 m spatial resolution, depending on altitude (Qian, 2021), or restricted access satellite missions, such as TacSat-3 with a 4 m spatial resolution (Li, 2021). However, both of these sources pose data availability and accessibility problems for entities involved in biodiversity monitoring (government bodies, universities, non-profit organizations, etc.). Airplane missions only capture a small field of view and private or military high-resolution satellites are either too costly or too classified to be acquired. Thus, HSI remains one of the best options, if it can be refined to a higher resolution.

Viable techniques to address these limitations and enhance HSI for urban classification include pansharpening and hypersharpening, which improve spatial resolution by fusing data with higher-resolution sources. In fact, the validity of the pansharpening or hypersharpening methods to enhance HSI data from PRISMA while preserving the original spectral characteristics has been demonstrated (De Luca et al., 2024) by comparing the enhancement result with hyperspectral data acquired at the origin from higher resolution aircraft sensors (CASI/SASI). However, each one of these techniques has advantages and drawbacks. This study availed itself of pansharpening for the specific reasons explained below.

Research shows that using pansharpening to adjust the reflectance of hyperspectral data improves the spatial resolution of the new pixels.

However, this process only adjusts the intensity of the hyperspectral signature based on the panchromatic information, without adding any new radiometric information (Alparone et al., 2024, 2015; De Luca et al., 2024). Approaches proposed in other studies (Acito et al., 2022; Alparone et al., 2024; De Luca et al., 2024), which use hypersharpening with Sentinel data, would likely yield even more accurate results, particularly in flat areas where orthorectification of non-coregistered images is less challenging. In such a context, Hypersharpening may have some additional potential compared to single-band pansharpening.

Hypersharpening regards the fusion of higher spatial resolution multispectral data with hyperspectral data. Each of the multispectral bands is used as a sharpening band, as opposed to pansharpening, where only the panchromatic band is used. Hypersharpening allows the corresponding hyperspectral bands to be grouped using the wavelength range of each multispectral band. Hyperspectral enhancement is thus determined as a function of the values recorded by the multispectral sensor in different spectral regions, instead of just once for the entire panchromatic range, as in pansharpening.

However, while this technique certainly has advantages in terms of spectral signature reconstruction, it also has drawbacks. These are related to the use of scenes acquired by different satellites, at different times, at different angles, and using a mismatched orthorectification. This method relies on images taken from different satellites in different moments and thus demands high precision in orthorectification to prevent spatial misalignments and the overlapping of acquisition dates. Additionally, radiometric differences—due to factors like noise, sensor sensitivity, and atmospheric correction—can occur even for data captured on the same day (De Luca et al., 2024).

The pansharpening method proposed in this study uses a coregistered image to simplify processing, principally because the images are taken simultaneously, thereby avoiding the need for overlapping acquisition dates and complicated preprocessing (geocoding and the spatial alignment of the two datasets). Thus, it is the more practical choice for biodiversity monitoring in urban contexts.

3.5. Conclusion

This study aimed to achieve both a technical and a practical objective: to evaluate the contribution of pansharpening to improve image classification accuracy using hyperspectral data, so that it is also useful in urban settings; and, to apply this method to a real-world problem, specifically urban tree monitoring, through a simple pansharpening application that only uses the more easily accessible panchromatic band. In order to carry out these objectives, the classification accuracy results for some tree species obtained with HSI1 (GSD 30 m) and HSI2 (GSD 5 m) were compared. The results showed that pansharpening improves classification quality in dense urban areas with complex topography. In fact, pansharpened data led to significantly higher classification accuracy for all the examined species.

Through its investigation, this study made contributions by:

- introducing a novel application using pansharpening techniques to improve classification performance in urban environments by enhancing the spatial resolution of PRISMA hyperspectral imaging data;
- demonstrating its efficiency by applying the method to a practical real-world use of pansharpened image classification for urban tree monitoring.

Thus, dissemination of this method could improve HSI classification performance to help public administrations that are currently struggling to meet international and national policy demands to monitor biodiversity at various scales of governance.

In fact, the study's results confirm one of the objectives of the PRISMA mission, which is intended as a precursor to the applied mission: to evaluate the benefits of using coregistered panchromatic data (Cogliati et al., 2021; Galeazzi et al., 2013). To the best of our knowledge, there are no specific evaluations of pansharpening for PRISMA data based on the use of GTs for classification purposes in urban environments. Based on the results of this initial study, it could be said that the PRISMA mission has confirmed the usefulness of a panchromatic band sensor on hyperspectral satellite platforms.

Based on these findings, the following recommendations can be made. Firstly, it seems that hyperspectral data have potential to be used to differentiate the spectral signatures of trees in complex urban environments. Indeed, this technique addresses the needs of public administrations seeking to follow international and national urban forestry policies, recognizing the many contributions made by urban trees to health and wellbeing, ecosystem functions, biodiversity conservation, and sustainable development. In Italy, national legislation such as the *Regulations for the Development of Urban Green Spaces* (Italian Law n. 10, January 14, 2013) (Italian Republic, 2013) and the *Minimum Environmental Criteria (CAM) for Public Green Space Management Services and the Supply of Green Care Products* (Ministerial decree n. 63 of March 10, 2020) (Ministro dell'Ambiente e della Tutela del Territorio e del Mare, 2020) require municipal administrations to keep up-to-date georeferenced tree inventories specifying the number, species, health, and location of specimens and a plan for their management. This study was fortunate enough to be able to make use of an extensive inventory provided by the Public Greenery Department of the municipality of Naples. However, not all cities are able to keep up with policy demands. In fact, the same CAM legislation mentioned above was conceived to nudge municipalities into compliance by making up-to-date tree inventories and management plans a mandatory step in public procurement processes. The problem regards the limited number of public employees with the specialized skills necessary to create and update such an inventory and the huge amount of time such a feat requires. The approach proposed by this study could clearly be of great use to speed up this enterprise. By using hyperspectral data for initial classification, it is possible to provide a preliminary classification and then have field personnel focus solely on verifying changes over time, which can be identified using GIS techniques. Furthermore, the collection of GTs presents an interesting opportunity for municipalities to involve other stakeholders, such as educational institutions, associations, and citizens (Rossi et al., 2022).

This study's limitations are related to its focus on verifying the utility of pansharpening on PRISMA data by classifying tree species in an urban environment. While it successfully demonstrated that hyperspectral data with a 30 m resolution is useful not only in the field of forestry but also in urban areas, it was constrained by the availability of spaceborne hyperspectral data. Although easier to obtain than the other sources mentioned above, it still remains challenging for interested parties to acquire usable images in their ROI, under the conditions that they require (season, cloud cover, etc.). There is currently a very high demand for image acquisitions from users and a concentration of requests limiting the frequency of data availability (Shaik et al., 2023). The high demand for image acquisitions often makes it difficult to request new data as many users must wait their turn according to their priority status.

Future investigations could certainly start from the classification and spatial distribution of species carried out here and look more in depth at such phenomena as fragmentation and ecological connectivity in urban environments (Casalegno et al., 2017). Furthermore, the obtained results suggest that future analyses could identify individual species to uncover specific vegetation characteristics and detect potential diseases. Such an approach would likely yield statistically significant results and could provide a valuable foundation for urban, peri-urban, and rural forest inventories. Furthermore, hyperspectral data could be used to compare specimens of the same species that are in different contexts in order to study phenological differences, or health status in urban environments or as a response to climate change.

Today's environmental, climate, and biodiversity challenges require innovative solutions that can be implemented at various scales with limited resources. Technologies like remote sensing and AI offer precise tools for monitoring and management. International policies, such as Agenda 2030 and the Sustainable Development Goals, increasingly rely on data-driven and adaptive management approaches. PRISMA and other hyperspectral satellite missions can significantly contribute to these global efforts by providing data that, when enhanced through techniques such as pansharpening, become more applicable in urban environments. For effective urban tree management and improved policy implementation, it is crucial to leverage such advancements to ensure accurate, efficient, and actionable environmental monitoring.

Chapter 4

Leveraging the Potential of PRISMA Hyperspectral Data for Forest Tree Species Classification: A Case Study in Southern Italy

Gabriele Delogu, Miriam Perretta, Eros Caputi, Alessio Patriarca, Cassandra Funsten, Fabio Recanatesi, Maria Nicolina Ripa and Lorenzo Boccia

Published in Remote Sens. **2024**, 16 (24), 3730.
https://doi.org/10.3390/rs16244788

Abstract

Hyperspectral imagery and advanced classification techniques can significantly enhance remote sensing's role in forest monitoring. Thanks to recent missions, such as the Italian Space Agency's PRISMA (PRecursore IperSpettrale della Missione Applicativa — Hyperspectral PRecursor of the Application Mission), hyperspectral data in narrow bands spanning visible/near infrared to shortwave infrared are now available. In this study, hyperspectral data from PRISMA were used with the aim of testing the applicability of PRISMA with different band sizes to classify tree species in highly biodiverse forest environments. The Serre Regional Park in southern Italy was used as a case study. The classification focused on forest category classes based on the predominant tree species in sample plots. Ground truth data were collected using a global positioning system together with a smartphone application to test its contribution to facilitating field data collection. The final result, measured on a test dataset, showed an F1 greater than 0.75 for four classes: fir (0.81), pine (0.77), beech (0.90), and holm oak (0.82). Beech forests showed the highest accuracy (0.92), while chestnut forests (0.68) and a mixed class of hygrophilous species (0.69) showed lower accuracy. These results demonstrate the potential of hyperspectral spaceborne data for identifying trends in spectral signatures for forest tree classification.

4.1. Introduction

Environmental and biodiversity monitoring have become essential to preserving the planet in the face of human activity and climate change (Mittermeier et al., 2011; Pallotta et al., 2022; Randin et al., 2020). Forests are reservoirs of biodiversity (Hansen et al., 2021) and deserve special attention because the benefits humans receive from nature depend on their ecosystem functionality (Brockerhoff et al., 2017; Kacic and Kuenzer, 2022). Automated processes can support natural resource conservation, management, and promotion tasks by facilitating the large-scale availability of detailed and up-to-date land use (LU) and land cover (LC) information (Malinowski et al., 2020). In an era of global change, vegetation maps are critical for understanding and managing local to global biodiversity patterns (Casavecchia et al., 2020). Remote sensing (RS) is a practical and feasible solution for deforestation and forest degradation monitoring, and policies such as REDD (reducing emissions from deforestation and forest degradation in developing countries) could be based on above-ground biomass mapping alongside conventional field sampling (Goetz et al., 2009).

The potential of hyperspectral data to contribute to innovative research has been the subject of growing attention. Up until now, with the exception of NASA's pioneer Hyperion mission (Lim et al., 2019), these studies have been based on airborne data (Jia et al., 2020), or in some cases, on unmanned aerial vehicle (UAV) data (Capolupo et al., 2015). However, recent hyperspectral satellite missions such as PRISMA (Cogliati et al., 2021) and EnMAP (Storch et al., 2023), launched in 2019 and 2022, respectively, have added new tools to the field of Earth observation (EO). PRISMA hyperspectral imagery (HSI) has 240 bands with a bandwidth of 12 nm or less. The bands range from the visible/near infrared spectrum (400–1010 nm) (VNIR) to the shortwave infrared spectrum (920–2505 nm) (SWIR). The swath width at nadir is 30 km, the ground sampling distance (GSD) is 30 m for the hyperspectral bands and 5 m for the panchromatic band, and the radiometric resolution is 12 bits (PRISMA, 2020).

New hyperspectral missions such as PRISMA may increase the possibilities of innovative applications (Cogliati et al., 2021). In fact, PRISMA data have already been used for detecting and classifying non-photosynthetic vegetation (Pepe et al., 2020); geological applications (Tripathi and Garg, 2021); methane emission point mapping (Guanter et al., 2021); forest type discrimination (Vangi et al., 2021); fire fuel detection (Shaik et al., 2022); crop type mapping (Spiller et al., 2021); crop trait identification (Tagliabue et al., 2022); and local climate zone mapping (Vavassori et al., 2024).

However, hyperspectral data present its own challenges. The high dimensionality of HSI (Hughes, 1968) requires a significant number of ground truths (GTs) to maintain the accuracy of the classifier (Alonso et al., 2011; Richards and Jia, 2006). While band selection or feature extraction techniques can help handle data dimensionality (Hong et al., 2019; Landgrebe, 2002), GT availability remains a challenge, especially in developing countries as well as in areas with limited access. Furthermore, GT collection is a costly and time-consuming process. Common personal devices such as smartphones or tablets can facilitate data collection by a range of expert and non-expert users including professionals, scientists, or citizen scientists (Martinez-Sanchez et al., 2024; van der Velde et al., 2023). New user interfaces and applications facilitate contributions and simplify field surveys, expanding the amount of information and geotagged photos that can be used as reference data with appropriate pre-processing (Ferster and Coops, 2016; Kosmala et al., 2016).

In this framework, innovative EO programs should be considered together with innovative data collecting and processing technologies including artificial intelligence (AI) (Ghasemi et al., 2024). Both EO and AI techniques can significantly contribute to developing databases for decision support systems. In the last decade, there has been a renaissance of deep learning (DL) models, especially due to advancements in computer technology and improvements in image analysis (Ma et al., 2019). Before the advent of deep learning models, neural networks were overlooked in favor of traditional machine learning (ML) algorithms (Ma et al., 2019). The development of new AI algorithms has expanded the range of available classification techniques, allowing for extremely accurate LU and LC classification (Lou et al., 2024). Traditional ML algorithms have proven to typically not be well-suited for hyperspectral data and are being replaced by DL models (Ghasemi et al., 2024). The latter have shown great potential for the automatic learning of nonlinear data features that are difficult to detect through human analysis (Ghasemi et al., 2024; Hasan et al., 2019; Signoroni et al., 2019; Sothe et al., 2020). Some of the most widely used DL models are convolutional neural networks (CNNs) due to their architecture, which is particularly suited to hyperspectral data processing (Ma et al., 2019; Wang et al., 2021). CNN models have demonstrated impressive accuracy in previous studies related to tree species classification (Hasan et al., 2019; Wang et al., 2021; Zhang et al., 2020).

The use of satellite RS data for tree species classification has increased exponentially since 2005/2010, partly due to the availability of LiDAR and hyperspectral data (Fassnacht et al., 2016). The majority of these studies have been based on different types of data: passive optical multispectral or hyperspectral data; LiDAR; SAR; or the results of data fusion from different sources (Fassnacht et al., 2016; Zhong et al., 2024). Recently, Blickensdörfer et al. (2024) demonstrated that predominant tree species can be mapped on a national scale using a combination of Sentinel-1 and Sentinel-2 time series. Dalponte et al. (2012) combined high spatial resolution airborne hyperspectral data with multispectral satellite data and LiDAR to demonstrate that hyperspectral data provided the best results for classifying individual tree species in the southern Alps. Better discrimination of forest types using hyperspectral data was also shown in Vangi et al. (2021) by comparing the PRISMA and Sentinel 2 spectral separability metrics.

Considering these recent advancements, the aim of this study was to explore the applicability of PRISMA hyperspectral satellite data for tree species classification in a forest environment. One of the aims of the PRISMA mission is to test the hyperspectral data contribution in forest analysis and management (Shaik et al., 2023). To the best of our knowledge, no study has ever used PRISMA data to map land cover at the tree species level in a forest environment. Thus, the main novelty of this study lies in using spaceborne hyperspectral data in a forest context to distinguish forest classes based on predominant tree species. The investigation was conducted in a biodiversity-rich study area with different vegetation patterns where GSD could be a crucial factor.

Within this framework, the creation of labeled pixel datasets using GTs collected via smartphone apps QField (QField App, 2023) and EyeLand (EyeLand App, 2024) was also explored. This allowed the suitability of these data collection instruments to be tested for classifier training. Artificial intelligence-based classification techniques were applied in this study to classify the forest category according to the predominant tree species. Considering the model performance in our previous LC classification study (Delogu et al., 2023), a CNN was used to classify the PRISMA satellite data. While other models could be used, ML models have been shown to be less effective than DL models (Delogu et al., 2023; Ghasemi et al., 2024; Ma et al., 2019). Given that this study was not focused on innovating classification techniques, an established CNN model (Hu et al., 2015) was selected from the range of available DL models.

Specifically, the study's objective was to address the following research questions:

- First, is it possible to achieve a detailed classification at the forest category level, defined according to the Third Italian National

Forest Inventory (N.I.) (Gasparini et al., 2016), using PRISMA HSI, which coincides in some cases with individual tree species?

- Second, are the PRISMA data, with a GSD of 30 m, sufficient for the classification of forest trees in a context of high biodiversity and what accuracy level can be achieved with a single HSI?

4.2. Materials and Methods

4.2.1. Study Area

The study area, shown in Figure 21, is in southern Italy. The region of interest (ROI) is a square of about 441 km2 and includes the Serre Regional Natural Park [51] (excluding Lake *Angitola*), which covers an area of 17,700 Ha.

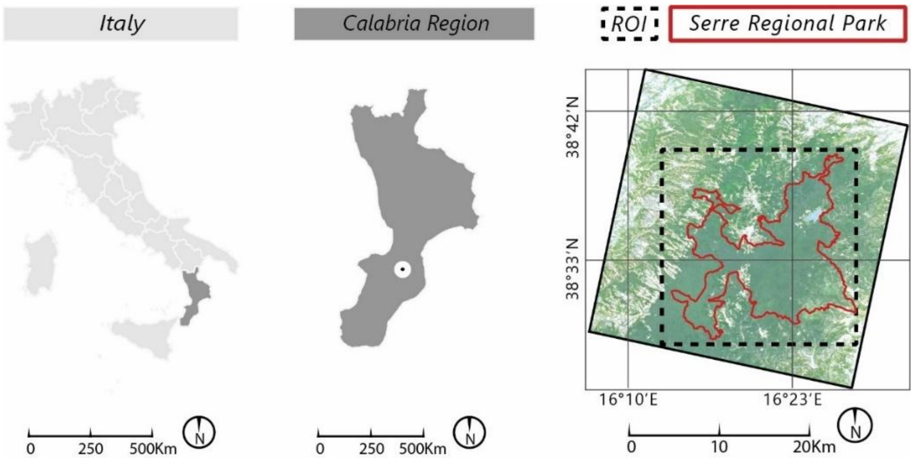

Figure 21: Framing of the study area. Authors' elaboration.

The study area is crossed by the Apennine Mountains and has an elevation between 800 m and 1400 m above sea level. According to the Köppen–Geiger classification (Kottek et al., 2006), the area's climate is classified as hot-summer Mediterranean (Csa) and partially as cool-summer Mediterranean (Csb) (Kottek et al., 2006; Rubel et al., 2017). The importance of the study area is also related to its latitude (about 38°N), which is extremely southern for the Csb climate. In fact, the site experiences an anomalously high rainfall for southern Italian climates; at the meteorological station of *Mongiana*, located at the center of the study area, the average rainfall is about 1600 mm per year (“Weather data archive | Mongiana (VV) weather station - MeteoNetwork,” 2024). As a result, forest growth has always been intense. Historically, the practice of selective logging has contributed to the mixed cover of some areas (Agnoletti, 2022; Siviglia, 2023). Other studies (Blickensdörfer et al., 2024) have shown that the combination of satellite imagery with environmental and climatic variables is useful for the classification of tree species on a large scale (e.g., national scale). However, in cases referring to smaller regions, the combination of satellite data with environmental variables has not necessarily led to significant increases in classification accuracy (Hemmerling et al., 2021). In this proposed case study, the study area corresponding to the PRISMA acquisition (900 km^2) was relatively limited. Therefore, climatic or environmental factors were not considered significant sources of enough internal variability within individual species to affect the spectral signature of each pixel. Furthermore, collecting many GTs for the same class in different regions of the image preserves the spectral variability representation within that same class, as shown below.

The study area contains the following Special Areas of Conservation (SACs) (“List of sites of Community importance,” 2024): SAC IT9350121; SAC IT9340118; SAC IT9340119; SAC IT9340120. These areas were included in or partially overlapped the park area, as shown in Figure 22.

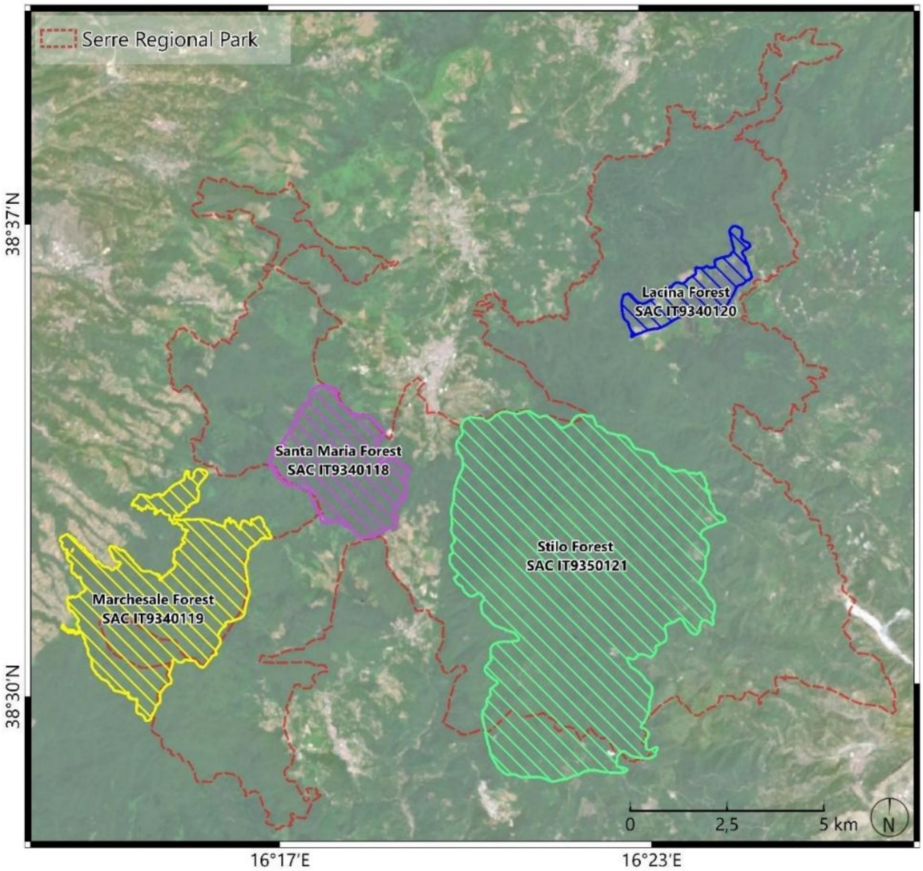

Figure 22: SACs areas included in the ROI.

The Park Authority provided some GIS layers related to the SAC's classification (Table 17). These data were useful for determining the number and predominance of forest types as well as their spatial distribution (Figure 23).

Table 17: Dominant LC classes in hectares per SAC.

Class	SAC IT9350121	SAC IT9340118	SAC IT9340119	SAC IT9340120	Tot. Class Area
Mixed areas (*Fagus sylvatica* and *Abies alba*)	3122	167	915	5	4209
Abies alba	1241	559	3	11	1814
Mixed areas (*Pinus nigra* and other conifers)		29	485	1	514
Castanea sativa	8	32	143		183
Quercus ilex	182				182
Pinus nigra	120	14		46	180
Areas with shrubs and herbaceous vegetation	24			75	99
Mixed areas (*Alnus glutinosa, Salix alba, Fraxinus excelsior*)		2		6	8
Fagus sylvatica	1				1
Alnus glutinosa		1			1
Total SAC area	4697	803	1546	143	

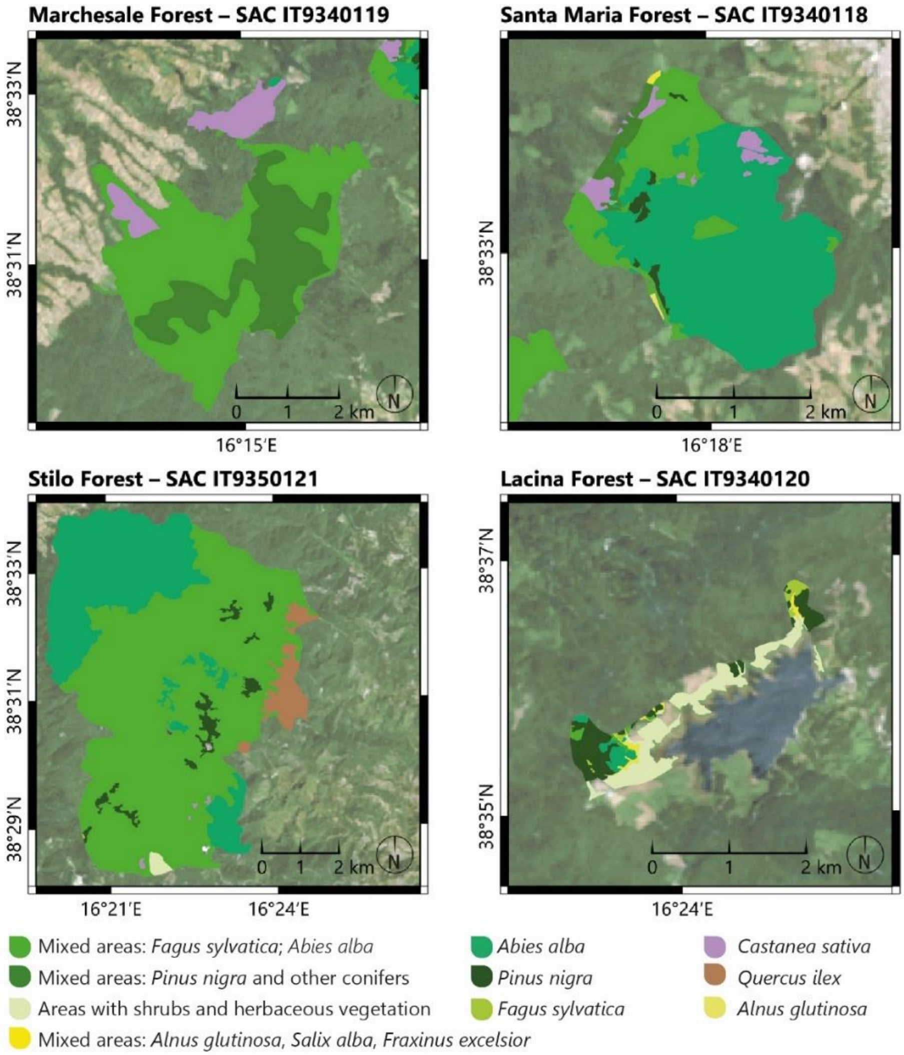

Figure 23: SAC forest type classification maps.

4.2.2. Ground Truths

Data collected in the field were used to train the classifiers and test the final results to ensure validity between the classification results and the real world. While the SAC classification map could have served as a reference dataset from which to derive the baseline truths for the classification process, the presence of many mixed classification areas made it unsuitable for the purpose of this study.

Instead, a field survey to collect GTs was conducted in March 2024. The survey was carried out with the assistance of the Park Authority, which helped to identify the tree species, particularly during a period when some species had dropped their leaves. EyeLand (EyeLand App, 2024) and Qfield (QField App, 2023) smartphone applications and the Geomax Zenith35 GNSS instrument were used to collect the field data. The EyeLand app was developed to facilitate GT point collection by non-expert users (EyeLand App, 2024), but in this pilot application, it was tested by the authors for ease of use without exploring a citizen science element. The accuracy of the GNSS position from smartphones, which always have a horizontal range of less than 5 or 7 m, was considered acceptable given the 30-m GSD of the PRISMA image.

The field survey guidelines of the N.I. (Gasparini et al., 2016) were used to organize the GT dataset. The species were grouped as shown in Table 18. The classes chosen in this study are indicated in the column "GT classes used". Category names were also included as metadata to provide information on the individual tree species as well as information on the surrounding habitat.

Table 18: Class definitions to generate the label dataset.

N.I. Macro Category	N.I. Code	N.I. Category	GT Class Used	SAC Class
Conifer forest	03	Silver fir forest	Fir forest	*Abies alba*
	05	Black pine, larch, and loricate pine forest	Pine forest	*Pinus nigra*
Deciduous broadleaf forest	08	Beech forest	Beech forest	*Fagus sylvatica*
	11	Chestnut forest	Chestnut forest	*Castanea sativa*
	13	Hygrophilous forest	Hygrophilous species	*Fraxinus excelsior*
				Alnus glutinosa
				Salix alba
Evergreen broadleaf forest	15	Holm oak forest	Holm oak forest	*Quercus ilex*

Shrubland, maquis	23	Maquis, Mediterranean shrubland	Grassland and shrubs	Area with shrubs and herbaceous vegetation

A total of 784 plots with an estimated minimum area of 30 × 30 m (PRISMA GSD) were collected in the field, resulting in a first dataset of labeled data (DS_1). DS_1 contained a total of 766 labeled pixels. The number of plots exceeded the number of pixels because multiple plots collected by different users were contained within the same pixel (900 m^2) in a few cases. Additional information recorded during the survey included an evaluation of canopy cover homogeneity outside the plot area. This evaluation was conducted within a variable radius that depended on the degree of canopy cover homogeneity, averaging about 100 m. This information was useful during postprocessing to label additional pixels, adjacent to those contained in DS_1, according to the information on the canopy cover homogeneity outside the plot area. In this way, it was possible to generate a second dataset with an additional 1865 labeled pixels (DS_2) using the information collected during the survey and through photointerpretation using the Google basemap in the Qgis software (version 3.34) (OSgeo, 2023). Figure 24 shows the distribution by class of the labeled pixels belonging to DS_1 and DS_2. It should be noted that only the plots belonging to DS_1, collected in the field, were used to test the final result in this study, ensuring greater scientific reliability.

The "Grassland and shrubs" class deserves special mention. For this class, no field plots were collected. As grasslands are easily distinguishable, photointerpretation in Qgis was used to obtain the 200 pixels belonging to this class in DS_2.

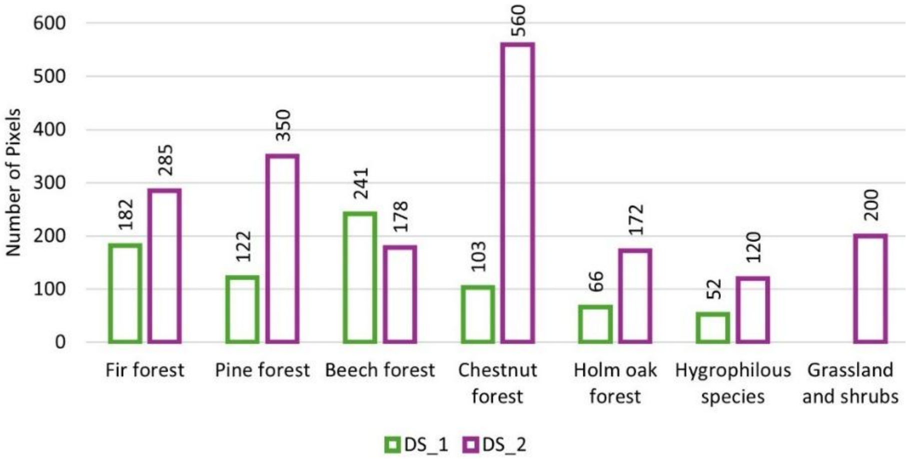

Figure 24: Labeled dataset. DS_1 indicates the labeled pixels corresponding to the plots collected in the field. DS_2 indicates the labeled pixels derived from the information collected in the field as well as from the photointerpretation.

4.2.3. Data Mining

This study used an HSI acquired by the PRISMA hyperspectral satellite on 25 July 2023. This was at the L2D level, the geocoded version of the L2C that is geolocated at bottom-of-atmosphere reflectance (Caporusso et al., 2020). LD2 images are atmospherically corrected and orthorectified by the Italian Space Agency (Caporusso et al., 2020). The PRISMA L2D level cube, provided in HDF5 format, was converted to GeoTiff format using a Python application developed by the authors and is available for download (LARP, 2023b). The same Python script was used to improve the georeferencing of the images by inserting the coordinates of the four scene vertices. This process resulted in the extraction of the original cube (Cube_O) with 234 bands. Cube_O was then subsetted to the ROI. This made it possible to include all of the polygons of the SAC areas (Figure 23) including those that lay partially outside the park boundary. Subsetting Cube_O produced Cube_S. To identify bands with missing information, an analysis of the pixel value distribution in Cube_S was performed using R software (version 4.3.0) to detect bad bands (Alicandro et al., 2022). These bands mostly corresponded to windows of the electromagnetic spectrum with zero transmittance values, associated with atmospheric noise (Flynn et al., 2020). A new cube (Cube_R1) was obtained after removing the bands highlighted in Figure 25 in the following ranges: bands from 104 to 112 (1361.0 nm to 1449.1 nm); bands from 147 to 163 (1803.5 nm to 1949.9 nm); bands from 232 to 234 (2483.7 nm to 2497.1 nm). Finally, the new Cube_R1 consisted of 205 bands.

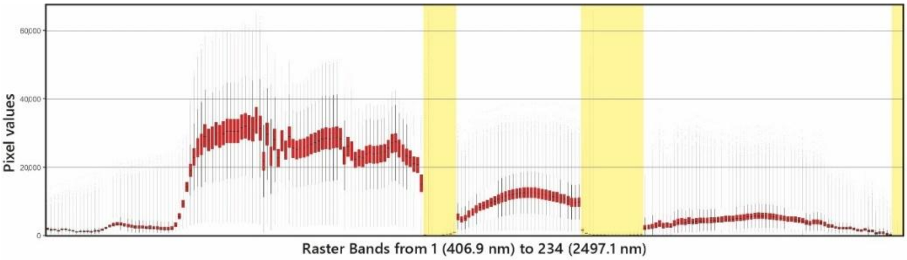

Figure 25: Distribution of the pixel digital numbers corresponding to the reflectance values. The graph shows the box plots for each of the 234 PRISMA data bands in red. The yellow highlighted areas correspond to regions where bands were removed.

Since classifiers and their results are known to be affected by data normalization and how it is performed, Cao et al. (Cao et al., 2017) suggested using the "band min–max" method for HSI classification. Therefore, using R software, Cube_R1 was normalized to obtain Cube_R1_N (normalized).

For the next steps, the pixels corresponding to the vegetated areas were isolated, and everything else was excluded. In order to do this, the normalized difference vegetation index (NDVI) was used, as it is a popular choice (Huang et al., 2021) for vegetation assessment. Several vegetation indices have been defined in the literature using both multispectral or hyperspectral data (Haboudane et al., 2004; Lemenkova and Debeir, 2023). Hyperspectral data, unlike multispectral data, have a series of narrow bands in both the red and infrared spectral regions. The NDVI was calculated following (Haboudane et al., 2004) using Formula (1), where R_x is the reflectance at a given wavelength (nm).

$$\text{NDVI} = \frac{(R_{806} - R_{664})}{(R_{806} + R_{664})}$$

The NDVI value distribution for pixels overlaid with ground truth datasets (DS_1 and DS_2) was examined to identify the pixels to be preserved. The median NDVI values were all above 0.6, as shown in Figure 26. However, in some cases, the values were lower considering outliers. Therefore, as a precaution, we decided to keep all pixels with an NDVI greater than 0.4, also considering the thresholds for different LC types reported by (Mehta et al., 2021). A mask was applied to Cube_R1_N, creating Cube_R1_M (mask), to only preserve the regions with values above this threshold. This step considered the areas of vegetation that were present at the time of the image acquisition (25 July 2023).

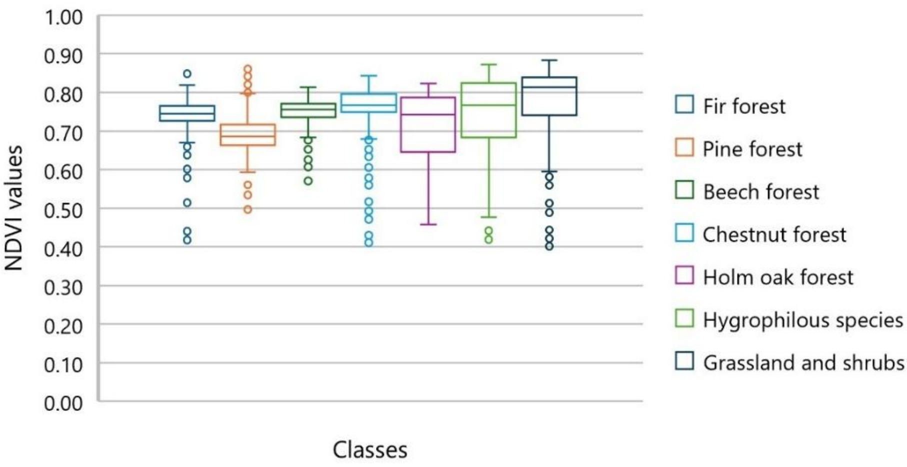

Figure 26: NDVI distribution by class of labeled pixels from the GT database.

Using hyperspectral data can be very challenging due to the large amount of information available and the time-consuming process required (Lou et al., 2024; Signoroni et al., 2019). Indeed, another process at this stage involves reducing the data's dimensionality to deal with the Hughes phenomenon (Hughes, 1968). Nevertheless, having many bands can improve the ability to discriminate between similar entities (Signoroni et al., 2019). Techniques for dimensionality reduction can be broadly classified into two categories: feature extraction and band selection. Methods based on feature extraction, such as principal component analysis (PCA), select a subset of features with a high variance from the original dataset (Jolliffe, 1986). However, these methods may result in information loss. Consequently, the band selection method is often favored when dealing with HSIs (Zhang et al., 2018), as this technique involves the selection of a subset of bands without compromising their physical interpretation (Sawant and Prabukumar, 2020; Yang et al., 2023).

In this study, three different banded HSIs were tested to evaluate the impact that the available spectral information might have on the accuracy of the results. Cube_R1_M with 205 bands was used in the first set of experiments. In this case, the band selection only involved removing the bands without information. The other two sets of experiments were performed with HSIs obtained through PCA. Considering the same number of principal components, the cumulative variance increased less rapidly for Cube_R1 than for Cube_R1_M, which only contained vegetated areas, as shown in Figure 27. For the first set, 30 principal components were selected. This made it possible to obtain Cube_R2_M and preserve 99.9% of the data variance. For the second set, 16 principal components were selected to evaluate the effect of halving the components while preserving a high percentage of variance. This resulted in Cube_R3_M, which retained 99.8% of the data variance.

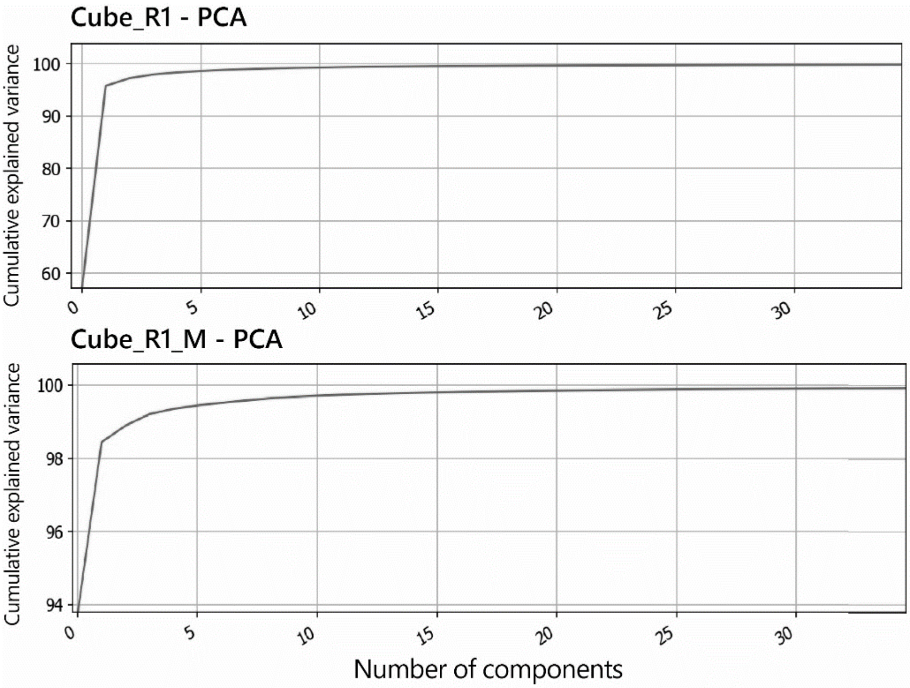

Figure 27: PCA of Cube_R1 and Cube_R1_M. This graph shows the growth of the cumulative variance as the components increase.

4.2.4. Classification Task

The remote sensing community is constantly investigating classification models that improve the accuracy of results. Prior to the development of deep learning models, neural networks were underutilized in favor of traditional machine learning algorithms such as random forest (RF) or support vector machine (SVM) (Ma et al., 2019). For HSI classification, previous studies have shown that DL models generally outperform ML models (Delogu et al., 2023; Ghasemi et al., 2024; Hasan et al., 2019; Sothe et al., 2020). As the focus of this paper was on an applied case study and not on a comparative analysis of classification models, we decided to use a DL model, taking into account the results of our previous study with PRISMA data (Delogu et al., 2023; Perretta et al., 2024). In this study, the AVHYAS plugin

(Lyngdoh et al., 2021), available in the open-source software Qgis, was used for the classification task. A CNN was used, since their architecture is particularly suited to processing large datasets such as hyperspectral cubes (Ma et al., 2019). Specifically, the CNN model proposed by Hu et al. (Hu et al., 2015) was selected. This model is composed of five layers: first, there is the input layer, represented by a pixel spectral vector, followed by the convolutional layer, the max pooling layer, the full connection layer, and finally, the output layer. The model was based on the spectral signature and does not consider spatial information. It was chosen because the spectral signature shape may be more relevant for class recognition than textures, patterns, or boundaries when using the PRISMA HSI with a 30 m GSD.

The classification was carried out for a total of 15 experiments, with 5 tests for each of the input datasets. The variations between the five tests for each input data cube were related to the selection of different labeled pixels stored in DS_1 and DS_2. The same percentage of random partitioning of DS_1 and DS_2 was used for each of the selections (Sel_1; Sel_2; Sel_3; Sel_4; Sel_5). Specifically, depending on the number of labeled pixels available for each class in DS_1, the selection percentage for test dataset creation varied: 40% was used to randomly select pixels for those classes with more than 100 labeled pixels, while the remaining 60% was merged with DS_2 to train and validate the model. For classes with less than 100 labeled pixels, the percentage for testing was increased to 80%, and 20% were merged with DS_2 for model training and validation. Thus, only the labeled pixels belonging to DS_1 were used to test the final map. The data from DS_1 that were not selected for testing were added to DS_2 data and used to train the network and validate the model performance. In particular, 70% of the data were randomly selected for training and 30% for model performance validation for all classes. Then, to reduce the dependence of the results on the specific selection of each experiment, a 5-fold selection was used, where a random selection of training, validation, and test pixels was repeated five times. The labeled pixels used at the end of each of the five random selections for training, validation, and testing are shown in Figure 28. These percentages were chosen based on what is commonly used in the literature (Sen and Keles, 2020). The possibility of reducing or increasing the number of labeled pixels used for the training, validation, or testing phases was not considered, given the good results obtained. Rather than testing the performance of the classification model, the usability of the PRISMA data to discriminate tree species was the main aim of this work.

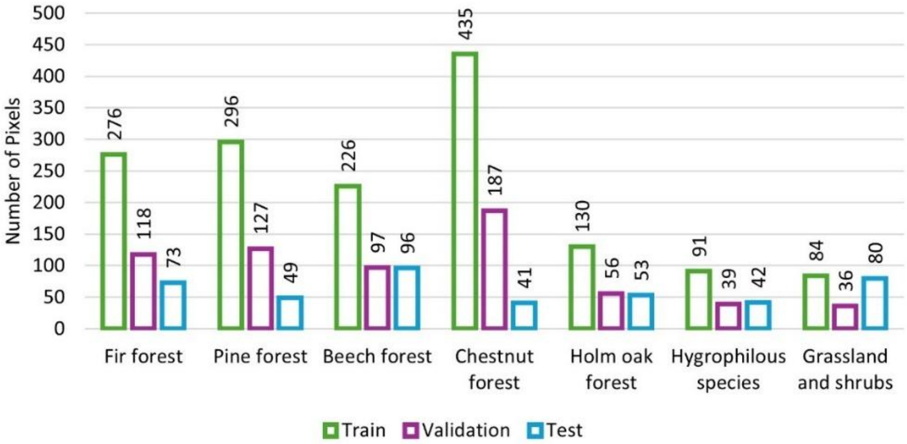

Figure 28: This graph shows the pixels used for training, validation, and testing in each of the five random selections.

Regarding the setting parameters of the chosen CNN model, an initial number of 200 epochs and a learning rate of 0.001 was used in all experiments, as these are the most common in the literature [76]. A number of experiments were carried out to test these values on the datasets used before choosing the values given above. An increase (0.01) or decrease (0.0001) in the learning rate resulted in lower accuracy (0.87 and 0.82, respectively) and higher loss (0.41 and 0.55, respectively). An increase (300) or decrease (100) in number of epochs resulted in lower accuracy (0.91 and 0.85, respectively) and higher loss (0.27 and 0.44, respectively). Based on these results, we decided to set the initial epochs to 200 and the learning rate to 0.001, since these values gave higher accuracy and lower loss in all experiments. The other AVHYAS plugin settings remained at their default values. As shown in Table 19, the model automatically stopped training early to avoid overfitting, resulting in a lower number of epochs in some experiments. Only the experiments with an accuracy above 0.9 and a loss below 0.2 were retained. The time required to classify the HSI (CNN training and validation) never exceeded 10 minutes (the tests were performed on an HP laptop with an AMD Ryzen 7 PRO 7840HS processor, a Radeon 780 M graphics card, 3.80 GHz, and 32.0 GB RAM).

Table 19: This table reports the CNN input data and shows the number of epochs, accuracy, and loss of the CNN used for each test.

Input	n. Test/Sel	n. Epochs	Accuracy	Loss
Cube_R1_M	1	165	0.955	0.145
	2	200	0.946	0.183
	3	152	0.946	0.177
	4	184	0.949	0.178
	5	200	0.945	0.171
Cube_R2_M	1	184	0.964	0.105
	2	200	0.963	0.111
	3	174	0.968	0.097
	4	188	0.966	0.114
	5	200	0.966	0.106
Cube_R3_M	1	200	0.972	0.089
	2	193	0.973	0.096
	3	200	0.950	0.137
	4	161	0.954	0.137
	5	195	0.969	0.124

Finally, the model was validated and the final classification map was tested. The metrics used in the statistical analyses of the accuracy evaluation were overall accuracy (OA), Kappa coefficient (K), user accuracy (UA), and producer accuracy (PA) [29,77], along with the F1 score (F1), which is the harmonic mean of precision and re-call and is another metric measured for each class [78]. It is useful for unbalanced datasets and ranges from 0 (worst) to 1 (best) [79]. The results related to the model vali-dation were automatically generated by the AVHYAS plugin. The results related to the final testing phase were generated using the SCP plugin [80] using the DS_1 GTs collected in the field.

4.3. Results

This section reports the results for the metrics used, calculated using the error matrices. All metrics are available in the Supplementary Materials (Table S1: Model_Validation_Test). Two matrices were generated for each test of the 15 experiments. The first was to validate the model and the second was to test the final map. In the following tables, the arithmetic mean (average) was added for each input as it is considered to be more representative than a single test (single selection of labeled pixels) and was calculated over the five results obtained from the five selections.

The following tables show the accuracy values obtained in all of the experiments. The scores relate to both the validation of the performance of the classification model and the testing of the final classification map. Table 20 shows the overall results in terms of OA, K coefficient, and F1 for each test. In the case of the validation phase, the highest OA was obtained using Cube_R1_M. Cube_R1_M also had a marginally higher K coefficient, while Cube_R2_M produced a slightly higher F1 value. Regarding the test results, the highest OA, both as a single test and considering the average value, was obtained using Cube_R2_M. Cube_R2_M also provided the highest K coefficient and F1 value.

Table 20: Validation and test results in terms of OA, K, and F1 for each test.

			VALIDATION			TEST		
Input	n. Test	GT	OA	K	F1	OA	K	F1
Cube_R1_M	Test_1	Sel_1	0.943	0.932	0.928	0.899	0.874	0.820
	Test_2	Sel_2	0.928	0.915	0.922	0.869	0.837	0.773
	Test_3	Sel_3	0.936	0.924	0.923	0.892	0.866	0.817
	Test_4	Sel_4	0.920	0.905	0.907	0.859	0.825	0.747
	Test_5	Sel_5	0.907	0.890	0.887	0.865	0.833	0.758
	Average		0.927	0.913	0.913	0.876	0.847	0.783
Cube_R2_M	Test_6	Sel_1	0.920	0.905	0.914	0.910	0.889	0.842
	Test_7	Sel_2	0.914	0.897	0.906	0.861	0.829	0.765
	Test_8	Sel_3	0.935	0.922	0.930	0.892	0.866	0.813
	Test_9	Sel_4	0.921	0.907	0.912	0.889	0.862	0.800
	Test_10	Sel_5	0.931	0.918	0.929	0.899	0.875	0.821
	Average		0.924	0.910	0.918	0.890	0.864	0.808
Cube_R3_M	Test_11	Sel_1	0.915	0.900	0.910	0.903	0.880	0.832
	Test_12	Sel_2	0.914	0.898	0.898	0.890	0.863	0.810
	Test_13	Sel_3	0.925	0.911	0.919	0.869	0.838	0.776
	Test_14	Sel_4	0.932	0.919	0.932	0.880	0.851	0.787
	Test_15	Sel_5	0.928	0.915	0.917	0.883	0.855	0.798
	Average		0.923	0.908	0.915	0.885	0.858	0.800

Table 21 shows the results in terms of the F1 for each individual class. The mean value is calculated for each of the five labeled pixel selections. The values in the table refer to both the validation (first number) and the map's test (second number) and are separated by a semicolon.

Table 21: F1 obtained for each individual class in each test. Values refer to both the validation (first number) and final classification map test (second number). Validation and test F1 scores are separated by a semicolon.

	Sel_1	Sel_2	Sel_3	Sel_4	Sel_5	Average
			Cube_R1_M			
Fir forest	0.91; 0.85	0.87; 0.77	0.90; 0.81	0.88; 0.80	0.86; 0.81	0.89; 0.81
Pine forest	0.93; 0.80	0.90; 0.75	0.90; 0.80	0.90; 0.75	0.85; 0.75	0.90; 0.77
Beech forest	0.95; 0.92	0.92; 0.84	0.95; 0.90	0.92; 0.87	0.93; 0.89	0.93; 0.88
Chestnut forest	0.95; 0.75	0.96; 0.69	0.97; 0.73	0.95; 0.63	0.97; 0.70	0.96; 0.70
Holm oak forest	0.92; 0.74	0.90; 0.78	0.91; 0.84	0.87; 0.72	0.80; 0.58	0.88; 0.73
Hygrophilous species	0.85; 0.73	0.86; 0.63	0.85; 0.73	0.78; 0.54	0.75; 0.64	0.82; 0.65
Grassland and shrubs	0.99; 0.95	0.96; 0.94	0.91; 0.91	0.96; 0.92	0.93; 0.95	0.95; 0.93
			Cube_R2_M			
Fir forest	0.85; 0.81	0.85; 0.75	0.89; 0.81	0.88; 0.84	0.87; 0.83	0.87; 0.81
Pine forest	0.88; 0.84	0.86; 0.71	0.90; 0.78	0.87; 0.79	0.91; 0.80	0.88; 0.78
Beech forest	0.94; 0.95	0.95; 0.86	0.94; 0.88	0.94; 0.92	0.96; 0.90	0.95; 0.90
Chestnut forest	0.95; 0.74	0.94; 0.63	0.97; 0.72	0.95; 0.65	0.95; 0.64	0.95; 0.68
Holm oak forest	0.93; 0.84	0.92; 0.79	0.89; 0.82	0.91; 0.81	0.90; 0.82	0.91; 0.82
Hygrophilous species	0.81; 0.76	0.79; 0.66	0.89; 0.71	0.86; 0.66	0.88; 0.80	0.84; 0.72
Grassland and shrubs	0.96; 0.96	0.94; 0.95	0.97; 0.96	0.88; 0.92	0.97; 0.97	0.95; 0.95
			Cube_R3_M			
Fir forest	0.87; 0.80	0.88; 0.76	0.87; 0.75	0.86; 0.81	0.89; 0.78	0.87; 0.78
Pine forest	0.89; 0.82	0.90; 0.80	0.89; 0.76	0.89; 0.77	0.92; 0.79	0.90; 0.79
Beech forest	0.92; 0.91	0.92; 0.90	0.98; 0.90	0.96; 0.92	0.95; 0.88	0.95; 0.90
Chestnut forest	0.93; 0.74	0.93; 0.71	0.94; 0.62	0.95; 0.63	0.94; 0.65	0.94; 0.67
Holm oak forest	0.89; 0.82	0.92; 0.86	0.90; 0.78	0.97; 0.79	0.90; 0.81	0.92; 0.81
Hygrophilous species	0.82; 0.75	0.72; 0.69	0.82; 0.70	0.86; 0.66	0.87; 0.71	0.82; 0.70
Grassland and shrubs	0.96; 0.97	0.90; 0.95	0.96; 0.92	0.97; 0.93	0.87; 0.97	0.93; 0.95

Considering the validation results, the best performance was obtained for the “Chestnut forest” class (0.96) using the Cube_R1_M. Results above 0.90 were also obtained for “Beech forest” and “Grassland and Shrubs”, regardless of the input data. The lowest model performance with both Cube_R1_M and Cube_R3_M was recorded for the mixed class “Hygrophilous species” (0.82). For the other classes, the CNN used achieved an average F1 ranging from 0.80 to 0.90.

In the case of the test results, considering the average value, the best accuracy in map classification testing among the tree species was obtained for the class “Beech forest” (0.90) using Cube_R2_M. Using the same dataset as input, results above 0.8 were obtained for the classes “Fir forest” (0.81) and “Holm oak forest” (0.82), while the “Pine forest” (0.78) class obtained a slightly lower F1. The lowest F1, regardless of the input data, was recorded for the mixed class “Hygrophilous species” (0.65) using Cube_R1_M and for the class “Chestnut forest” (0.67) using Cube_R3_M.

Figure 29 shows the distribution of the F1 values obtained by each of the classes in the fifteen trials in the validation phase. The classes with the largest ranges between the minimum and maximum values were the mixed class “Hygrophilous species” (0.17), “Holm oak forest” (0.17), and “Grassland and shrubs” (0.12). The rest of the classes showed less sensitivity to the HSI image used as input and/or to the selection of labeled pixels used for training and validation.

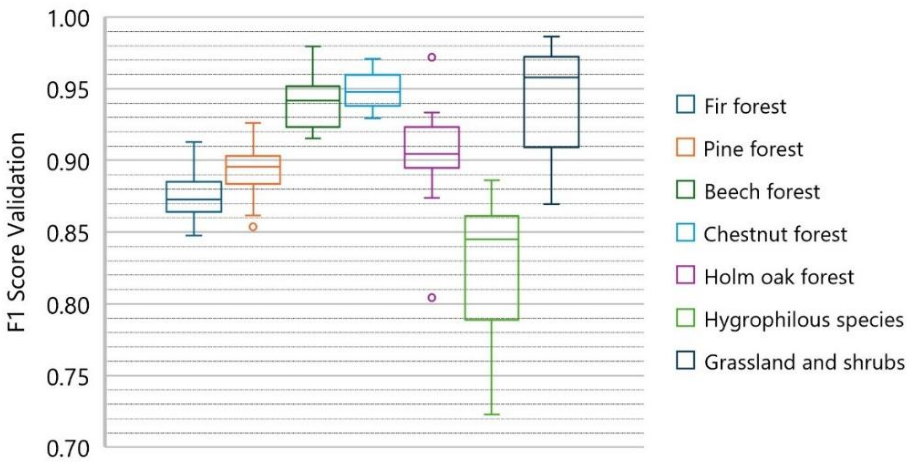

Figure 29: F1 distribution by class considering all the experiments. Values refer to the validation phase.

Figure 30 shows the distribution of F1 values obtained by each class using the three different inputs in the test phase. The highest differences between the minimum and maximum values were recorded with Cube_R1_M. The classes with the largest ranges were

"Holm oak forest" (0.26) and "Hygrophilous species" (0.19). The latter al-so showed a relatively large interval (0.14), as did the "Pine forest" class (0.13) when using Cube_R2_M. Using Cube_R3_M, the class with the largest interval was "Chestnut forest", which also had about the same interval when the other two HSIs were used as input. The other classes showed less sensitivity to the HSI image used as input and/or to the selection of the labeled pixels used to test the results.

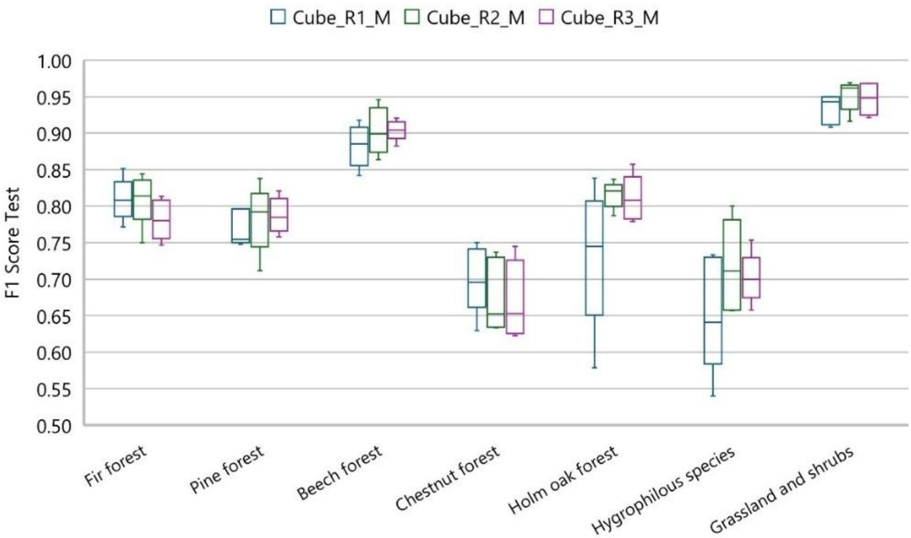

Figure 30: F1 scores by class, distinguished for each input cube. Values refer to the test phase.

Figure 31 shows the map obtained with Test_1, which was the test with the optimal reliability regarding the final scores, considering all 15 tests performed. Even if there was a trade-off for some classes in light of the higher results obtained in the other tests, Test_1 offered the best overall balance considering the values obtained in terms of F1.

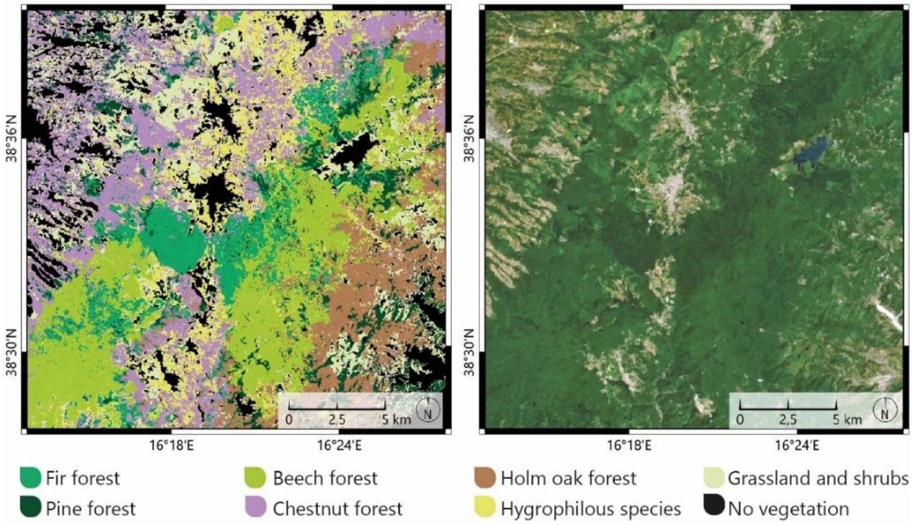

Figure 31: Classification map result from Test_1 on the left. PRISMA image in RGB composition on the right.

Finally, the results obtained in this study were compared with the pre-existing SACs LC classification in order to analyze their convergences and divergences, even though the latter contains more areas of mixed cover than polygons assigned to pure classes. The two classifications were overlaid and the class correspondences shown in Table 18 were used for the comparison. Figure 32 shows the results obtained in Test_1 within the perimeter of the SACs. Figure 33 shows what the composition of the SAC classes would be on the basis of the results of this study.

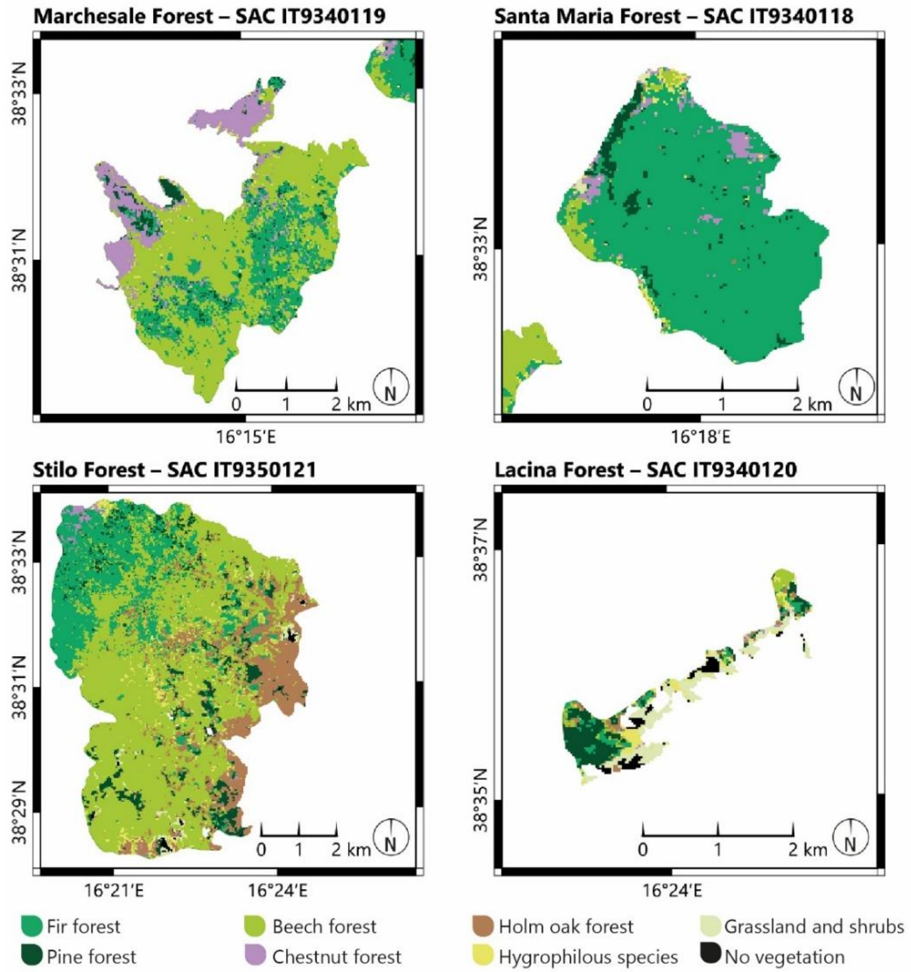

Figure 32: Classification results obtained in Test_1 within the perimeter of the SACs.

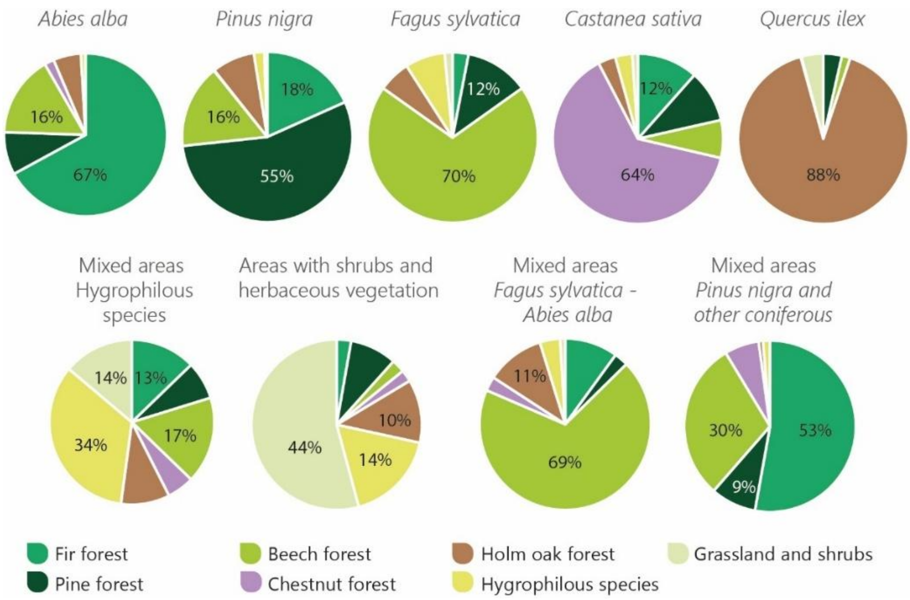

Figure 33: Composition of the SAC classes with respect to the results of this study (only the largest percentages are shown).

4.4. Discussion

The results obtained in this study confirm that hyperspectral data strongly increase the ability to discriminate between similar entities in forest classifications, consistent with findings in previous studies (Bandyopadhyay et al., 2023; Dalponte et al., 2012; Lim et al., 2019; Vangi et al., 2021). Furthermore, the ability of DL models to handle HSI data (Ghasemi et al., 2024; Signoroni et al., 2019; Sothe et al., 2020) was demonstrated by the accuracy values obtained in the model validation of the CNN used (Hu et al., 2015; Lyngdoh et al., 2021). The results showed rather high values for all accuracy metrics used, considering other studies aimed at using RS to classify tree species (Fassnacht et al., 2016). The case study results showed an average OA of 0.92 in the validation phase and an average OA of 0.88 in the test phase. The average K was 0.91 in the validation phase and 0.86 in the test phase, while the average F1 was 0.92 in the model validation phase and the average F1 of 0.80 in the test phase. For most of the classes considered, higher results were obtained (around 0.90 in terms of F1) when considered individually.

Fassnacht's review of tree species classification from RS data (Fassnacht et al., 2016) discusses the concept of accuracy in classifying tree species. According to Foody (2002), the level of accuracy can depend on the needs of the user and the type of application. Some authors of reviewed papers (Goodenough et al., 2003; Heikkinen et al., 2010; Korpela et al., 2010) set an OA target for forest type mapping (80% in northwestern USA and 95% in Finland). Thomlinson et al. (1999)set a minimum OA of 85% for land cover studies and a minimum of 70% for individual classes.

Since there are no similar studies on PRISMA data classification for tree species recognition using CNNs in forests, the results of this study could only be compared with similar studies regarding the satellite data used, the classification model used, or the object of classification. Rogers et al. (2024) classified 21 land cover types using PRISMA data with an average balanced accuracy of 76% and an F1 of 77%. Vanguri et al. (2024) classified tree species using EnMAP hyperspectral data combined with Sentinel using ML algorithms and achieved the best results in model validation with SVM with an average OA of 0.94 between the deciduous and coniferous LC. Dalponte et al. (2012) obtained the best K accuracy (88%) in the validation of the classification of five forest types using SVM on a combination of 30 hyperspectral and LiDAR bands. Fricker et al. (2019) achieved an average F1 of 0.87, classifying seven tree species using CNN and high spatial resolution airborne hyperspectral data. Comparing the accuracy achieved in this study with these previous forest classification studies demonstrated that using a single PRISMA HSI dataset could yield quite accurate classification results.

It is also interesting to compare the results obtained in this study with the classification of the SACs in order to analyze their convergences and divergences, even though the latter contained more areas of mixed cover than polygons assigned to pure classes. The predominant class in the PRISMA classification was the same as in the SAC classification in the homogeneous SAC polygons. Nevertheless, other classes with lower percentages were also included in these areas due to the higher level of detail in this study. In the mixed cover polygons, the SAC classification and the results of this study also agreed in terms of the prevalent species. An exception was the class "Mixed areas (*Pinus nigra* and other conifers)", where the dominant species in this study was "Fir forest" due to the class polygon extent and difficulty in distinguishing conifers in SAC classification.

As shown in Vangi et al. (2021), PRISMA's spatial resolution does not limit its application, and its spectral resolution makes it possible to discriminate between similar forest types. Indeed, it has been shown that hyperspectral data are less dependent on GSD (Goodenough et al., 2003), and high spatial resolution does not necessarily lead to more accurate results (Liu et al., 2020). However, the GSD of PRISMA HSI deserves more attention, even though it appears to be effective in areas of mixed coverage. Spectral unmixing techniques seem very promising and may lead to a better interpretation of the spectral composition in the future (Palsson et al., 2018).

There is not always a strong correlation between the accuracy values and the availability of labeled pixels as it depends on the class type and its spectral response. Classes with fewer samples, such as "Grassland and shrubs" and "Hygrophilous species", showed significant differences in F1 values because mixed classes have inherently inhomogeneous characteristics.

The very high accuracy values obtained may be an indication of possible overfitting, also in light of the size of DB_1 and DB_2. However, regardless of the labeled pixels selected for training, validation, and testing, the resulting accuracy values were nearly stable. This stability, together with the early arrest of the classification model in the training phase described in Section 2.4, prevented overfitting in the final classification. Even when considering cases where a decrease in accuracy was observed, the results remained consistent with values reported in other studies (Bandyopadhyay et al., 2023; Zhong et al., 2024). Nevertheless, a larger labeled dataset could result in less variation in accuracy across trials. When the statistical sample size is modest, a significant increase or decrease in accuracy may be more influenced by the labeled pixels used in the sample than by actual variations in the model predictions. Hyperspectral data are notorious for the large amount of sample data required, especially when DL models are used. In this study, the representativeness of the data for CNN training was enhanced by adding approximately 1800 additional labeled pixels (DS_2) from the smartphone app to the approximately 750 plots collected in the field. The additional dataset was added based on the information and photos collected with the smartphone app. This shows how personal devices can facilitate data collection by expert users and may indicate the potential of expanding its use to non-experts through citizen science.

An important consideration is that the results were based on a single image. It is likely that the results could be further improved with multitemporal analysis or by combining different sources (e.g., LiDAR). The wide availability of long time series of multispectral data remains a valuable tool. Recently, Blickensdörfer et al. (2024) demonstrated that major forest species can be mapped using a combination of Sentinel-1 and Sentinel-2 time series. However, the potential of hyperspectral data seems to guarantee excellent results, even with limited acquisitions and in areas of mixed forest cover.

Optical sensors have been used to measure the aboveground biomass over large areas by linking reflectance variations to field measurements, however, canopy structural conditions can change more rapidly than a satellite temporal resolution can record (Goetz et al., 2009). In the case of hyperspectral missions such as PRISMA, this problem can be exacerbated by infrequent data acquisition (Shaik et al., 2023). An overview of the strengths and weaknesses of the PRISMA mission is reported in Shaik et al. (2023). Some weak points are related to the difficulty in accessing data compared to the high number of requests and the long revisit time in the same area of ~16 days (Shaik et al., 2023). However, data fusion with high temporal resolution multispectral sensors such as Sentinel may provide a solution, combining the high spectral resolution of the original hyperspectral dataset with the temporal repeatability of multispectral data (Alparone et al., 2024).

4.5. Conclusion

This paper explored the use of PRISMA data for forest classification and provides results confirming that: (1) a detailed classification at the forest category level can be obtained using PRISMA HIS and (2) the PRISMA data's GSD of 30 m is sufficient for the classification of forest trees in a context of high biodiversity and can achieve a high accuracy level with a single HSI. However, a higher accuracy was observed for pure cover with respect to mixed cover. This indicates that without additional processing, such as spectral unmixing, the classification of HSI with 30 m GSD is less effective in mixed cover cases. The study also dealt with the need for data dimensionality reduction. The best overall balance in accuracy validation and testing was achieved using the 205-band cube, but fewer bands can also yield high accuracy when fast processing is required. Finally, the paper demonstrated the potential of using smartphone apps to collect GTs. It should be noted, however, that the post-processing of such data is time consuming and requires a thorough verification of each labeled pixel.

This study was limited by the current scarce availability of hyperspectral data. There are few active hyperspectral satellites, and weather conditions often prevent regular acquisition. Indeed, the use of a single satellite image, rather than a time series or a combination of different sources, is certainly a limitation of this study. However, given the scarcity of data in certain regions, the possibilities offered by a single PRISMA image appear very promising. Depending on the purpose of the study, a single image could provide sufficient accuracy without resorting to multitemporal analysis or data fusion. The imminent launch of further hyperspectral missions could also help to overcome the limited availability of hyperspectral satellites.

Possible directions for future research include the combination of PRISMA data with radar or higher resolution imagery and leveraging networks of field data collectors. The production of detailed land cover maps with HSI could enable tree species to be correlated with vegetation indices to measure vegetation health. Finally, it should be noted that the availability of current data, HSIs, and GTs will be extremely powerful in the future. For example, comparisons of the effects of climate change based on data collected in previous years will be possible in the future as scientific knowledge and more advanced technological processing tools become available.

Chapter 5

Comparing forest tree species classification models across Italy using PRISMA, Sentinel-2, and simulated Landsat next data

Gabriele Delogu, Dirk Pflugmacher, Lorenzo Boccia, Patrick Hostert

Under review

Abstract

Forests provide essential ecosystem services, yet monitoring their composition remains challenging due to limited accessibility and resources. Remote sensing technologies offer effective alternatives, with multispectral satellite time series (e.g., Sentinel-2) widely used for tree species mapping. Hyperspectral missions such as PRISMA promise further improvements, though large-scale applications remain underexplored. This study tested the generalizability of PRISMA-based tree species classification models across six environmentally diverse sites in Italy and compared their performance with Sentinel-2 time series and simulated data from the forthcoming Landsat Next mission. Results show that site-specific models offer slightly better accuracy, yet generalized models still provide reliable classifications, particularly for dominant Italian tree species. PRISMA hyperspectral data yielded higher accuracy than single Sentinel-2 acquisitions and results comparable to Sentinel-2 time series, while Landsat Next demonstrated strong potential despite relying on fewer spectral inputs. The findings highlight both the promise and challenges of hyperspectral remote sensing, emphasizing the need for robust reference datasets and careful consideration of mixed forest cover. Integrating Earth Observation data with field inventories will be crucial for advancing forest monitoring, supporting management, and addressing climate change impacts.

5.1. Introduction

Preserving forests is essential due to the vital ecosystem services they provide (Brockerhoff et al., 2017), including the conservation of habitat and biodiversity (Mori et al., 2017), water and climate regulation (Ellison et al., 2017), and carbon sequestration (Pan et al., 2024). Climate change impacts the growth dynamics and distribution of forests and the spread of disturbances (Hof et al., 2017). Information about tree species is essential for forest management and protection, to safeguard biodiversity (Randin et al., 2020; Vihervaara et al., 2017), and to develop climate change mitigation and adaptation strategies (Vanguri et al., 2024). Tree species diversification further enhances forest resilience by reducing susceptibility to pathogens and wildfires (Field et al., 2025; Fuentealba et al., 2013). However, the human and economic resources necessary for monitoring forests are not always available. Furthermore, rural areas are often not easily accessible, especially mountain regions. Earth Observation (EO) programs provide a valuable addition to field data and are cost-effective technologies for monitoring forests (Massey et al., 2023), helping decision-makers to understand and manage biodiversity patterns (Casavecchia et al., 2020), as evidenced by the growing number of studies using remote sensing data for tree species classification (Fassnacht et al., 2016; Pu, 2021).

The most promising and widely used approach for large-scale tree species mapping currently relies on multispectral satellite time series, such as Sentinel-2 (S2) and Landsat. These satellite programs provide global observations at medium spatial resolution with relatively high temporal resolution, making them well suited for long-term monitoring of land cover and forest conditions (Massey et al., 2023; Phiri et al., 2020). Recent studies have shown that phenological information contained in dense multi-spectral time series substantially improves the classification of tree species (Blickensdörfer et al., 2024;

Bolyn et al., 2022; Francini et al., 2024; Grabska et al., 2019; Hemmerling et al., 2021; Liu et al., 2024; Wegler et al., 2025). For example, Hemmerling et al. (2021) and Blickensdörfer et al. (2024) used S2 and Sentinel-1 time series to map tree species in Germany. Bolyn et al. (2022) used a cloud-free S2 time series to classify nine species in the Wallonia region of Belgium. Francini et al. (2024) used S2 time series and harmonic functions to improve the classification of tree species for the Netherlands, and Grabska et al. (2019) showed an improved performance of S2 time series vs single S2 images for mapping nine tree species in *Baligród* Forest District (Poland). In Canada, Hermosilla et al. (2022) mapped 37 species over different ecozones using Landsat and, specifically for phenology data, Sentinel-2 time series. These studies all demonstrate the effective use of multispectral satellite time series for large-scale tree species classification, though the use of hyperspectral data across wide ecological gradients remains unexplored.

Hyperspectral remote sensing data have the potential to improve the mapping of tree species due to their finer spectral resolution (Dalponte et al., 2012; Rogers et al., 2024; Vangi et al., 2021). For example, Vangi et al. (2021) used PRISMA data to discriminate forest types in two 900 km² study areas in Italy, achieving better spectral separability compared to S2 data. They demonstrated that hyperspectral data improved separability by 84%-120% for differentiating two coniferous and three broadleaf forest types. Rogers et al. (2024) used PRISMA to classify five forest type classes, across four study sites of about 900 km² each in the North American coastal plain, and improved the accuracy of the original reflectance data through a mixture residual spectral preprocessing transformation. Vanguri et al. (2024) combined EnMAP and S2 data to classify nine forest tree species in Poland's *Kampinos* National Park (≈385 km), finding that the combined dataset improved classification accuracy over using either source alone. Caputi et al. (2025) used PRISMA and S2 in two 900 Km² areas in Italy to classify four and five forest types, respectively, and found that PRISMA data outperformed S2, especially when processed with principal component analysis (PCA). Although improvements were more evident in homogeneous forests, PRISMA data performed better despite its lower spatial resolution, even in the mixed forests of the Mediterranean environment. Spaceborne imaging spectroscopy has therefore allowed for more accurate species identification by offering finer spectral resolution. However, most existing studies remain focused on local areas with narrow ecological gradients, also due to limitations in acquisition frequency and coverage (Shaik et al., 2023).

Large area studies are currently constrained by the limited availability of hyperspectral data, but this is expected to change in the near future. To date, hyperspectral missions are pathfinders or research-focused (EnMAP, PRISMA, HISUI), designed for targeted acquisitions rather than continuous mapping. For 2028, the European Space Agency (ESA) has planned to launch the CHIME (Copernicus Hyperspectral Imaging Mission for the Environment) mission (Nieke et al., 2023). CHIME, will carry a unique visible to shortwave infrared spectrometer to provide routine hyperspectral observations globally. NASA had planned a comparable mission for the end of this decade, called Surface Biology and Geology (SBG) mission (NASA, 2019), but the exact specifications of this mission are currently unclear. To better understand how future operational hyperspectral missions can contribute to large area mapping of forest attributes such as tree species, more regional studies that utilize hyperspectral data over large areas are required. One way to achieve that is by leveraging data from the PRISMA (PRecursore IperSpettrale della Missione Applicativa) mission (Cogliati et al., 2021) operated by the Italian Space Agency (ASI). PRISMA is considered a precursor mission designed to assess the potential of future long-term hyperspectral missions for monitoring applications. PRISMA hyperspectral imagery consists of

240 bands with a bandwidth of 12 nm or less in two spectral intervals ranging from 400-1010 nm (VNIR) and 920-2505 nm (SWIR). The hyperspectral data are collected with a Ground Sampling Distance (GSD) of 30 m and a swath width of 30 km at nadir (Guarini et al., 2018). In addition to upcoming operational hyperspectral missions, multispectral instruments are evolving towards superspectral missions, i.e., platforms with enhanced spectral resolution and additional bands to improve the monitoring of vegetation, water, and soils. For example, NASA had designed Landsat Next (Survey, 2024), which was originally planned to follow Landsat 9, to not only improve spatial resolution and revisit time but also to spectral resolution, adding more narrow bands in the visible, near-infrared, and shortwave-infrared region. Similarly, the Sentinel-2 Next Generation is expected to deliver enhanced global measurements after the Sentinel-2 mission in 2035. Meanwhile, hyperspectral precursor such as PRISMA offer opportunities not only to demonstrate the capabilities of future hyperspectral missions but also to evaluate how upcoming superspectral missions may improve applications such as tree species classification.

The objective of this study was to test how well predictive tree species models based on hyperspectral satellite data (PRISMA) generalize across a large environmental gradient in Italy. We address this objective by selecting PRISMA data from six representative study sites in Italy, where dominant tree species include broadleaves, such as Beech, Oak and Hornbeam, as well as evergreen Oak, and conifers such as Mediterranean pine, Fir and Norway spruce (Gasparini et al., 2022). The second objective was to compare the accuracy of hyperspectral models to the accuracy of multispectral models using state-of-the-art methods based on Sentinel-2 time series and prospective superspectral satellite missions such as Landsat Next (LSN). The specific research questions addressed in this study are:

- How do site-specific tree species classification models compare to a generalized classification model?
- How do tree species classification models from single PRISMA acquisitions compare to classification models based on a Sentinel-2 time series and single Sentinel-2 acquisitions?
- How do tree species classification models from single PRISMA acquisitions compare to classification models from next generation super-resolution sensors like Landsat Next?

5.2. Materials and Methods

5.2.1. Study Area

The Italian peninsula covers an area of 302,073 km², and based on its orographic characteristics can be divided into hills (41.6 %), mountains (35.2 %), and flat areas (23.2 %) (ISTAT, 2024). The Italian forests are mainly composed of temperate oaks, Mediterranean oaks, and beech forests (along with the mixed class "other deciduous broadleaf trees") (Gasparini et al., 2022). According to the NFI statistics for tall trees forests (INFC, 2015) these classes, each covering more than 1 million hectares, account for approximately 37% of the total forest cover. Other major tree species, each covering more than half a million hectares, include Hornbeam and Hop hornbeam, Chestnut, Holm oak, and Norway spruce. The minor forest categories, covering less than 250,000 hectares each, include Fir, Scots pine and mountain pine, Cork oak, Black pine, Hygrophilous forest, and Mediterranean pines. Collectively, these classes account for 15% of the national forest cover.

The Italian territory can be grouped into ecoregions based on homogeneous ecological characteristics and the interaction of natural communities and species with the physical characteristics of the environment (Blasi et al., 2010). The Italian Ecoregions are organized in four hierarchical levels: 2 Divisions (Temperate and Mediterranean), 7 Provinces, 12 Sections and 33 Subsections (ISTAT, 2023). To capture a wide ecological gradient, we selected six test sites from the temperate and Mediterranean ecoregions distributed across the Alpine, Apennine, and Tyrrhenian provinces (Figure 34). The information about the ecoregion subsection to which each site belongs were obtained from the work of Blasi et al. (2018, 2014, 2010). The ecoregion subsections ranging from Temperate semi-continental to Mediterranean oceanic climate and cover gradients from high elevation in mountain regions (2200 m a.s.l.) to sea level elevation with flat terrain on the coast, from moist areas (2550 mm per year) to dry areas (650 mm per year), from areas with colder temperatures (-8 °C in winter) to warmer areas (> 30°C in summer). Since tree species diversity as well as the availability of reference data varied geographically, 3 sites cover a single PRISMA tile (30 km^2 x 30 km^2) and 3 sites cover two PRISMA tiles (30 km^2 x 60 km^2). The following study areas were selected for this study:

1. *Central-Eastern Alps* (CEAL) belongs to the Pre-Alps subsection ecoregion (1A2a), with temperate semi-continental climate (annual precipitations 800-2500 mm, annual average temperature range 2/14°C, min -7.6/1.3°C January, max 13.8/35.2°C July). The ecoregion is dominated by coniferous forests, mainly spruce and fir, and deciduous forests, mainly beech and hornbeam. This is the northernmost study area, between the Trentino-Alto Adige and Veneto regions and is characterized by mountainous areas bordering the *Adige* River valley with an elevation in forest areas ranging from 64 to 2200 m a.s.l. (mean 922; std dev 419).
2. *Central Apennines* (CAP) is part of the Umbria and Marche ecoregion subsection (1C2a), which has a temperate semi-continental climate (annual precipitation 700-2100 mm, average annual temperature range of 6/15°C, min -3.8/3.1°C January, max 18.5/30.9°C August) and is dominated by oaks, beech, and hornbeam. This site lies on the border of the Umbria and Lazio

regions. The elevation in forest areas ranges from 16 to 1885 m .a.s.l. (mean 844; std dev 321), is mainly characterized by mountainous regions surrounding the *Terminillo* peak.

3. *Castel Porziano* (CP) lies at the Tyrrhenian Sea coast and belongs to the Roman area subsection of the ecoregion (2B1c), which has a mediterranean oceanic climate (annual precipitation of 650–1,100 mm and an average annual temperature range of 14/17°C, min 3.1/6.7°C January, max 27.7/29.8°C August). It is mostly flat with an elevation ranging from -3 to 138 m a.s.l. (mean 48; std dev 28). Most of the landscape is agricultural, and the forested areas largely correspond to the Castel Porziano presidential reserve, characterized by Mediterranean shrubs, oak forests, and pine forests.
4. *Matese (MAT)* belongs to the Campania Appennines subsection of the ecoregion (1C3a), which has a temperate oceanic/semi-continental climate on relief and transitional on hills and valleys (annual precipitation of 700-2550 mm, average annual temperature of 8/15°C, min -1.9/3.6°C January, max 21.1/32.9°C August). It is a predominantly mountainous area with an altitude ranging from 44 to 1903 m a.s.l. (mean 736; std dev 334), crossed by the *Volturno* River valley. This site lies on the border between the Campania and Molise regions and includes the protected area of *Matese* National Park, which is mainly characterized by beech, oaks, and hornbeam forests.
5. *Southern Apennines* (SAP) lies in the ecoregion of the Lucania Apennine subsection (1C3b), which has a temperate and transitional oceanic climate (annual precipitation 650-1800 mm, average annual temperature range of 11/15°C, min 0/3.2°C February, max 25.2/30.9°C August) and is primarily dominated by oaks and beech forest. The elevation ranges from 42 to 1900 m a.s.l. (mean 899; std dev 285) and is mainly occupied by the mountainous territories of the *Lucano Apennine, Val d'Agri,*

Lagonegrese, and Cilento and Vallo di Diano National Park, on the border between Campania and Basilicata regions.

6. *Serre* (SER) is part of the Calabria subsection (2B2c), which has a temperate oceanic climate at higher altitudes (annual precipitation 500-1800 mm, average annual temperature 9/18°C, min -2.8/8.1°C February, max 19.7/32.5°C August) and is predominantly dominated by deciduous oak, beech, pine and fir forests. The topography of this site is characterized by mountainous areas bordered by the Tyrrhenian and Ionian coasts, with elevations ranging from 7 to 1428 m a.s.l. (mean 737; std dev 310). It is the southernmost study area and corresponds to the *Serre* Park in the Calabria region.

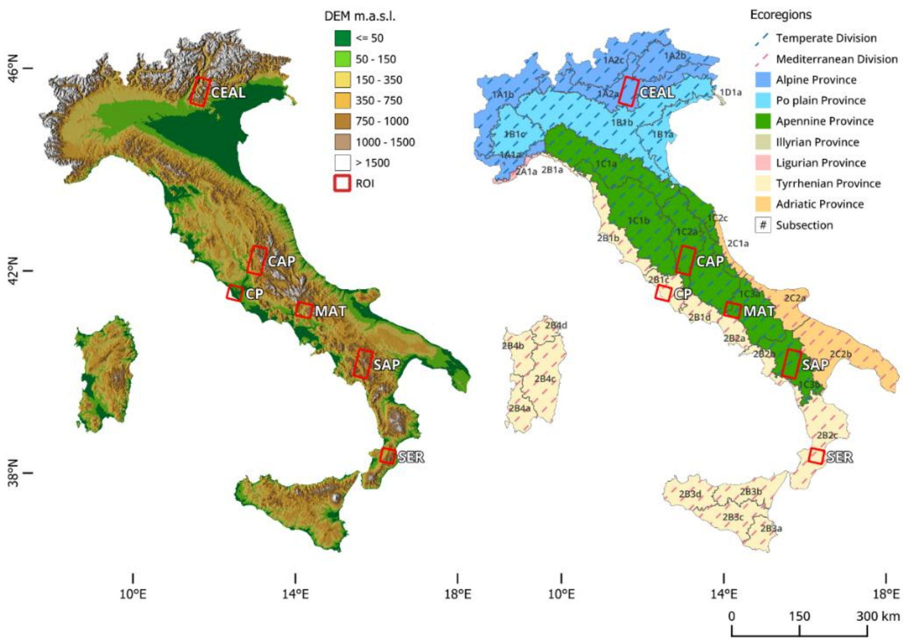

Figure 34: Orographic characteristics of Italy using Copernicus Digital Elevation Model (European Space Agency, 2021) on the left, ecoregion subsection division by ISTAT based on (Blasi et al., 2010) on the right. The ROIs are outlined by the red rectangles.

5.2.2. Remote Sensing data

Following the aim of our study we use different remote sensing data: HS satellite data from PRISMA (ASI, 2019), multispectral satellite data from Copernicus S2 (ESA, 2015), and a synthetic reproduction using PRISMA bands of what the future Landsat Next (Survey, 2024) should be.

Prisma data

In this study we used a total of 9 PRISMA HS level L2D cubes (Table 22) downloaded from the ASI portal (www.prisma.asi.it). The PRISMA images were acquired during the growing season in 2023 and selected so that they had the lowest cloud cover percentage. Level L2D PRISMA data are atmospherically corrected and orthorectified (Caporusso et al., 2020; Loizzo et al., 2018). However, the geolocation accuracy of PRISMA can still vary up to 200 m within the same scene and between different acquisitions (De Luca et al., 2024). We used AROSICS (Automated and Robust Open-Source Image Co-Registration Software) (Scheffler et al., 2017) to improve the geometric accuracy of PRISMA HS cubes using S2 data as reference. Specifically, we used AROSICS' local co-registration approach, which applies phase correlation in a moving-window manner to a regular grid of tie points and estimates X/Y translations for each point within the overlapping area of the input images. In our implementation, we used a window size of 256 x 256 pixels and a grid resolution of 30 m x 30 m. To identify matching tie points, we used the S2 NIR band 8a (cubic-convolution resampled to 30 m) and the PRISMA NIR band 47 (~ 800 nm). The derived shift information was then used to resample the PRISMA cube via cubic convolution, thereby correcting for geometric misalignments. Finally, we removed noisy bands within the following ranges: from band 104 (1361 nm) to band 112 (1449 nm), and from band 147 (1803 nm) to band 163 (1949 nm) (Alicandro et al., 2022). These bands contain values equal to zero for the majority of pixels, due to the low signal-to-noise ratio and the absorption of solar energy by water vapor (De Luca et al., 2024; Flynn et al., 2020).

Sentinel-2 data

In this study, we used all available Sentinel-2 scenes acquired between 1 January 2023 and 31 December 2023 with an estimated cloud cover of less than 75%. The images were downloaded at processing Level-1C from the Copernicus Open Access Hub. Image pre-processing and analyses were conducted using the Framework for Operational Radiometric Correction for Environmental Monitoring (FORCE) (Frantz, 2019). Pre-processing included geometric correction following Rufin et al. (2020), cloud and cloud shadow detection, atmospheric correction to surface reflectance, and retrieval of nadir BRDF-adjusted reflectance using a global set of kernel parameters derived from the Moderate Resolution Imaging Spectroradiometer (Frantz et al., 2018). We used bands 2 (blue), 3 (green), 4 (red), 5–7 (red edge), 8a (near-infrared), and 11–12 (shortwave-infrared). Finally, all bands were resampled to 30 m using cubic convolution to match the resolution of the PRISMA data.

We created two different Sentinel-2 datasets as predictors for the tree species classification: 1) single Sentinel-2 images close to the acquisition date of the PRISMA data (Table 22), and 2) Sentinel-2 time series. To develop Sentinel-2 time series suitable as input for tree species classification, we followed the approach by Hemmerling et al. (2021) and Blickensdörfer et al. (2024), who used Sentinel-2 time series to map tree species in Germany. Their approach applies a weighted ensemble of radial basis convolution filters (RBF) with varying kernel widths (σ) to each pixel to produce continuous, gap-free spectral time series. We applied the RBF ensemble to each band to generate time series with a regular temporal spacing every 30 days between 1

January 2023 and 31 December 2023. In total, this resulted in 108 features (12 time-steps times 9 bands).

Table 22: Acquisition dates of the PRISMA and Sentinel-2 data at each site.

Site	PRISMA	S2 single	S2 time series
CEAL	2023/08/13	2023/08/13	2023/01/01 - 2023/12/31
CAP	2023/07/20	2023/07/19	2023/01/01 - 2023/12/31
CP	2023/08/24	2023/08/23	2023/01/01 - 2023/12/31
MAT	2023/09/27	2023/09/27	2023/01/01 - 2023/12/31
SAP	2023/07/14	2023/07/16	2023/01/01 - 2023/12/31
SER	2023/07/25	2023/07/28	2023/01/01 - 2023/12/31

Simulated Landsat Next data

In this study, we simulated Landsat Next images using the PRISMA HS bands. Landsat Next features 18 reflectance bands ranging from 402 to 2211 nm (excluding the thermal bands, violet, water vapor and cirrus bands). We used a uniform "boxcar" relative spectral response for resampling based on the Full Width at Half Maximum specifications that had previously been provided by the USGS. A boxcar function represents a reasonable simplification of filter-based multispectral instrument relative spectral response (Dennison et al., 2023). Using the PRISMA bands and the EnMAP box Qgis plugin (Jakimow et al., 2023) we simulated a Landsat Next image for each site.

5.2.3. Reference data

To train and validate the classification models, we compiled a reference dataset from different field inventories: 1) the Italian national forest inventory (NFI), 2) an open georeferenced dataset provided by Gasparini et al. (2025), 3) local forest inventory derived from forest management plans, and 4) data from our own field surveys. The forest classification system by the NFI served as a reference for the entire dataset, i.e., all other field data were translated to the NFI classification. This was feasible as all other reference sources had the same or a higher level of detail as the NFI. The final reference classification (labels) consists of 13 classes: seven conifers, five deciduous broadleaves, and one evergreen broadleaf (Table 23). We excluded the NFI classes artificial plantation (e.g., poplar plantations, eucalyptus plantations, olive groves, etc.), shrub classes, as well as ambiguous and mixed classes like other conifers and other deciduous broadleaf. We further combined the NFI classes temperate oaks and Mediterranean oaks into deciduous oaks; and we combined holm oak and cork oak into evergreen oaks. This choice was based on the spectral similarity of these tree species (Caputi et al., 2025), as well as the relatively small sample size. Finally, we included a Cypress class, which is not part of the NFI classification, but the species was quite abundant at the MAT site (D'auria et al., 2020).

Table 23: List of the classes used in the reference dataset along with the species or group of species contained in each class, following the NFI guidelines (Gasparini et al., 2016). The table also contains the number of plots available for each class at each site.

Id	Species group	Dominant species	CEAL	CAP	CP	MAT	SAP	SER	Tot
1	Larch and stone pine	*Larix decidua,Pinus cembra*	19	0	0	0	0	0	19
2	Norway spruce	*Picea abies*	84	0	0	0	0	0	84
3	Fir	*Abies alba, Abies pectinata*	58	0	0	0	0	247	305
4	Scots pine and mountain pine	*Pinus sylvestris, Pinus uncinata*	23	0	0	0	0	0	23
5	Black pine	*Pinus nigra, Pinus laricio, Pinus leucodermis*	46	60	0	74	3	238	421
6	Mediterranean pines	*Pinus pinaster, Pinus pinea, Pinus halepensis*	0	1	232	18	0	0	251
7	Cypress	*Cupressus sempervirens*	0	0	0	78	0	0	78
8	Beech	*Fagus sylvatica*	68	16	0	286	85	402	857

9	Deciduous oaks	Temperate oaks: *Quercus petraea, Quercus pubescens, Quercus robur;* Mediterranean oaks: *Quercus cerris, Quercus frainetto, Quercus trojana, Quercus ithaburensis*	3	119	487	41	87	0	737
10	Chestnut	*Castanea sativa*	2	2	0	2	50	296	352
11	Hornbeam and Hophornbeam	*Ostrya carpinifolia, Fraxinus ornus, Carpinus orientalis, Carpinus betulus*	58	49	1	36	5	0	149
12	Hygrophilous species	*Populus sp., Salix sp., Alnus sp., Fraxinus sp., Ulmus sp., Platanus sp.*	0	0	0	16	0	95	111
13	Evergreen oaks	*Quercus ilex, Quercus suber*	0	54	242	21	1	112	430
Tot			361	301	962	572	231	1390	3817

The final harmonized reference dataset consists of 30 m x 30 m reference pixels, each labeled with the dominant tree species present at the corresponding inventory plot. Only plots with pure or clearly dominant species or species groups were included. To account for differences in acquisition years between field and remote sensing data, all selected plots were manually checked for disturbances and obvious misclassifications (e.g., conifers labeled as deciduous or vice versa) using high-resolution satellite imagery in Google Earth. Additionally, to reduce spatial autocorrelation, a minimum distance of 50 m was enforced between plots belonging to the same class. A more detailed description of the individual data sources follows:

- *National Forest Inventory*: the national forest inventory was conducted in 2015 (INFC, 2015). The national inventory collects data at a systematic grid (1 km x 1 km) using circular plots with a radius of 25 m (Gasparini et al., 2020, 2016). Each field plot is assigned to one of 23 NFI classes based on the dominant species or group of species. Dominant species have a canopy cover greater than 50% (Pignatti Sandro, 2003). To estimate the canopy cover of the dominant species, the NFI surveyor takes 25 ocular canopy measurements within 2000 m^2 of the plot along two orthogonal transects (N-S and E-O) (Gasparini et al., 2016). In total, we selected 247 NFI plots of 15 different tree species groups.

- *Open georeferenced field dataset*: The open, georeferenced field data on forest categories and species was provided by Gasparini et al. (2025) to support the use of remote sensing data in forest studies. In total, 934 circular plots of radius 15 m were collected in 2023 and 2024 using the same classes and sampling method as the NFI, 821 of which intersected with our study sites (CEAL: 265, CAP: 330, SAP: 226) covering 11 tree species groups. We excluded 40 mixed forest plots for which coniferous or deciduous crown cover was lower than 75% (Gasparini et al., 2025), respectively. We made an exception for the Scots pine and mountain pine class, due to the limited number of pure species plots for this class.
- *Local inventory data*: Local inventory data were provided by the Italian province of Trento (CEAL), the Mediterranean Ecosystem Observatory Office of Castel Porziano (CP), and for four municipalities of the Matese Park (MAT). The data at CEAL and CP were polygons delineating homogenous stand boundaries. We filtered all polygons that conformed to the NFI classification and randomly selected 30 m x 30 m pixels within these polygons, ensuring a minimum distance of 50 m between selected pixels. The MAT data consisted of a systematic sample of 20 m x 20 m plots surveyed between 2017 and 2020, as part of the preparation of forest management plans. For each plot, species and diameter information was available for all trees. Here, we selected all plots for which the dominant species group made up 80% and higher of the plot basal area. In total, we selected 108 plots of 7 species

groups at CEAL, 1091 plots of 6 species groups at CP, and 260 plots at MAT.

- *Field surveys data*: we carried out some field surveys at the SER site in March 2024, and at the MAT site in November 2024. Field information was collected using two smartphone applications EyeLand (EyeLand App, 2024) and Qfield (QField App, 2024) and the Geomax Zenith35 Global Navigation Satellite System (GNSS) instrument. EyeLand is an experimental app developed to facilitate field data collection (EyeLand App, 2024). Data were collected either for 30 m x 30 m plots or for larger, homogenous polygons. For each plot and polygon, we recorded the dominant species and species association and then assigned the corresponding NFI class following the NFI field survey guidelines (Gasparini et al., 2016). From the polygon data, we later extracted a random sample of 30 m x 30 m pixels, ensuring a minimum distance of 50 m, consistent with the procedure used for other datasets. For the MAT site, we used 654 plots and for the SER site we used 1405 plots.

5.2.4. Classification models

To address our research questions, we trained several random forest classification models using the species group labels as response and the satellite data as predictors. Random forest (Breiman, 2001) can handle high dimensional datasets, and it is robust against overfitting (Belgiu and Drăguţ, 2016; Lou et al., 2024). We used the Random Forest package in R (Liaw and Wiener, 2002) and the default parameters (mtry = sqrt(p), where p is the number of predictor variables), but we set the number of trees to 1000 (Blickensdörfer et al., 2024). Finaly, we applied a mask including only forest areas according to the Forest Map of Italy (CREA - MASAF, 2020).

For research question 1, we analyzed how well tree species classification models based on PRISMA data generalize across multiple sites. To address this question, we built and compared two types of models: 1) a generalized model combining reference and PRISMA data from all study areas, and 2) site-specific models trained separately for each study site.

To address research question 2 and 3, we compared classification models trained with PRISMA data against classification models trained with single-date Sentinel-2 data, Sentinel-2 time series, and Landsat Next. For this comparison, we used generalized models, i.e., a single model across all sites for each sensor.

In general, the classification accuracy should improve as the number of spectral bands increase, due to the dense spectral information captured in narrow bands that enhance the ability to distinguish specific characteristics (Dalponte et al., 2012; Lv and Wang, 2020; Rasti et al., 2020; Signoroni et al., 2019). However, the high dimensionality of HS data requires a large amount of training data and can affect the accuracy of the results (Alonso et al., 2011; Hughes, 1968). We used a band selection approach, since the physical interpretation of the information is not altered by the choice of a subset of bands compared to feature extraction techniques (Sawant and Prabukumar, 2020). We applied a recursive feature elimination (RFE) method using the caret package (Kuhn, 2008) in R (version 4.4.3) (R Core Team, 2021) to reduce the number of features in the PRISMA data and Sentinel-2 time series. Recursive feature elimination involves iteratively training Random Forest, ranking features by importance, and removing the least important ones until the desired number of features is reached. In this study, we used a step size of 10 features with five-fold cross-validation repeated five times in each iteration. The optimal number of features was selected based on the lowest RMSE, which resulted in 72 PRISMA bands and 108 Sentinel-2 time series features. The differences in prediction error between the full and reduced feature sets were marginal. However, we proceeded with the reduced feature set for the classification.

To validate the model results we use the out-of-bag (OOB) cross-validation method (Blickensdörfer et al., 2024; Hemmerling et al., 2021). The OOB method allows the entire reference data to be used, preventing the division into training and testing from further reducing the amount of data for underrepresented classes. Furthermore, cross-validation methods are able to estimate the standard error with greater reliability than using a static validation dataset (Breiman, 2001). Accuracy metrics were calculated from the error matrices generated using the reference dataset and OOB predictions to evaluate the performance of the classification models and the predictive accuracy. Specifically, for each classification we calculate the overall accuracy (OA), user's accuracy (UA), producer's accuracy (PA), and F-score (Congalton, 2001). The OA of site-specific models was calculated by aggregating the results obtained at individual sites into a single error matrix with all classes used.

5.3. Results

Comparison between generalized and site-specific models

The PRISMA model generalized well across the six sites. The difference in overall accuracy between the generalized model (OA = 79.41% ± 0.65%) and the site-specific models (80.67 ± 0.63%) were marginal. For most classes, the site-specific models achieved only slightly higher accuracies, up to 2 pp (percentage points) (Figure 35). The most significant differences in accuracy were found for some but not all species endemic to single sites. For example, Scots and mountain pine as well as Norway spruce only occurred at the Alpine site (CEAL). Their accuracy improved with the site-specific model by 11 pp and 3 pp, respectively. Interestingly, the accuracy of Larch and stone pine (also endemic to CEAL) only improves by 2 pp, despite the small sample size like Scots and mountain pine. Hygrophilous species occurred at two sites but predominantly at Serre. The accuracy of

Hygrophilous species improved with site-specific models by 5 pp (± 3 pp). Also, the accuracy of the Evergreen Oaks improved with site-specific by 3 pp despite its presence at four sites.

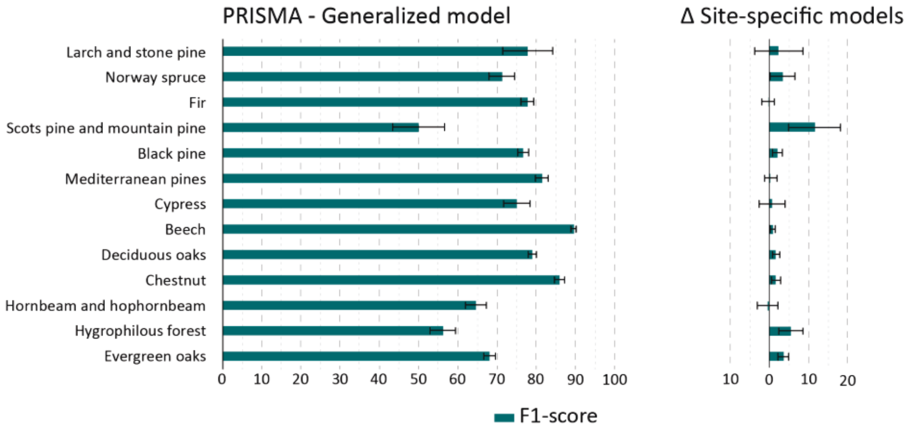

Figure 35: F1-scores (%) for each tree species group using the generalized model with PRISMA HS data and the difference in F1-scores (Δ) between generalized and site-specific models. Negative values indicate a lower accuracy, and positive values indicate a higher accuracy of the site-specific models compared to the generalized model. Error bars show the standard error.

The F1-scores of each class obtained with the site-specific models were generally higher compared to the generalized model but not for all the sites (Figure 36). The generalized model improved the results for some classes that occur at multiple sites, compared to the F1 obtained at some of these sites with site-specific models. While the greatest differences for the species that occurs at one or two sites can only be seen for the *Scots and mountain pine* and *Hygrophilous species* classes. For the classes occurring at multiple sites, we found bigger difference in F1 depending on the site. Some of these classes like *Beech* or *Deciduous oaks* have almost similar F1 values at all sites except one (CAP and MAT, respectively), where both the reference data and the accuracies were very lower. The accuracies of some other classes such as *Black pine*, *Hornbeam and Hophornbeam* and *Evergreen oaks* vary greatly across the sites, with the lowest F1-score at the site where they have the fewest reference plots: *Black pine* at CEAL site and *Hornbeam and Hophornbeam* and *Evergreen oaks* at MAT site. However, an increase in the number of plots does not necessarily indicate higher accuracy, as evidenced by the F1-values of *Black pine* and *Evergreen oaks* at the CAP site.

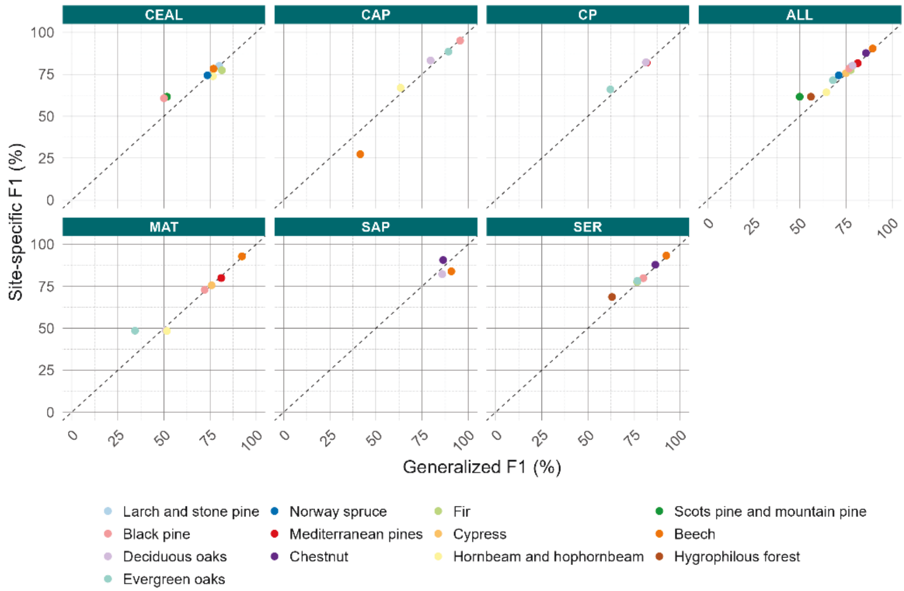

Figure 36: The graph shows the F1-scores (%) obtained for each class using PRISMA data, in each of the study sites, with the generalized model and with the site-specific models.

The error matrix and accuracy metrics obtained using the generalized model (Table 24) report the highest F1-scores obtained for *Beech* class (89.51 ± 0.72%) and *Chestnut* class (85.95 ± 1.27). *Deciduous oaks* and *Evergreen oaks*, despite were frequently confused with each other (11% of *Deciduous oaks* plots classified as *Evergreen oaks* and 14% of *Evergreen oaks* plots classified as *Deciduous oaks*), achieved an F1 of 78.89 ± 1.00% and 68.02 ± 1.47%, respectively. Some classes such as *Hornbeam and Hophornbeam* and *Hygrophilous species* classes were frequently misclassified with *Beech* and *Deciduous oaks* and *Beech* and *Chestnut*, respectively, which corresponds to widely represented classes in the dataset. Also, *Scots and mountain pines* had one of the higher misclassification errors in percentage, as it was often confused with *Norway spruce*. *Beech*, *Deciduous oaks*, *Chestnut* and *Norway spruce* are indeed the most overestimated classes. While significant underestimation occurs for *Scots and mountain pines*, *Hygrophilous species*, *Hornbeam and Hophornbeam* and *Evergreen oaks*. *Larch and stone pine* and *Cypress* occurring only at one site (CEAL and MAT) shifted from moderate overestimation to moderate underestimation using the generalized model.

Table 24: Error Matrix of the generalized model using PRISMA.

	Reference class (sample counts)													Total	
Map class	1	2	3	4	5	6	7	8	9	10	11	12	13	Map	Ref
Larch and stone pine ǀ 1	14	-	-	-	1	-	-	-	1	-	1	-	-	17	19
Norway spruce ǀ 2	1	63	7	10	5	-	1	2	1	-	2	1	-	93	84
Fir ǀ 3	-	6	227	-	28	-	-	7	-	5	-	3	3	279	305
Scots pine and mountain pine ǀ 4	-	-	-	8	-	-	-	-	-	-	-	1	-	9	23
Black pine ǀ 5	3	10	36	3	325	1	11	8	6	5	3	7	9	427	421
Mediterranean pines ǀ 6	-	-	-	-	3	204	1	-	25	-	-	-	17	250	251
Cypress ǀ 7	-	-	-	1	11	-	57	-	2	-	1	1	1	74	78
Beech ǀ 8	-	4	14	1	17	-	-	806	26	11	31	22	12	944	857
Deciduous oaks ǀ 9	-	1	2	-	11	29	6	18	613	5	24	6	102	817	737
Chestnut ǀ 10	-	-	13	-	6	-	-	8	5	315	2	18	14	381	352
Hornbeam and hophornbeam ǀ 11	-	-	-	-	6	1	2	3	11	1	83	-	1	108	149
Hygrophilous species ǀ 12	-	-	2	-	-	-	-	3	1	3	-	48	3	60	111
Evergreen oaks ǀ 13	1	-	4	-	8	16	-	2	46	7	2	4	268	358	430

	Accuracy		
Map class	**Producer's**	**User's**	**F1**
Larch and stone pine ǀ 1	73.68 ± 8.91	82.35 ± 9.25	77.78 ± 6.45
Norway spruce ǀ 2	75.00 ± 4.27	67.74 ± 4.85	71.19 ± 3.30
Fir ǀ 3	74.43 ± 2.16	81.36 ± 2.33	77.74 ± 1.59
Scots pine and mountain pine ǀ 4	34.78 ± 6.24	88.89 ± 10.48	50.00 ± 6.65
Black pine ǀ 5	77.20 ± 1.81	76.11 ± 2.06	76.65 ± 1.37
Mediterranean pines ǀ 6	81.27 ± 2.23	81.60 ± 2.45	81.44 ± 1.65
Cypress ǀ 7	73.08 ± 4.43	77.03 ± 4.89	75.00 ± 3.29
Beech ǀ 8	94.05 ± 0.78	85.38 ± 1.15	89.51 ± 0.72
Deciduous oaks ǀ 9	83.18 ± 1.23	75.03 ± 1.51	78.89 ± 1.00
Chestnut ǀ 10	89.49 ± 1.55	82.68 ± 1.94	85.95 ± 1.27
Hornbeam and hophornbeam ǀ 11	55.70 ± 3.26	76.85 ± 4.06	64.59 ± 2.62
Hygrophilous species ǀ 12	43.24 ± 3.44	80.00 ± 5.16	56.14 ± 3.16
Evergreen oaks ǀ 13	62.33 ± 1.90	74.86 ± 2.29	68.02 ± 1.47
	Overall accuracy = 79.41 ± 0.65		

A visual comparison of the classification maps obtained using PRISMA with the generalized model and the site-specific models indicates a high degree of agreement in certain areas, while revealing significant discrepancies in forest cover predictions in other areas (Figure 37). The models' predictions differ most clearly at the CEAL and CAP sites. At CEAL site most of the pixels that the generalized model classified as *Beech* were assigned to *Hornbeam and Hophornbeam* or *Fir* by the model trained exclusively with reference data from that specific site. A similar pattern emerges at CAP site where pixels classified as *Beech* by the generalized model were classified with the site-specific model as *Deciduous oaks*. Conversely, at MAT study area the site-specific model classified as *Beech* some pixels that the generalized model assigned to the *Norway spruce* and *Deciduous oaks*. In the SAP study area, the predictions of the two models were very similar, but in the case of the generalized model, there was a higher presence of pixels assigned to the *Chestnut* and some pixels assigned to *Evergreen oaks* which was absent with the site-specific model. Very similar predictions were also observed at CP and at SER sites. The only notable difference was the higher presence of *Black pine* with the generalized model at SER site, whereas the site-specific model classified them mostly as *Evergreen oaks* or *Hygrophilous species*.

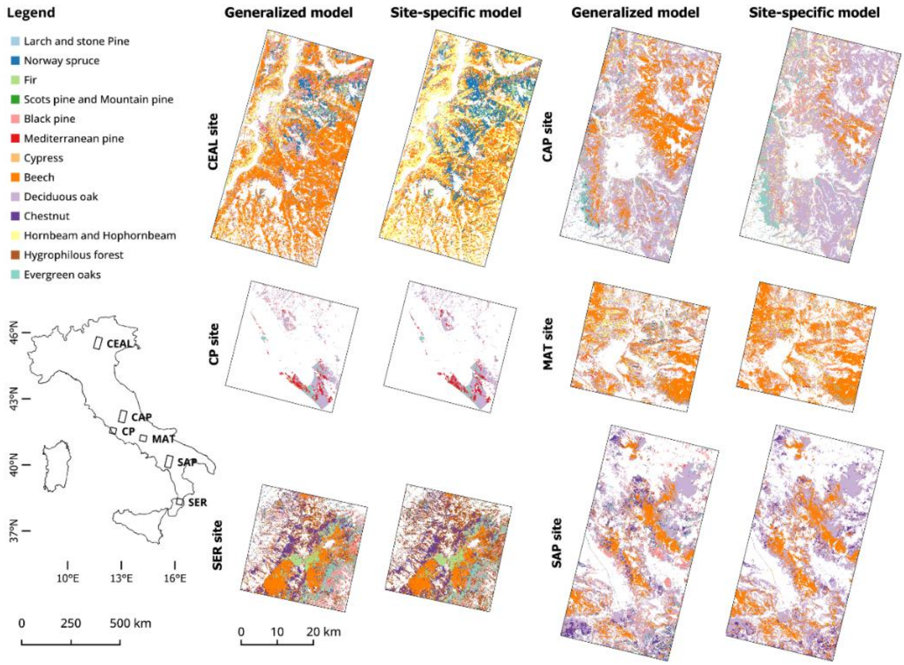

Figure 37: Comparison of the classification maps at each site obtained with generalized and site-specific models using PRISMA.

Comparison between PRISMA and Sentinel-2

In this study, in addition to testing the use of the recent PRISMA data, we used Sentinel-2 as this is one of the satellites widely used for large-scale mapping of tree species at the moment. The S2 time series achieved with the generalized model an OA (82.24 ± 0.62%) slightly better than PRISMA (79.41 ± 0.65). At the same time, using the single S2 acquisition reduced the OA (75.39 ± 0.69) compared to PRISMA.

The F1 obtained using PRISMA generally shows that a single HS acquisition yields better results than individual S2, while S2 TSI allow for higher accuracy in predictions (Figure 38). The F1-scores obtained with S2 were generally lower than PRISMA for the majority of the classes. Bigger differences were found for *Larch and stone pine* (Δ -0.38), *Scots pine and mountain pine* (Δ -0.21), *Hornbeam and Hop Hornbeam* (Δ -0.19), *Hygrophilous species* (Δ -0.14) and *Cypress* (Δ -0.12). The only classes that slightly improved using S2 were *Norway spruce* (Δ +0.03) and *Mediterranean pine* (Δ +0.02).

Conversely, the predictions using S2 time series were slightly better compared to PRISMA. The higher differences occur for *Hygrophilous species* (Δ +0.07), *Evergreen oaks* (Δ +0.07), *Fir* (Δ +0.06), *Cypress* (Δ +0.05), *Chestnut* (Δ +0.05), and *Larch and stone pine* (Δ +0.04). The other classes did not have significantly higher F1 when using S2 TSI compared to PRISMA, averaging Δ +0.02. Only *Scots pine and mountain pine* (Δ -0.14) and *Hornbeam and Hop Hornbeam* (Δ -0.09) were improved using PRISMA.

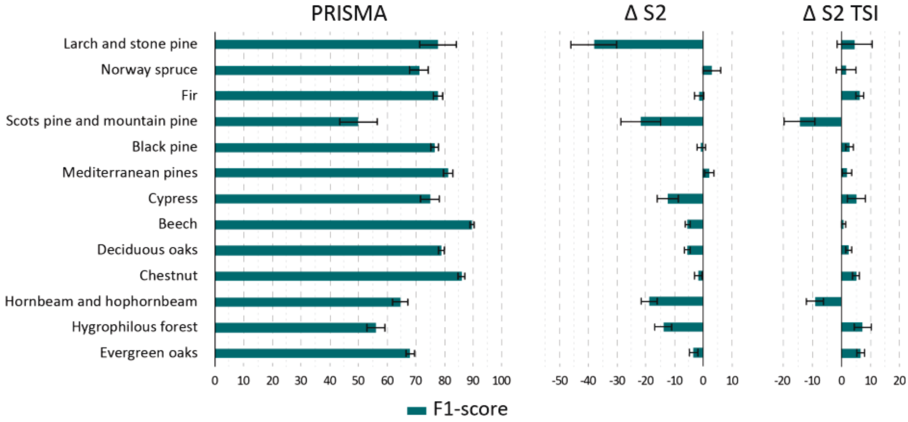

Figure 38: F1-scores (%) obtained using the generalized model with PRISMA and differences with S2 and S2 TSI negative Δ indicate worse performance, while positive Δ indicate better performance than PRISMA.

A visual comparison of the classification maps shows broad agreement between PRISMA, S2 and S2 TSI predictions, though certain differences emerge. At some sites, PRISMA tends to assign more pixels to specific tree classes such as Beech, Norway spruce, or Chestnut, while Sentinel data more often classifies those same areas as Hornbeam and Hophornbeam or Oak classes. For example, PRISMA frequently predicts higher proportions of Beech and Norway spruce, with fewer Hornbeam and Hophornbeam, compared to Sentinel data (CEAL site). In other cases, pixels labeled as Beech in PRISMA maps are reclassified when using Sentinel imagery as Deciduous oaks or Hornbeam and Hophornbeam (CAP site) or as Deciduous oaks and Evergreen oaks (MAT site). In other cases, PRISMA and Sentinel agree closely, with only minor shifts such as a higher presence of Chestnut (SAP site) or Black pine (SER site) in PRISMA predictions. Overall, although little or no difference has been found between PRISMA and Sentinel maps for large parts of the studied areas, the generalized model slightly tends to amplify them.

Comparison between PRISMA and Landsat Next

In this study, we simulated the bands of Landsat Next to compare the classification of PRISMA data with future new-generation super-resolution sensors. The OA obtained using LSN (76.66 ± 0.68%) with the generalized model was lower compared to the one obtained using PRISMA (79.41 ± 0.65). Interestingly, for most of the classes, the improvement due to the HS data was minimal (Figure 39). Significant differences were only recorded for the Larch and stone pine (Δ -0.18), Hygrophilous species (Δ -0.16), Hornbeam and hophornbeam (Δ -0.08), Norway spruce (Δ -0.06), and Deciduous oaks (Δ -0.04). Considering only the classes with an F1-score greater than 70% the most significant advantages occurred only for Larch and stone pine, Norway spruce and Deciduous oaks. Comparable results between PRISMA and LSN were found for the other classes. However, except Evergreen oaks (Δ +0.01), all other classes obtained a slightly worse F1 using LSN, averaging Δ -0.02.

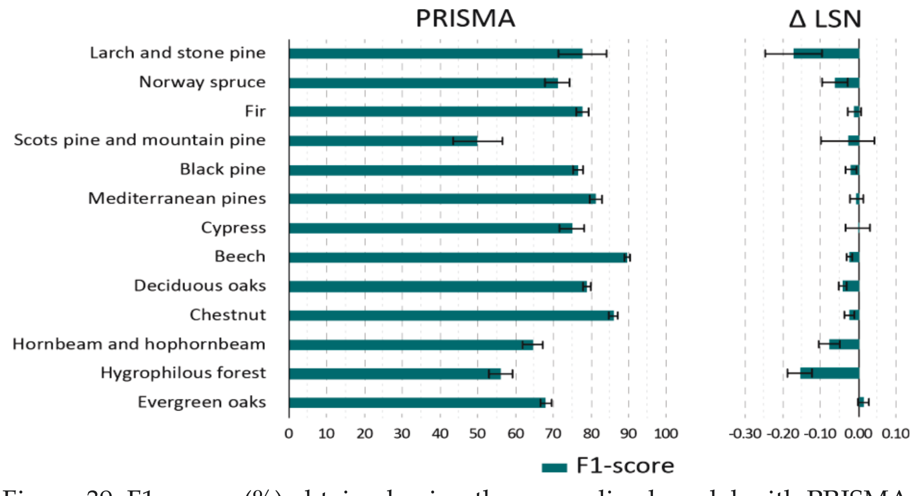

Figure 39: F1-scores (%) obtained using the generalized model with PRISMA and differences with LSN: negative Δ indicate worse performance, while positive Δ indicate better performance than PRISMA

A comparison of the classification maps derived from PRISMA and LSN with the generalized model shows only a few localized differences. At CEAL, SAP, CP, and MAT sites, classification maps obtained using PRISMA or LSN were very similar. A noteworthy difference occurs at SAP site with a greater presence of pixels assigned to the *Chestnut* when using LSN compared to PRISMA (or Sentinel) data. At SER site, differences are minimal, though LSN map shows a slightly higher presence of *Mediterranean pine* and *Evergreen oaks* compared to PRISMA.

5.4. Discussion

Models' comparison

This study explores the classification of 13 forest categories across six study sites in Italy, using two classification models. The aim was to explore how site-specific models trained separately for each site compare to a generalized model trained by combining the predictors of all the sites. The overall accuracy results show only marginal difference between the generalized model (OA = 79.41% ± 0.65%) and the site-specific models (80.67 ± 0.63%), as the majority of the classes obtained only slightly higher accuracies with the site-specific models. The concept of accuracy may depend on the user's needs and the type of application (Foody, 2002) and an increase in the precision of a thematic map, leading to a greater number of classes, often results in a reduction of the map's overall accuracy (Brivio et al., 2006). Although a direct comparison cannot be made due to differences in the data used, types and number of classes, or study area, the results obtained in this study concerning OA are consistent with previous studies on tree species classification. For example, Blickensdörfer et al. (2024) classified 11 forest species using Sentinel-1 and Sentinel-2 time series at the national level in Germany and obtained an OA equal to 87.07% when considering only pure-species stands and 75.53% when also including plots from mixed-species. Rogers et al. (2024) obtained an average balanced accuracy of 76% in classifying 21 distinct land cover types in North America, including 5 forest classes. Caputi et al. (2025) used PRISMA and S2 to classify 4 and 5 forest classes in two different areas in Italy and obtained a weighted OA of 72.74% and 87.33%, respectively. Bolyn et al. (2022) classifies 9 species in Belgium using a nested U-shaped neural network trained with forest inventory polygon and obtained an OA for major species of 73%.

From the comparison of the models three major aspects emerged. First, the classification errors for both models occur mostly because of the underrepresentation of classes within the reference dataset (which in some cases corresponds to minor species) or because of the misclassification between species which share the same genus or the same growing environment. Second, we noted that the accuracy of some classes occurring at multiple sites (i.e., *Black pine*, *Hornbeam and Hophornbeam* and *Evergreen oaks*) was improved by the generalized model compared to the site specific at the sites where the reference data for those classes were lower. For classes present at multiple sites the differences in accuracy obtained in site-specific models for those classes appear to be closely linked to the availability of predictors at each study site, as the cases of *Beech* at CAP site and *Deciduous oaks* at MAT site. Third, we found that the two models differed significantly for almost all the classes occurred or predominantly occurred at a single site, such as *Scots and mountain pine*, *Norway spruce* and *Hygrophilous species*. However, the site-specific model unexpectedly differs from the generalized for the *Evergreen oaks,* despite occurring at multiple sites, and did not improve the accuracy of *Larch and stone pine* endemic to CEAL site. Overall, the results of the generalized model are promising for mapping major tree species across wide ecological gradient. Even species with limited reference data at certain sites can benefit from using the generalized model, as noted in Marconi et al. (2022). However, all the aspects described in the previous paragraph highlight some challenges associated with multiple factors, including: (i) the availability of reference data; (ii) the inherent characteristics of species that may differ across the sites; and (iii) the capacity to encompass the characteristics of the mixed forests.

i. Remote sensing data can greatly contribute to forest mapping across a wide environmental gradient, but the availability of reference data remains a key concern. National forest inventories have proven to be an excellent solution for tree species mapping at national scale (Blickensdörfer et al., 2024; Francini et al., 2024). However, we strictly relate the surface of the sites included in this study to the coverage of PRISMA data. As a result, there were limited plots available for some classes at certain sites due to the NFI sampling grid size (Gasparini et al., 2020). The plot availability affected the F1 values for both the generalized model and the site-specifics model at some sites. Among the most widespread forest categories in Italy (Gasparini et al., 2022), higher F1-scores were obtained for *Beech* (89.51 ± 0.72), *Deciduous oaks* (78.89 ± 1.00) and *Chestnut* (85.95 ± 1.27) compared to *Norway spruce* (71.19 ± 3.30) *Hornbeam and Hophornbeam* (64.59 ± 2.62). The F1 values obtained for these classes vary significantly with site-specific models (Figure 36), yielding higher or lower values depending on the site, showing the correlation with available plots at that site. The low accuracy for minor species, such as *Scots pine and mountain pine* (50.00 ± 6.65%) may be related to the limited number of samples. However, in other cases, such as *Larch and stone pine* (77.78 ± 6.45%), the accuracy was higher despite the limited number of plots. Also, different accuracies for classes with similar sample sizes such as *Hygrophilous species* (56.14 ± 3.16 %) and *Cypress* (75.00 ± 3.29%) show that accuracy does not always depend on the amount of training data, but rather on how easily a class can be separated from others based on spectral characteristics.
ii. The inherent characteristics of tree species, which may vary across a range of geographical and climatic conditions, increase the

variability within individual classes (Blickensdörfer et al., 2024; Hemmerling et al., 2021). The site-specific models exhibit more sensitivity to such spectral variability because were trained using site-specific labeled data, which provide better descriptions of the characteristics of trees at each site. However, the results demonstrate a satisfactory level of accuracy, even using a generalized classification model applied to a broad ecological gradient. The higher differences with the site-specific models emerged for classes predominantly occurring at single site, as a consequence of both the limited number of reference data but also the site-specific spectral characteristics of those classes. If for classes endemic to a single site, such as *Scots and mountain pine* and *Norway spruce* at the CEAL site, the greater accuracy of the site-specific model would be expected. For other classes, such as *Evergreen Oaks* and *Hygrophilous species* present in multiple sites, lower accuracy seems more closely linked to the complexity of representing the spectral variations these classes exhibit along the ecological gradient.

iii. The distribution of forest species is not always homogeneous, and correctly assigning pixels to the corresponding class is more challenging in cases of mixed forest cover. In this study, we considered only pure stands as reference data; however, the sampling method used by the NFI (Pignatti Sandro, 2003) and the thresholds used in this study to define the dominant class may not ensure the exclusive occurrence of a single species within the plot. It is likely that some samples, though labeled according to the dominant species, are spectrally influenced by the presence of minor species within the plot, leading to higher classification errors. This is particularly evident for classes as *Hornbeam and Hophornbeam* and *Hygrophilous species*, which are characterized by multiple species, including different genus levels (Table 23). Plots collected in mixed forest areas composed of species with similar ecological characteristics, such as climate, altitude range, and growing environment, are likely to negatively impact the classification accuracy. Hornbeam and hophornbeam, for instance, often get misclassified as oak and beech because they share the same growing habitat (Gasparini et al., 2022). The accuracy *Evergreen oaks* class is negatively impacted by its confusion with the *Deciduous oaks* class, with which it shares a genus, but also with the *Mediterranean pine* class, with which it coexists in the Mediterranean mixed pine-oak ecosystem. Depending on the spatial resolution, the satellite data could also return reflectance data as the sum of several species rather than a single one. Indeed, the spatial resolution of 30 m could hinder the distinction between the two species in the Mediterranean scrub environment, as previously noted in (Caputi et al., 2025).

In this study, we found a high level of agreement between the generalized model and the site-specific models in some areas (CP, MAT, SAP, and SER sites). This supports the idea that the generalized model can accurately predict forest cover categories by combining reference data from different study areas. However, the classification maps of other areas (CEAL and CAP sites) show significant differences in the predictions of the two models. The most substantial differences between the two models were found for classes that were less represented in a given site, for example, Beech at CEAL and CAP sites. These results highlight the need for more representative sample data covering the entire ecological gradient and containing the spectral characteristics of species at each site.

PRISMA and Sentinel-2 comparison

The S2 time series provided the best results for all the accuracy metrics used, showing that the temporal resolution of RS data remains crucial for differentiating between various forest categories (Hemmerling et al., 2021; Zhong et al., 2024). Nevertheless, the single

HS acquisitions achieve comparable results, demonstrating that higher spectral resolution, along with greater availability of acquisitions in the future, may be the way forward to guarantee even more robust results. The most frequent classification errors in this study (Table 24) tend to occur among forest types belonging to the same *genus* (e.g. *Quercus*, *Pinus*) or the same forest macro-category (i.e. Conifers or Deciduous Broadleaf), as in (Francini et al., 2024; Hemmerling et al., 2021). HS data can distinguish species more accurately, particularly those with similar spectral characteristics (Dalponte et al., 2012).

Using HS satellite data, such as PRISMA, to identify forest types seems very promising, even with a single acquisition (Caputi et al., 2025; Delogu et al., 2024; Vangi et al., 2021). Our results indicate that the F1 obtained with PRISMA were higher than those of single S2 scenes for 10 out of 13 classes, even when combining results from multiple sites in different ecoregions. Using a composite data of twelve S2 acquisitions, one per month for a year, improved the results, although the enhancement compared to using PRISMA was greater than 0.05% for only four classes (Cypress, Fir, Black pine and Evergreen oaks).The S2 time series, which contains acquisitions outside of the deciduous vegetative periods, likely improves the ability to distinguish these classes, which include three conifers and one evergreen broadleaf.

These results confirm the findings of previous studies about the superior ability in distinguishing forest types and in general landcover classes when using HS compared to multispectral data. The improved ability to distinguish forest types, which was previously demonstrated in Vangi et al. (2021) through the analysis of the spectral separability of S2 and PRISMA data — particularly with a fourth-level CLC nomenclature (Büttner et al., 2004) — remains evident using the NFI classification level adopted in this study, which is comparable to a fifth-level CLC classification. The HS data generally performed better than the individual S2 acquisitions for most classes and slightly worse than the multi-temporal series for some classes. However, it should be noted that in this study, the HS data was used as it is, except for the feature selection that led to the use of 72 bands. Further improvements to the results could be achieved through the combination of multispectral data and techniques to enhance data quality. Vanguri et al. (2024), for example, combines EnMAP hyperspectral data with S2 data to classify tree species and shows that EnMAP alone performs better than S2 data for certain classes. In most cases, better results are achieved by combining the two datasets. Rogers et al. (2024), meanwhile, demonstrates that it is possible to improve results by applying the Mixture Residual spectral preprocessing transformation to the PRISMA data, using endmembers to consider illumination variability and absorption features.

PRISMA and Landsat Next comparison

The results obtained with the generalized model using the PRISMA data differ significantly from those obtained with the simulated LSN data for only 4 out of 13 classes. The remaining classes achieved comparable, though slightly better, results with the HS data. The most significant improvements using PRISMA were for classes with limited reference data, such as Larch, Stone Pine, Hornbeam, Hophornbeam, and Norway Spruce, and for classes characterized by a mixed growth environment with other species, such as Hygrophilous species. These results suggest that HS data can discriminate these species more effectively, even with limited reference data. Using the site-specific model, the differences between PRISMA and LSN for the Hygrophilous class decreased. This class, characterized by varying percentages of different species, appears to be more related to site-specific characteristics. However, any improvement achieved with HS data, which is more sensitive to spectral differences in the reference data and has a better ability to generalize, is reduced with the site-specific model.

Previous studies have shown that PRISMA data can be more accurate than Landsat 9 data. Kokal et al., (2022) compared PRISMA with Landsat 9 in terms of classifying 8 generic land cover categories and found that using HS data produced better classification accuracies for all the classes except for road class. There is no comparison in the literature between the PRISMA data and the Landsat data for forest tree classification, even less between PRISMA and the data that will be obtainable from the future LSN. The findings presented in this study indicate that the availability of a significant number of spectral bands in targeted intervals of the electromagnetic spectrum leads to comparable results between the HS data and the simulated LSN data. Specifically, as Vangi et al. (2021) pointed out, the spectral information acquired in the near infrared and shortwave infrared are most suitable for discriminating forest types. The higher availability of spectral bands in these intervals allows the LSN to produce better results compared to the S2 datum and results similar to those obtained with the PRISMA data.

5.5. Conclusion

In this study, we tested how well forest tree species classification models based on HS PRISMA data can generalize over a wide environmental gradient in Italy. Site-specific models are more accurate than generalized models, though the latter guarantee good results using HS data or S2 time series, particularly for tree species prevalent in Italy. This appears to be a key issue, especially in view of the future availability of Earth Observation data, including hyperspectral data, which will allow wall-to-wall classification.

In this study, we also presented a comparison of the PRISMA HS data with the state of the art represented by the S2 data and with future super-resolution satellite sensors such as LSN. This comparison demonstrated that the availability of HS data appears to be very promising for forest classification. Generally, results obtained with

PRISMA are more accurate compared to those obtained with single S2 acquisitions and comparable to those obtained with S2 time series. Future satellites, such as LSN, also appear promising because they allow for the prediction of the main forest tree species with a good degree of accuracy, despite using a smaller amount of data compared to HS data. There are still some critical issues, particularly the need for a large reference dataset that can accurately reflect the detailed forest composition. This includes the number of samples and information on individual species, in addition to the dominant species. While forest classification may benefit from the high spectral resolution, the full potential of HS data remains unexplored due to the inability to label the reference data considering the species-specific percentages in individual plots. In any case, this aspect, which would be necessary for the considerations of minor species, would seem to have no significant effect on the accuracy of dominant species.

The use of large-scale satellite data is an effective way to map forest tree species, which is a key aspect of planning, managing, and monitoring forests. In the future, further investigation will be necessary to ensure the robustness of the results, even in cases of mixed forest cover and the recognition of minor species. Additionally, scientific research can reveal the challenges of using field observations, such as NFI data, for classifying remotely sensed data. This study revealed the need for a reference dataset with accurate location and spatial distribution samples to represent the complexity of Italian forest cover, as well as the need for a sufficient number of samples. Investments in Earth Observation programs will be able to provide enough data in the future to ensure the continuous study of the forest environment. However, the importance of collecting samples through surveys as part of inventory censuses must also be considered. Integrating remote sensing data with other collective and diffuse sources seems essential for monitoring forest evolution and dynamics, particularly in light of climate change effects.

Chapter 6

Synthesis and Conclusion

6.1. Main results

This thesis examined the potential of spaceborne imaging spectroscopy, using PRISMA hyperspectral data as a case study, to support planning processes in forestry, agriculture, and urban green spaces. The findings demonstrate that hyperspectral sensors can provide highly detailed information, extending the capabilities of current multispectral missions such as Copernicus Sentinel-2 (Chapter 5, section 5.3). By addressing four research questions, the thesis highlights both the opportunities and limitations of this technology.

The first research question examined whether hyperspectral data could discriminate between land cover types, agricultural crops, urban and forest tree species, with very similar spectral signatures. The PRISMA data exhibited remarkable potential for thematic detail, with permanent crops, urban tree species, and forest stands dominated by spectrally similar genera all classified with meaningful accuracy. When applied to the agricultural domain, the best results — with F1 scores exceeding 0.70 for six out of ten permanent crops — were achieved using a convolutional neural network trained on a reduced hyperspectral cube of 156 bands (Chapter 2, section 2.3). These results confirm that hyperspectral data enable classification down to IV level of the Corine Land Cover legend, a level of detail rarely achievable with multispectral imagery. Even in highly fragmented and spectrally complex environments, such as mixed forests or urban environment, the rich spectral resolution of PRISMA was adequate to resolve differences between tree species or forest types, although mixed-cover stands remained more challenging (Chapter 4, section 4.3). The results of chapter 2, 3 and 4, showed that convolutional neural networks can handle the high dimensionality of hyperspectral data effectively without extensive feature reduction, particularly when using band-reduced cubes that balance dimensionality and information content.

However, as stated in chapter 5, Random forest model can also handle high dimensional datasets, and it is more robust against overfitting.

The second research question focused on integrating spatial and spectral information, particularly whether enhancing hyperspectral imagery with higher-resolution data could improve classification in fragmented urban settings. The pansharpening experiments demonstrated a significant increase in classification accuracy for urban tree species, with overall accuracy rising from 0.64 to 0.78 and class-specific F1 scores improving substantially (Chapter 3, section 3.3). Importantly, the spectral integrity of hyperspectral data was preserved, using the co-registered panchromatic band and avoiding distortions due to orthorectification of different sources. These results highlight that relatively simple preprocessing techniques can extend the applicability of hyperspectral imagery to contexts where spatial fragmentation is critical. This not only improves classification performance but also delivers actionable information for municipalities, which often face pressing policy and management demands regarding urban green infrastructure.

The third research question investigated whether hyperspectral satellite data could provide sufficient detail for forest areas classification despite their moderate GSD. Results indicate that PRISMA data can indeed achieve meaningful classification at the level of forest type and, in some cases, tree species (Chapter 4, section 4.3 and Chapter 5, section 5.3). However, it should be noted that pixels were assigned to a specific class during the labelling process, according to the dominant species of the considered stand. This method is more reliable for pure stands than for mixed stands. Thus, in the case of non-homogeneous forest cover, identifying the class of labeled (and classified) pixels is more difficult, which reveals the ongoing trade-off between spectral richness and spatial resolution.

Finally, the fourth research question addressed model generalization across a wide ecological gradient, from northern to southern Italy. The comparison between site-specific and generalized models showed that while site-specific models performed slightly better, generalized models offered distinct advantages for underrepresented classes (Chapter 5, section 5.3). In particular, generalized models slightly improved the classification of species with limited training data at individual sites, suggesting that pooling different training datasets from multiple sites can strengthen model robustness. Performance with PRISMA data was higher than with single Sentinel-2 acquisitions and comparable to Sentinel-2 time series and simulated Landsat Next data. These results highlight the effectiveness of hyperspectral and superspectral sensors in discriminating between spectrally similar classes, paving the way for wall-to-wall classification as future long-term missions become available.

Taken together, these findings confirm that PRISMA hyperspectral data can be effectively applied in real-world contexts ranging from agriculture crops to urban or forest trees classification and large-scale forest biodiversity monitoring. At the same time, the studies revealed limitations, particularly in mixed-cover classification, with a balance between spectral richness and spatial resolution and the dependency on high-quality reference data. Nevertheless, the inclusion of smartphone-collected ground-truth data allows to substantially increase the training data, demonstrating the potential of mobile crowd sensing with smartphone application, such as Eye-Land, to complement spaceborne acquisitions.

6.2. Conclusion

The synthesis of results across agricultural, urban, and forest applications shows that spaceborne imaging spectroscopy from the PRISMA precursor mission is not only a research tool, but also a practical resource for planning processes. This mission, with its very high spectral resolution, enables accurate classification in agricultural, forest and urban context, providing detailed thematic information (e.g., about permanent crops, urban tree species, forest tree stands). Such information can directly contribute to cartography and documentation required by planning tools detailed in Chapter 1, paragraph 1.4. "Planning Process". In this sense, future missions will be key instruments for addressing societal challenges linked to food security, urban resilience, and forest conservation.

Several cross-cutting conclusions emerge from this thesis. First, spaceborne hyperspectral imagery outperforms traditional multispectral single acquisitions and achieves accuracies comparable to multispectral time series. Second, integrating spatial and spectral detail—such as through pansharpening—substantially improves performance in fragmented urban contexts, expanding the scope of hyperspectral applications. Third, while moderate spatial resolution poses challenges in heterogeneous ecosystems, the spectral richness of hyperspectral sensors offsets these limitations, rendering them a valuable addition to existing multispectral programs. Fourth, the ability of generalized models to perform well across wide ecological gradients demonstrates the scalability of hyperspectral products and strengthens their potential for operational adoption at national or regional levels.

Despite these promising findings, the operational deployment of PRISMA-based applications appeared partly constrained. As a precursor and exploratory mission, PRISMA was not designed for continuous and systematic global coverage, but for on-demand acquisitions responding to user requests. This kind of service, combined with a high global demand for hyperspectral data, makes the timely acquisition of usable images challenging, especially under constraints related to seasonality or cloud conditions (Shaik et al., 2023). The revisit cycle further limits the monitoring of rapidly evolving characteristics, where canopy vegetation changes faster than the available temporal resolution can capture (Goetz et al., 2009) (Goetz et al., 2009), and even more so for hyperspectral sensors with less frequent acquisitions (Shaik et al., 2023). Moreover, while hyperspectral data offers substantial spectral richness, the technical effort needed in terms of calibration, atmospheric correction, and data handling may hinder its operational integration into planning workflows, especially for users lacking advanced processing capabilities. Data access policies and competition among users can also create bottlenecks, especially for regions with lower acquisition priority (Shaik et al., 2023). To maximize the value of the PRISMA data, fusion with multispectral sensors characterized by higher revisit rates can be a possible strategy, combining temporal repeatability with high spectral detail (Alparone et al., 2024).

However, these challenges reflect the developmental stage of satellite imaging spectroscopy worldwide, where existing systems such as PRISMA or EnMAP are pathfinders focused on scientific experimentation rather than operational continuity. The upcoming Copernicus CHIME mission will represent a major transition to routine global observations, supporting large-scale environmental monitoring and long-term operational uptake (Nieke et al., 2023). In this perspective, the present thesis contributes to building the knowledge to prepare operational applications for when stable hyperspectral data streams become available.

Looking ahead, there are several promising directions for future research. Multi-temporal imagery should be explored to account for phenological variability in agriculture and forestry, though the on-demand nature of PRISMA currently limits this potential. Data fusion with active sensors such as SAR or LiDAR could overcome limitations related to canopy complexity, offering structural information alongside spectral detail. Advanced approaches like spectral unmixing show promise for addressing mixed-cover challenges, particularly in forests. Finally, mobile crowd sensing offers a powerful avenue for enriching reference datasets and involving local networks of contributors in monitoring processes, thereby bridging the gap between spaceborne acquisitions and ground-based knowledge.

In conclusion, this thesis demonstrates that hyperspectral Earth Observation can meaningfully support planning in agriculture, forestry, and urban green areas. As future missions improve imagery characteristics, and as collaborative data collection expands, spaceborne imaging spectroscopy is poised to become a central tool for sustainable planning and environmental management.

References

Acito, N., Diani, M., Corsini, G., 2022. PRISMA Spatial Resolution Enhancement by Fusion With Sentinel-2 Data. IEEE J. Sel. Top. Appl. Earth Obs. Remote Sens. 15, 62–79. https://doi.org/10.1109/JSTARS.2021.3132135

Agnoletti, M., 2022. Atlante dei boschi italiani, Prima edizione. ed, I Robinson. Letture. Editori GLF Laterza, Bari.

Albrechts, L., 2004. Strategic (Spatial) Planning Reexamined. Environ. Plan. B Plan. Des. 31, 743–758. https://doi.org/10.1068/b3065

Alicandro, M., Candigliota, E., Dominici, D., Immordino, F., Masin, F., Pascucci, N., Quaresima, R., Zollini, S., 2022. Hyperspectral PRISMA and Sentinel-2 Preliminary Assessment Comparison in Alba Fucens and Sinuessa Archaeological Sites (Italy). Land 11, 2070. https://doi.org/10.3390/land11112070

Alonso, M.C., Malpica, J.A., de Agirre, A.M., 2011. Consequences of the Hughes phenomenon on some classification techniques.

Alonzo, M., Bookhagen, B., Roberts, D.A., 2014. Urban tree species mapping using hyperspectral and lidar data fusion. Remote Sens. Environ. 148, 70–83. https://doi.org/10.1016/j.rse.2014.03.018

Alparone, L., Aiazzi, B., Baronti, S., Garzelli, A., 2015. Remote Sensing Image Fusion, in: Remote Sensing Image Fusion. CRC Press, Boca Raton, p. 178. https://doi.org/10.1201/b18189

Alparone, L., Arienzo, A., Garzelli, A., 2024. Spatial Resolution Enhancement of Satellite Hyperspectral Data Via Nested Hyper-Sharpening With Sentinel-2 Multispectral Data. IEEE J.

Sel. Top. Appl. Earth Obs. Remote Sens. 1–11. https://doi.org/10.1109/JSTARS.2024.3406762

Amici, S., Piscini, A., 2021. Exploring PRISMA Scene for Fire Detection: Case Study of 2019 Bushfires in Ben Halls Gap National Park, NSW, Australia. Remote Sens. 13, 1410. https://doi.org/10.3390/rs13081410

Arun, S.A., Akila, A.S., 2023. Land-cover classification with hyperspectral remote sensing image using CNN and spectral band selection. Remote Sens. Appl. Soc. Environ. 31, 100986. https://doi.org/10.1016/j.rsase.2023.100986

Avery, T.E., Berlin, G.L., 1992. Fundamentals of remote sensing and airphoto interpretation. New York : Macmillan ; Toronto : Maxwell Macmillan Canada ; New York : Maxwell Macmillan International.

Baiocchi, V., Giannone, F., Monti, F., 2022. How to Orient and Orthorectify PRISMA Images and Related Issues. Remote Sens. 14, 1991. https://doi.org/10.3390/rs14091991

Bandyopadhyay, D., Mukherjee, S., Ball, J., Vincent, G., Coomes, D.A., Schönlieb, C.-B., 2023. Tree species classification from hyperspectral data using graph-regularized neural networks.

Barnsley, M.J., Settle, J.J., Cutter, M.A., Lobb, D.R., Teston, F., 2004. The PROBA/CHRIS mission: a low-cost smallsat for hyperspectral multiangle observations of the Earth surface and atmosphere. IEEE Trans. Geosci. Remote Sens. 42, 1512–1520. https://doi.org/10.1109/TGRS.2004.827260

Belgiu, M., Drăguţ, L., 2016. Random forest in remote sensing: A review of applications and future directions. ISPRS J. Photogramm. Remote Sens. 114, 24–31. https://doi.org/10.1016/j.isprsjprs.2016.01.011

Bjerreskov, K.S., Nord-Larsen, T., Fensholt, R., 2021. Classification of Nemoral Forests with Fusion of Multi-Temporal Sentinel-1 and 2 Data. Remote Sens. 13, 950. https://doi.org/10.3390/rs13050950

Blasi, C., Capotorti ,G., Copiz ,R., Guida ,D., Mollo ,B., Smiraglia ,D., and Zavattero, L., 2014. Classification and mapping of the ecoregions of Italy. Plant Biosyst. - Int. J. Deal. Asp. Plant Biol. 148, 1255–1345. https://doi.org/10.1080/11263504.2014.985756

Blasi, C., Capotorti, G., Copiz, R., Guida, D., Mollo, B., Smiraglia, D., Zavattero, L., 2018. Terrestrial Ecoregions of Italy.

Blasi, C., Capotorti, Giulia, Smiraglia, D., Guida, D., Zavattero, L., Frondoni, Raffaella, Copiz, Riccardo, Marzio, P.D., Siervo, V., Michetti, L., Teodonio, L., Anzellotti, I., Bonacquisti, S., Azzella, M.M., Burrascano, S., Capotorti, G, Copiz, R, Frondoni, R, Lasen, C., 2010. The Ecoregions of Italy - A thematic contribution to the National Biodiversity Strategy.

Blickensdörfer, L., Oehmichen, K., Pflugmacher, D., Kleinschmit, B., Hostert, P., 2024. National tree species mapping using Sentinel-1/2 time series and German National Forest Inventory data. Remote Sens. Environ. 304, 114069. https://doi.org/10.1016/j.rse.2024.114069

Bolyn, C., Lejeune, P., Michez, A., Latte, N., 2022. Mapping tree species proportions from satellite imagery using spectral–spatial deep learning. Remote Sens. Environ. 280, 113205. https://doi.org/10.1016/j.rse.2022.113205

Boncori, M., Peter, J., 2016. Caveats Concerning the Use of SRTM DEM Version 4.1 (CGIAR-CSI). Remote Sens. 8, 793. https://doi.org/10.3390/rs8100793

Breiman, L., 2001. Random Forests. Mach. Learn. 45, 5–32. https://doi.org/10.1023/A:1010933404324

Brivio, P.A., Lechi, G., Zilioli, E., 2006. Principi e metodi di telerilevamento. CittàStudi.

Brockerhoff, E.G., Barbaro, L., Castagneyrol, B., Forrester, D.I., Gardiner, B., González-Olabarria, J.R., Lyver, P.O., Meurisse, N., Oxbrough, A., Taki, H., Thompson, I.D., van der Plas, F., Jactel, H., 2017. Forest biodiversity, ecosystem functioning and the provision of ecosystem services. Biodivers. Conserv. 26, 3005–3035. https://doi.org/10.1007/s10531-017-1453-2

Büttner, G., Feranec, J., Jaffrain, G., Mari, L., Maucha, G., Soukup, T., 2004. The corine land cover 2000 project 331–346.

Campbell, J.B., Wynne, R.H., 2011. Introduction to Remote Sensing, fifth. ed. Guilford Press.

Campbell, S., 1996. Green Cities, Growing Cities, Just Cities?: Urban Planning and the Contradictions of Sustainable Development. J. Am. Plann. Assoc. 62, 296–312. https://doi.org/10.1080/01944369608975696

Cao, F., Yang, Z., Ren, J., Mengying, J., Ling, W.-K., 2017. Does Normalization Methods Play a Role for Hyperspectral Image Classification?

Capolupo, A., 2021. Improving the Accuracy of Global DEM of Differences (DoD) in Google Earth Engine for 3-D Change Detection Analysis. IEEE J. Sel. Top. Appl. Earth Obs. Remote Sens. 14, 12332–12347. https://doi.org/10.1109/JSTARS.2021.3130063

Capolupo, A., Kooistra, L., Berendonk, C., Boccia, L., Suomalainen, J., 2015. Estimating Plant Traits of Grasslands from UAV-Acquired Hyperspectral Images: A Comparison of Statistical Approaches. ISPRS Int. J. Geo-Inf. 4, 2792–2820. https://doi.org/10.3390/ijgi4042792

Caporusso, G., Ettore, L., Rino, L., Rosa, L., Rocchina, G., Girolamo, D.M., Patrizia, S., 2020. The Hyperspectral Prisma Mission in Operations, in: IGARSS 2020 - 2020 IEEE International Geoscience and Remote Sensing Symposium. Presented at the IGARSS 2020 - 2020 IEEE International Geoscience and Remote Sensing Symposium, IEEE, Waikoloa, HI, USA, pp. 3282–3285. https://doi.org/10.1109/IGARSS39084.2020.9323301

Caputi, E., Delogu, G., Patriarca, A., Perretta, M., Mancini, G., Boccia, L., Recanatesi, F., Ripa, M.N., 2025. Comparison of Tree Typologies Mapping Using Random Forest Classifier Algorithm of PRISMA and Sentinel-2 Products in Different Areas of Central Italy. Remote Sens. 17, 356. https://doi.org/10.3390/rs17030356

Casalegno, S., Anderson, K., Cox, D.T.C., Hancock, S., Gaston, K.J., 2017. Ecological connectivity in the three-dimensional urban green volume using waveform airborne lidar. Sci. Rep. 7, 45571. https://doi.org/10.1038/srep45571

Casavecchia, S., Allegrezza, M., Biondi, E., Galli, A., Marcheggiani, E., Pesaresi, S., Taffetani, F., Tavoletti, S., Zitti, S., Bianchelli, M., Biscotti, N., Facchi, J., Galdenzi, D., Galié, M., Gasparri, R., Iommarini, L., Lancioni, A., Lucchetti, L., Mei, G., Micheletti, A., Montecchiari, S., Morbidoni, M., Ottaviani, C., Pinzi, M., Rismondo, M., Tesei, G., Zivkovic, L., 2020. Conservation and Management of Biodiversity and Landscapes: A Challenge in the Era of Global Change, in: Longhi, S., Monteriù, A., Freddi, A., Aquilanti, L., Ceravolo, M.G., Carnevali, O., Giordano, M., Moroncini, G. (Eds.), The First Outstanding 50 Years of "Università Politecnica Delle Marche": Research Achievements in Life Sciences. Springer International Publishing, Cham, pp. 483–503. https://doi.org/10.1007/978-3-030-33832-9_32

Cavalli, R.M., 2023. The Weight of Hyperion and PRISMA Hyperspectral Sensor Characteristics on Image Capability to Retrieve Urban Surface Materials in the City of Venice. Sensors 23, 454. https://doi.org/10.3390/s23010454

Cena, H., Labra, M., 2024. Biodiversity and planetary health: a call for integrated action. The Lancet 403, 1985–1986. https://doi.org/10.1016/S0140-6736(24)00292-7

Città Metropolitana di Napoli - SIT [WWW Document], n.d. URL https://sit.cittametropolitana.na.it/ (accessed 8.2.24).

Cogliati, S., Sarti, F., Chiarantini, L., Cosi, M., Lorusso, R., Lopinto, E., Miglietta, F., Genesio, L., Guanter, L., Damm, A., Pérez-López, S., Scheffler, D., Tagliabue, G., Panigada, C., Rascher, U., Dowling, T.P.F., Giardino, C., Colombo, R., 2021. The PRISMA imaging spectroscopy mission: overview and first performance analysis. Remote Sens. Environ. 262, 112499. https://doi.org/10.1016/j.rse.2021.112499

Comune di Napoli, 2021a. Manutenzione del verde ed igiene della città [WWW Document]. www.comune.napoli.it. URL https://www.comune.napoli.it/flex/cm/pages/ServeBLOB.php/L/IT/IDPagina/47672 (accessed 8.1.24).

Comune di Napoli, 2021b. Bilancio arboreo e gestione del verde della città di Napoli [WWW Document]. www.comune.napoli.it. URL https://www.comune.napoli.it/flex/cm/pages/ServeBLOB.php/L/IT/IDPagina/29726 (accessed 8.1.24).

Congalton, R., 2001. Accuracy assessment and validation of remotely sensed and other spatial information. Int. J. WILDLAND FIRE 10, 321–328. https://doi.org/10.1071/WF01031

Copernicus, 2023. Copernicus Annual Reports – Documentation. Frankfurt am Main, Germany.

CREA, 2023. Giornata Internazionale delle Foreste: verso l'Inventario Nazionale 2025 - Giornata Internazionale delle Foreste: verso l'Inventario Nazionale 2025 - CREA [WWW Document]. URL https://www.crea.gov.it/en/-/giornata-internazionale-delle-foreste-verso-l-inventario-nazionale-2025 (accessed 7.23.24).

CREA - MASAF, 2020. Carta Forestale d'Italia - Forest map of Italy. CREA - Consiglio per la Ricerca in Agricoltura e l'Analisi dell'Economia Agraria, Council for Agricultural Research and Analysis of Agricultural Economics. MASAF - Ministero dell'Agricoltura, della Sovranità Alimentare e delle Foreste, Ministry of Agriculture, Food Sovereignty and Forestry. Available on: https://cfi-sinfor.crea.gov.it (accessed on 2025-05-21).

CUAS, 2009. Carta Utilizzazione Agricola dei Suoli | Geoportale Regione Campania - Agricultural Land Use Map | Campania Region Geoportal.

Dainelli, N., 2011. L'osservazione della terra - Telerilevamento. Earth Observation - Remote Sensing. D. Flaccovio.

Dalponte, M., Bruzzone, L., Gianelle, D., 2012. Tree species classification in the Southern Alps based on the fusion of very high geometrical resolution multispectral/hyperspectral images and LiDAR data. Remote Sens. Environ. 123, 258–270. https://doi.org/10.1016/j.rse.2012.03.013

Davoudi, S., 2006. Evidence-Based Planning: Rhetoric and Reality. DisP - Plan. Rev. 42, 14–24. https://doi.org/10.1080/02513625.2006.10556951

De Luca, G., Carotenuto, F., Genesio, L., Pepe, M., Toscano, P., Boschetti, M., Miglietta, F., Gioli, B., 2024. Improving PRISMA hyperspectral spatial resolution and geolocation by using Sentinel-2: development and test of an operational procedure in urban and rural areas. ISPRS J. Photogramm. Remote Sens. 215, 112–135. https://doi.org/10.1016/j.isprsjprs.2024.07.003

De Toni, A., Roganti, R., Ronchi, S., Salata, S., 2023. Monitoring Recent Afforestation Interventions as Relevant Issue for Urban Planning, in: Gervasi, O., Murgante, B., Rocha, A.M.A.C., Garau, C., Scorza, F., Karaca, Y., Torre, C.M. (Eds.), Computational Science and Its Applications – ICCSA 2023 Workshops. Springer Nature Switzerland, Cham, pp. 578–595. https://doi.org/10.1007/978-3-031-37111-0_40

Delogu, G., Caputi, E., Perretta, M., Ripa, M.N., Boccia, L., 2023. Using PRISMA Hyperspectral Data for Land Cover Classification with Artificial Intelligence Support. Sustain. Switz. 15. https://doi.org/10.3390/su151813786

Delogu, G., Perretta, M., Caputi, E., Patriarca, A., Funsten, C.C., Recanatesi, F., Ripa, M.N., Boccia, L., 2024. Leveraging the Potential of PRISMA Hyperspectral Data for Forest Tree Species Classification: A Case Study in Southern Italy. Remote Sens. 16, 4788. https://doi.org/10.3390/rs16244788

Di Palma, M., Rigillo, M., Leone, M.F., 2024. Remote Sensing Technologies for Mapping Ecosystem Services: An Analytical Approach for Urban Green Infrastructure. Sustainability 16, 6220. https://doi.org/10.3390/su16146220

Dian, Y., Pang, Y., Dong, Y., Li, Z., 2016. Urban Tree Species Mapping Using Airborne LiDAR and Hyperspectral Data. J. Indian Soc. Remote Sens. 44, 595–603. https://doi.org/10.1007/s12524-015-0543-4

Drusch, M., Del Bello, U., Carlier, S., Colin, O., Fernandez, V., Gascon, F., Hoersch, B., Isola, C., Laberinti, P., Martimort, P., Meygret, A., Spoto, F., Sy, O., Marchese, F., Bargellini, P., 2012. Sentinel-2: ESA's Optical High-Resolution Mission for GMES Operational Services. Remote Sens. Environ., The Sentinel Missions - New Opportunities for Science 120, 25–36. https://doi.org/10.1016/j.rse.2011.11.026

Ellison, D., Morris, C.E., Locatelli, B., Sheil, D., Cohen, J., Murdiyarso, D., Gutierrez, V., Noordwijk, M. van, Creed, I.F., Pokorny, J., Gaveau, D., Spracklen, D.V., Tobella, A.B., Ilstedt, U., Teuling, A.J., Gebrehiwot, S.G., Sands, D.C., Muys, B., Verbist, B., Springgay, E., Sugandi, Y., Sullivan, C.A., 2017. Trees, forests and water: Cool insights for a hot world. Glob. Environ. Change 43, 51–61. https://doi.org/10.1016/j.gloenvcha.2017.01.002

EUROSTAT, 2022. LUCAS 2022 - (Land Use / Cover Area Frame Survey), E4.LUCAS (ESTAT).

EyeLand App, 2024. EyeLand App [WWW Document]. URL https://prineyeland.it/ (accessed 11.4.24).

Fabbrini, F., 2022. Italy's national recovery and resilience plan: context, content and challenges. J. Mod. Ital. Stud. 27, 658–676. https://doi.org/10.1080/1354571X.2022.2124672

FAO, 2024. The State of the World's Forests 2024, The State of the World's Forests. FAO, Rome, Italy. https://doi.org/10.4060/cd1211en

FAO, 2021. The State of the World's Land and Water Resources for Food and Agriculture – Systems at breaking point (SOLAW 2021). FAO. https://doi.org/10.4060/cb7654en

Farr, T.G., Rosen, P.A., Caro, E., Crippen, R., Duren, R., Hensley, S., Kobrick, M., Paller, M., Rodriguez, E., Roth, L., Seal, D., Shaffer, S., Shimada, J., Umland, J., Werner, M., Oskin, M., Burbank, D., Alsdorf, D., 2007. The Shuttle Radar Topography Mission. Rev. Geophys. 45. https://doi.org/10.1029/2005RG000183

Fassnacht, F.E., Latifi, H., Stereńczak, K., Modzelewska, A., Lefsky, M., Waser, L.T., Straub, C., Ghosh, A., 2016. Review of studies on tree species classification from remotely sensed data. Remote Sens. Environ. 186, 64–87. https://doi.org/10.1016/j.rse.2016.08.013

Ferster, C.J., Coops, N.C., 2016. Integrating volunteered smartphone data with multispectral remote sensing to estimate forest fuels. Int. J. Digit. Earth 9, 171–196. https://doi.org/10.1080/17538947.2014.1002865

Fichera, C.R., Modica, G., Pollino, M., 2011. GIS and Remote Sensing to Study Urban-Rural Transformation During a Fifty-Year Period, in: Murgante, B., Gervasi, O., Iglesias, A., Taniar, D., Apduhan, B.O. (Eds.), Computational Science and Its

Applications - ICCSA 2011. Springer, Berlin, Heidelberg, pp. 237–252. https://doi.org/10.1007/978-3-642-21928-3_17
Field, E., Hector, A., Barsoum, N., Koricheva, J., 2025. Tree diversity reduces pathogen damage in temperate forests: A systematic review and meta-analysis. For. Ecol. Manag. 578, 122398. https://doi.org/10.1016/j.foreco.2024.122398
Filchev, L., 2014. Satellite Hyperspectral Earth Observation Missions – A Review. Aerosp. Res. Bulg. 26, 191–207.
Flynn, K.C., Frazier, A.E., Admas, S., 2020. Nutrient Prediction for Tef (Eragrostis tef) Plant and Grain with Hyperspectral Data and Partial Least Squares Regression: Replicating Methods and Results across Environments. Remote Sens. 12, 2867. https://doi.org/10.3390/rs12182867
Foody, G.M., 2002. Status of land cover classification accuracy assessment. Remote Sens. Environ. 80, 185–201. https://doi.org/10.1016/S0034-4257(01)00295-4
Francini, S., Schelhaas, M.-J., Vangi, E., Lerink, B., Nabuurs, G.-J., McRoberts, R.E., Chirici, G., 2024. Forest species mapping and area proportion estimation combining Sentinel-2 harmonic predictors and national forest inventory data. Int. J. Appl. Earth Obs. Geoinformation 131, 103935. https://doi.org/10.1016/j.jag.2024.103935
Frantz, D., Haß, E., Uhl, A., Stoffels, J., Hill, J., 2018. Improvement of the Fmask algorithm for Sentinel-2 images: Separating clouds from bright surfaces based on parallax effects. Remote Sens. Environ. 215, 471–481. https://doi.org/10.1016/j.rse.2018.04.046
Fricker, G.A., Ventura, J.D., Wolf, J.A., North, M.P., Davis, F.W., Franklin, J., 2019. A Convolutional Neural Network Classifier Identifies Tree Species in Mixed-Conifer Forest from Hyperspectral Imagery. Remote Sens. 11, 2326. https://doi.org/10.3390/rs11192326
Friedman, J.H., 1997. On Bias, Variance, 0/1—Loss, and the Curse-of-Dimensionality. Data Min. Knowl. Discov. 1, 55–77. https://doi.org/10.1023/A:1009778005914
Friedmann, J., 1998. Planning theory revisited*. Eur. Plan. Stud. 6, 245–253. https://doi.org/10.1080/09654319808720459

Fritz, S., Fonte, C.C., See, L., 2017. The Role of Citizen Science in Earth Observation. Remote Sens. 9, 357. https://doi.org/10.3390/rs9040357

Fu, J., Dupre, K., Tavares, S., King, D., Banhalmi-Zakar, Z., 2022. Optimized greenery configuration to mitigate urban heat: A decade systematic review. Front. Archit. Res. 11, 466–491. https://doi.org/10.1016/j.foar.2021.12.005

Fuentealba, A., Alfaro, R., Bauce, É., 2013. Theoretical framework for assessment of risks posed to Canadian forests by invasive insect species. For. Ecol. Manag. 302, 97–106. https://doi.org/10.1016/j.foreco.2013.03.023

Fuentes, S., Tongson, E., Gonzalez Viejo, C., 2021. Urban Green Infrastructure Monitoring Using Remote Sensing from Integrated Visible and Thermal Infrared Cameras Mounted on a Moving Vehicle. Sensors 21, 295. https://doi.org/10.3390/s21010295

Gabellini, P., 2001. Tecniche urbanistiche - Urban planning techniques.

Gabriele, M., Brumana, R., Previtali, M., Cazzani, A., 2023. A combined GIS and remote sensing approach for monitoring climate change-related land degradation to support landscape preservation and planning tools: the Basilicata case study. Appl. Geomat. 15, 497–532. https://doi.org/10.1007/s12518-022-00437-z

Galeazzi, C., Carpentiero, R., Varacalli, G., 2013. The PRISMA system and PAN/HYP instrument 10.

Gao, Y., Mas, J.F., 2008. A comparison of the performance of pixel-based and object-based classifications over images with various spatial resolutions.

Gasparini, di P., Floris, A., Rizzo, M., Patrone, A., Credentino, L., Papitto, G., Martino, D.D., 2020. Il terzo inventario forestale nazionale italiano INFC2015:

Gasparini, P., Bruzzone, L., Ferrari, M., 2024. Classificazione di coperture forestali con dati iperspettrali della missione PRISMA e tecniche di apprendimento automatico per l'impiego negli inventari forestali.

Gasparini, P., Di Cosmo, L., Floris, A., 2022. Area and Characteristics of Italian Forests, in: Gasparini, P., Di Cosmo, L., Floris, A., De Laurentis, D. (Eds.), Italian National Forest Inventory—Methods and Results of the Third Survey: Inventario Nazionale Delle Foreste e Dei Serbatoi Forestali Di Carbonio—Metodi e Risultati Della Terza Indagine. Springer International Publishing, Cham, pp. 151–325. https://doi.org/10.1007/978-3-030-98678-0_7

Gasparini, P., Di Cosmo, L., Floris, A., Murgia, F., Rizzo, M., 2025. Open Georeferenced Field Data on Forest Types and Species for Biodiversity Assessment and Remote Sensing Applications. Data 10, 30. https://doi.org/10.3390/data10030030

Gasparini, P., Di Cosmo, L., Floris, A., Notarangelo, G., Rizzo, M., 2016. Guida per i rilievi in campo. INFC2015 – Terzo inventario forestale nazionale. - Guide for field surveys. INFC2015 – Third National Forest Inventory.

Ghasemi, N., Justo, J.A., Celesti, M., Despoisse, L., Nieke, J., 2024. Onboard Processing of Hyperspectral Imagery: Deep Learning Advancements, Methodologies, Challenges, and Emerging Trends.

Giordano, A., Caprio, A., Natale, M., 2003. Terra di lavoro. Guida Editori.

Goetz, S.J., Baccini, A., Laporte, N.T., Johns, T., Walker, W., Kellndorfer, J., Houghton, R.A., Sun, M., 2009. Mapping and monitoring carbon stocks with satellite observations: a comparison of methods. Carbon Balance Manag. 4, 2. https://doi.org/10.1186/1750-0680-4-2

Gomarasca, M., Angelo, 1997. Introduzione a Remote Sensing e GIS per la Gestione delle Risorse Agricole e Ambientali - Introduction to Remote Sensing and GIS for the management of the Agricultural and Environmental resources, 2nd ed. AIT (Associazione Italiana di telerilevamento).

Gomarasca, M.A., 2009. Basics of Geomatics. Springer Netherlands, Dordrecht. https://doi.org/10.1007/978-1-4020-9014-1

Goodenough, D.G., Dyk, A., Niemann, K.O., Pearlman, J.S., Chen, H., Han, T., Murdoch, M., West, C., 2003. Processing Hyperion and

ALI for forest classification. IEEE Trans. Geosci. Remote Sens. 41, 1321–1331. https://doi.org/10.1109/TGRS.2003.813214
Goodspeed, R., Liu, R., Gounaridis, D., Lizundia, C., Newell, J., 2022. A regional spatial planning model for multifunctional green infrastructure. Environ. Plan. B Urban Anal. City Sci. 49, 815–833. https://doi.org/10.1177/23998083211033610
Gouldson, A., Colenbrander, S., Sudmant, A., Papargyropoulou, E., Kerr, N., McAnulla, F., Hall, S., 2016. Cities and climate change mitigation: Economic opportunities and governance challenges in Asia. Cities, Cities, Energy and Climate Change Mitigation 54, 11–19. https://doi.org/10.1016/j.cities.2015.10.010
Govender, M., Chetty, K., Bulcock, H., 2009. A review of hyperspectral remote sensing and its application in vegetation and water resource studies. Water SA 33. https://doi.org/10.4314/wsa.v33i2.49049
Grabska, E., Hostert, P., Pflugmacher, D., Ostapowicz, K., 2019. Forest Stand Species Mapping Using the Sentinel-2 Time Series. Remote Sens. 11, 1197. https://doi.org/10.3390/rs11101197
Grandini, M., Bagli, E., Visani, G., 2020. Metrics for Multi-Class Classification: an Overview.
Guanter, L., Irakulis-Loitxate, I., Gorroño, J., Sánchez-García, E., Cusworth, D.H., Varon, D.J., Cogliati, S., Colombo, R., 2021. Mapping methane point emissions with the PRISMA spaceborne imaging spectrometer. Remote Sens. Environ. 265, 112671. https://doi.org/10.1016/j.rse.2021.112671
Guanter, L., Kaufmann, H., Segl, K., Foerster, S., Rogass, C., Chabrillat, S., Kuester, T., Hollstein, A., Rossner, G., Chlebek, C., Straif, C., Fischer, S., Schrader, S., Storch, T., Heiden, U., Mueller, A., Bachmann, M., Mühle, H., Müller, R., Habermeyer, M., Ohndorf, A., Hill, J., Buddenbaum, H., Hostert, P., Van der Linden, S., Leitão, P.J., Rabe, A., Doerffer, R., Krasemann, H., Xi, H., Mauser, W., Hank, T., Locherer, M., Rast, M., Staenz, K., Sang, B., 2015. The EnMAP Spaceborne Imaging Spectroscopy Mission for Earth Observation. Remote Sens. 7, 8830–8857. https://doi.org/10.3390/rs70708830

Guarini, R., Loizzo, R., Facchinetti, C., Longo, F., Ponticelli, B., Faraci, M., Dami, M., Cosi, M., Amoruso, L., De Pasquale, V., Taggio, N., Santoro, F., Colandrea, P., Miotti, E., Di Nicolantonio, W., 2018. Prisma Hyperspectral Mission Products, in: IGARSS 2018 - 2018 IEEE International Geoscience and Remote Sensing Symposium. Presented at the IGARSS 2018 - 2018 IEEE International Geoscience and Remote Sensing Symposium, IEEE, Valencia, pp. 179–182. https://doi.org/10.1109/IGARSS.2018.8517785

Habitats Directive - 92/43/EEC, 1992.

Haboudane, D., Miller, J.R., Pattey, E., Zarco-Tejada, P.J., Strachan, I.B., 2004. Hyperspectral vegetation indices and novel algorithms for predicting green LAI of crop canopies: Modeling and validation in the context of precision agriculture. Remote Sens. Environ. 90, 337–352. https://doi.org/10.1016/j.rse.2003.12.013

Hansen, A.J., Noble, B.P., Veneros, J., East, A., Goetz, S.J., Supples, C., Watson, J.E.M., Jantz, P.A., Pillay, R., Jetz, W., Ferrier, S., Grantham, H.S., Evans, T.D., Ervin, J., Venter, O., Virnig, A.L.S., 2021. Toward monitoring forest ecosystem integrity within the post-2020 Global Biodiversity Framework. Conserv. Lett. 14, e12822. https://doi.org/10.1111/conl.12822

Hasan, M., Ullah, S., Khan, M.J., Khurshid, K., 2019. Comparative analysis of SVM, ann and cnn for classifying vegetation species using hyperspectral thermal infrared data. Presented at the International Archives of the Photogrammetry, Remote Sensing and Spatial Information Sciences - ISPRS Archives, pp. 1861–1868. https://doi.org/10.5194/isprs-archives-XLII-2-W13-1861-2019

Healey, P., 1997. Collaborative Planning. Macmillan Education UK, London. https://doi.org/10.1007/978-1-349-25538-2

Heikkinen, V., Tokola, T., Parkkinen, J., Korpela, I., Jaaskelainen, T., 2010. Simulated Multispectral Imagery for Tree Species Classification Using Support Vector Machines. IEEE Trans. Geosci. Remote Sens. 48, 1355–1364. https://doi.org/10.1109/TGRS.2009.2032239

Hemmerling, J., Pflugmacher, D., Hostert, P., 2021. Mapping temperate forest tree species using dense Sentinel-2 time series. Remote Sens. Environ. 267, 112743. https://doi.org/10.1016/j.rse.2021.112743

Hermosilla, T., Bastyr, A., Coops, N.C., White, J.C., Wulder, M.A., 2022. Mapping the presence and distribution of tree species in Canada's forested ecosystems. Remote Sens. Environ. 282, 113276. https://doi.org/10.1016/j.rse.2022.113276

Hof, A.R., Dymond, C.C., Mladenoff, D.J., 2017. Climate change mitigation through adaptation: the effectiveness of forest diversification by novel tree planting regimes. Ecosphere 8, e01981. https://doi.org/10.1002/ecs2.1981

Hong, D., Li, C., Yokoya, N., Zhang, B., Jia, X., Plaza, A., Gamba, P., Benediktsson, J.A., Chanussot, J., 2025. Hyperspectral Imaging. https://doi.org/10.48550/arXiv.2508.08107

Hong, D., Yokoya, N., Chanussot, J., Xu, J., Zhu, X.X., 2019. Learning to propagate labels on graphs: An iterative multitask regression framework for semi-supervised hyperspectral dimensionality reduction. ISPRS J. Photogramm. Remote Sens. 158, 35–49. https://doi.org/10.1016/j.isprsjprs.2019.09.008

Hu, W., Huang, Y., Wei, L., Zhang, F., Li, H., 2015. Deep Convolutional Neural Networks for Hyperspectral Image Classification. J. Sens. 2015, 1–12. https://doi.org/10.1155/2015/258619

Hu, Z., Chu, Y., Zhang, Y., Zheng, X., Wang, Jingzhe, Xu, W., Wang, Jing, Wu, G., 2024. Scale matters: How spatial resolution impacts remote sensing based urban green space mapping? Int. J. Appl. Earth Obs. Geoinformation 134, 104178. https://doi.org/10.1016/j.jag.2024.104178

Huang, C., Davis, L.S., Townshend, J.R.G., 2002. An assessment of support vector machines for land cover classification. Int. J. Remote Sens. 23, 725–749. https://doi.org/10.1080/01431160110040323

Huang, S., Tang, L., Hupy, J.P., Wang, Y., Shao, G., 2021. A commentary review on the use of normalized difference vegetation index (NDVI) in the era of popular remote sensing. J. For. Res. 32, 1–6. https://doi.org/10.1007/s11676-020-01155-1

Hughes, G., 1968. On the mean accuracy of statistical pattern recognizers. IEEE Trans. Inf. Theory 14, 55–63. https://doi.org/10.1109/TIT.1968.1054102

INFC, 2015. National Inventory of Forests and forest Carbon pools - INFC - Italian National Forest Inventory [WWW Document]. Natl. Inventory For. For. Carbon Pools. URL https://www.inventarioforestale.org/it/superficie-e-composizione-area-and-composition/ (accessed 6.17.25).

IPCC, 2023. Climate Change 2023: Synthesis Report. Contribution of Working Groups I, II and III to the Sixth Assessment Report of the Intergovernmental Panel on Climate Change. Intergovernmental Panel on Climate Change (IPCC), Geneva, Switzerland. https://doi.org/10.59327/IPCC/AR6-9789291691647

ISPRA, 2021. Uso del suolo 2021 | Uso, copertura e consumo di suolo [WWW Document]. URL https://groupware.sinanet.isprambiente.it/uso-copertura-e-consumo-di-suolo/library/copertura-del-suolo/carta-di-copertura-del-suolo/uso-del-suolo-2021 (accessed 8.1.24).

ISTAT, 2024. Annuario statistico italiano - Italian Statistical Yearbook, Fuori Collana – Prodotto Flagship.

ISTAT, 2023. Classification of Municipalities according to the Italian Ecoregions.

ISTAT, 2011. Istat Data [WWW Document]. URL https://esploradati.istat.it/databrowser/#/en/dw (accessed 9.20.24).

Italian Constitution, Article 117, 2001. Costituzione, Articolo 117 | Repubblica italiana - Constitution, Article 117 | Italian Republic.

Italian Republic, 2013. Norme per lo sviluppo degli spazi verdi urbani - LEGGE 14 gennaio 2013, n. 10.

Jamali, A., 2019. Evaluation and comparison of eight machine learning models in land use/land cover mapping using Landsat 8 OLI: a case study of the northern region of Iran. SN Appl. Sci. 1, 1448. https://doi.org/10.1007/s42452-019-1527-8

Jena, B., Saxena, S., Nayak, G.K., Saba, L., Sharma, N., Suri, J.S., 2021. Artificial intelligence-based hybrid deep learning models for image classification: The first narrative review. Comput. Biol. Med. 137, 104803. https://doi.org/10.1016/j.compbiomed.2021.104803

Jia, J., Wang, Y., Chen, J., Guo, R., Shu, R., Wang, J., 2020. Status and application of advanced airborne hyperspectral imaging technology: A review. Infrared Phys. Technol. 104, 103115. https://doi.org/10.1016/j.infrared.2019.103115

Jia, X., 2022. Field Guide to Hyperspectral/Multispectral Image Processing. SPIE. https://doi.org/10.1117/3.2625662

Jolliffe, I.T., 1986. Principal Component Analysis and Factor Analysis, in: Jolliffe, I.T. (Ed.), Principal Component Analysis, Springer Series in Statistics. Springer, New York, NY, pp. 115–128. https://doi.org/10.1007/978-1-4757-1904-8_7

Kacic, P., Kuenzer, C., 2022. Forest Biodiversity Monitoring Based on Remotely Sensed Spectral Diversity—A Review. Remote Sens. 14, 5363. https://doi.org/10.3390/rs14215363

Kerrache, C.A., Sahraoui, Y., Calafate, C.T., Vegni, A.M. (Eds.), 2025. Mobile Crowdsensing and Remote Sensing in Smart Cities, Internet of Things. Springer Nature Switzerland, Cham. https://doi.org/10.1007/978-3-031-72732-0

Kokal, A.T., Ismailoglu, I., Musaoglu, N., 2022. COMPARISON of LANDSAT-9 and PRISMA SATELLITE DATA for LAND USE / LAND COVER CLASSIFICATION. Presented at the International Archives of the Photogrammetry, Remote Sensing and Spatial Information Sciences - ISPRS Archives, pp. 197–201. https://doi.org/10.5194/isprs-Archives-XLVI-M-2-2022-197-2022

Kokhanovsky, A., Di Mauro, B., Colombo, R., 2022. Snow surface properties derived from PRISMA satellite data over the Nansen Ice Shelf (East Antarctica). Front. Environ. Sci. 10. https://doi.org/10.3389/fenvs.2022.904585

Korpela, I., Ørka, H.O., Hyyppä, J., Heikkinen, V., Tokola, T., 2010. Range and AGC normalization in airborne discrete-return LiDAR intensity data for forest canopies. ISPRS J. Photogramm.

Remote Sens. 65, 369–379. https://doi.org/10.1016/j.isprsjprs.2010.04.003
Kosmala, M., Crall, A., Cheng, R., Hufkens, K., Henderson, S., Richardson, A.D., 2016. Season Spotter: Using Citizen Science to Validate and Scale Plant Phenology from Near-Surface Remote Sensing. Remote Sens. 8, 726. https://doi.org/10.3390/rs8090726
Kottek, M., Grieser, J., Beck, C., Rudolf, B., Rubel, F., 2006. World Map of the Köppen-Geiger climate classification updated. Meteorol. Z. 15, 259–263. https://doi.org/10.1127/0941-2948/2006/0130
Kuhn, M., 2008. Building Predictive Models in R Using the caret Package. J. Stat. Softw. 28, 1–26. https://doi.org/10.18637/jss.v028.i05
Laino, E., Iglesias, G., 2023. Extreme climate change hazards and impacts on European coastal cities: A review. Renew. Sustain. Energy Rev. 184, 113587. https://doi.org/10.1016/j.rser.2023.113587
Landgrebe, D., 2002. Hyperspectral Image Data Analysis as a High Dimensional Signal Processing Problem. IEEE Signal Process. Mag.
LARP, 2023a. LarpUnina/PrismaTool [WWW Document]. URL https://github.com/LarpUnina/PrismaTool (accessed 8.6.25).
LARP, 2023b. PrismaTool [WWW Document]. URL https://github.com/LarpUnina/PrismaTool (accessed 7.31.24).
Law no. 10, 2013. Norme per lo sviluppo degli spazi verdi urbani - Standards for the development of urban green spaces.
Law no. 142, 1990. Ordinamento delle autonomie locali - Local government system.
Law no. 194, 1991. Legge quadro sulle aree protette - Framework Law on Protected Areas.
Law no. 431, 1985. “Galasso” - Disposizioni urgenti per la tutela delle zone di particolare interesse ambientale - Urgent measures for the protection of areas of particular environmental interest.
Law no. 1150, 1942. LEGGE URBANISTICA FONDAMENTALE - FUNDAMENTAL URBAN PLANNING LAW.

Legislative Decree no. 34, 2018. Testo unico in materia di foreste e filiere forestali - Forests & forest supply chains.

Legislative Decree no. 42, 2004. Codice dei beni culturali e del paesaggio - Code of Cultural Heritage and Landscape.

Lemenkova, P., Debeir, O., 2023. Computing Vegetation Indices from the Satellite Images Using GRASS GIS Scripts for Monitoring Mangrove Forests in the Coastal Landscapes of Niger Delta, Nigeria. J. Mar. Sci. Eng. 11, 871. https://doi.org/10.3390/jmse11040871

Leone, A., 2019. Ambiente e pianificazione. Uso del suolo e processi di sostenibilità., 2nd ed. Milano.

Leone, A., Gobattoni, F., Pelorosso, R., Balena, P., 2019. L'uso del suolo agricolo è il fattore chiave per la sicurezza dei territori fragili. Presented at the XXII Conferenza SIU: L'urbanistica italiana di fronte all'Agenda 2030, Bari, Italy, pp. 857–862.

Leone, A., Ripa, M.N., Boccia, L., Lo Porto, A., 2008. Phosphorus export from agricultural land: a simple approach. Biosyst. Eng. 101, 270–280. https://doi.org/10.1016/j.biosystemseng.2008.07.005

Li, J., 2021. Satellite Remote Sensing Technologies, Space Science and Technologies. Springer Singapore, Singapore. https://doi.org/10.1007/978-981-15-4871-0

Li, L., Goodchild, M.F., Xu, B., 2013. Spatial, temporal, and socioeconomic patterns in the use of twitter and flickr. Cartogr. Geogr. Inf. Sci. 40, 61–77. https://doi.org/10.1080/15230406.2013.777139

Li, X., Chen, W.Y., Sanesi, G., Lafortezza, R., 2019. Remote Sensing in Urban Forestry: Recent Applications and Future Directions. Remote Sens. 11, 1144. https://doi.org/10.3390/rs11101144

Liaw, A., Wiener, M., 2002. Classification and Regression by randomForest 2.

Lim, J., Kim, K.-M., Jin, R., 2019. Tree Species Classification Using Hyperion and Sentinel-2 Data with Machine Learning in South Korea and China. ISPRS Int. J. Geo-Inf. 8, 150. https://doi.org/10.3390/ijgi8030150

List of sites of Community importance [WWW Document], 2024. URL https://eur-lex.europa.eu/eli/dec_impl/2024/424/oj (accessed 5.3.24).

Liu, M., Yu, T., Gu, X., Sun, Z., Yang, J., Zhang, Z., Mi, X., Cao, W., Li, J., 2020. The Impact of Spatial Resolution on the Classification of Vegetation Types in Highly Fragmented Planting Areas Based on Unmanned Aerial Vehicle Hyperspectral Images. Remote Sens. 12, 146. https://doi.org/10.3390/rs12010146

Liu, P., Ren, C., Wang, Z., Jia, M., Yu, W., Ren, H., Xia, C., 2024. Evaluating the Potential of Sentinel-2 Time Series Imagery and Machine Learning for Tree Species Classification in a Mountainous Forest. Remote Sens. 16, 293. https://doi.org/10.3390/rs16020293

Loizzo, R., Guarini, R., Longo, F., Scopa, T., Formaro, R., Facchinetti, C., Varacalli, G., 2018. Prisma: The Italian Hyperspectral Mission, in: IGARSS 2018 - 2018 IEEE International Geoscience and Remote Sensing Symposium. Presented at the IGARSS 2018 - 2018 IEEE International Geoscience and Remote Sensing Symposium, IEEE, Valencia, pp. 175–178. https://doi.org/10.1109/IGARSS.2018.8518512

Lou, C., Al-qaness, M.A.A., AL-Alimi, D., Dahou, A., Abd Elaziz, M., Abualigah, L., Ewees, A.A., 2024. Land use/land cover (LULC) classification using hyperspectral images: a review. Geo-Spat. Inf. Sci. 27, 1–42. https://doi.org/10.1080/10095020.2024.2332638

Lv, W., Wang, X., 2020. Overview of Hyperspectral Image Classification. J. Sens. 2020, 1–13. https://doi.org/10.1155/2020/4817234

Lyngdoh, R.B., Sahadevan, A.S., Ahmad, T., Rathore, P.S., Mishra, M., Gupta, P.K., Misra, A., 2021. AVHYAS: A Free and Open Source QGIS Plugin for Advanced Hyperspectral Image Analysis.

Ma, L., Liu, Y., Zhang, X., Ye, Y., Yin, G., Johnson, B.A., 2019. Deep learning in remote sensing applications: A meta-analysis and review. ISPRS J. Photogramm. Remote Sens. 152, 166–177. https://doi.org/10.1016/j.isprsjprs.2019.04.015

Makantasis, K., Karantzalos, K., Doulamis, A., Doulamis, N., 2015. Deep supervised learning for hyperspectral data classification through convolutional neural networks, in: 2015 IEEE International Geoscience and Remote Sensing Symposium (IGARSS). Presented at the 2015 IEEE International Geoscience and Remote Sensing Symposium (IGARSS), pp. 4959–4962. https://doi.org/10.1109/IGARSS.2015.7326945

Malinowski, R., Lewiński, S., Rybicki, M., Gromny, E., Jenerowicz, M., Krupiński, M., Nowakowski, A., Wojtkowski, C., Krupiński, M., Krätzschmar, E., Schauer, P., 2020. Automated production of a land cover/use map of europe based on sentinel-2 imagery. Remote Sens. 12, 1–27. https://doi.org/10.3390/rs12213523

Malkoç, E., 2024. City-wide assessment of urban tree cover and land-cover changes in Edirne using web-based tools. Int. J. Appl. Earth Obs. Geoinformation 132, 103997. https://doi.org/10.1016/j.jag.2024.103997

Marconi, S., Weinstein, B.G., Zou, S., Bohlman, S.A., Zare, A., Singh, A., Stewart, D., Harmon, I., Steinkraus, A., White, E.P., 2022. Continental-scale hyperspectral tree species classification in the United States National Ecological Observatory Network. Remote Sens. Environ. 282, 113264. https://doi.org/10.1016/j.rse.2022.113264

Martinez-Sanchez, L., See, L., Yordanov, M., Verhegghen, A., Elvekjaer, N., Muraro, D., d'Andrimont, R., van der Velde, M., 2024. Automatic classification of land cover from LUCAS in-situ landscape photos using semantic segmentation and a Random Forest model. Environ. Model. Softw. 172, 105931. https://doi.org/10.1016/j.envsoft.2023.105931

Massey, R., Berner, L.T., Foster, A.C., Goetz, S.J., Vepakomma, U., 2023. Remote Sensing Tools for Monitoring Forests and Tracking Their Dynamics, in: Girona, M.M., Morin, H., Gauthier, S., Bergeron, Y. (Eds.), Boreal Forests in the Face of Climate Change: Sustainable Management. Springer International Publishing, Cham, pp. 637–655. https://doi.org/10.1007/978-3-031-15988-6_26

Matese, A., Toscano, P., Di Gennaro, S.F., Genesio, L., Vaccari, F.P., Primicerio, J., Belli, C., Zaldei, A., Bianconi, R., Gioli, B., 2015. Intercomparison of UAV, Aircraft and Satellite Remote Sensing Platforms for Precision Viticulture. Remote Sens. 7, 2971–2990. https://doi.org/10.3390/rs70302971

Mehta, A., Shukla, S., Rakholia, S., 2021. Vegetation Change Analysis using Normalized Difference Vegetation Index and Land Surface Temperature in Greater Gir Landscape. J. Sci. Res. 65, 01–06. https://doi.org/10.37398/JSR.2021.650301

Melgani, F., Bruzzone, L., 2004. Classification of hyperspectral remote sensing images with support vector machines. IEEE Trans. Geosci. Remote Sens. 42, 1778–1790. https://doi.org/10.1109/TGRS.2004.831865

Ministerial Decree no. 397, 2017. Individuazione delle linee guida per i piani urbani di mobilita' sostenibile - Identification of guidelines for sustainable urban mobility plans.

Ministerial Decree no. 1444, 1968. Standard Urbanistici - Urban planning standards.

Ministro dell'Ambiente e della Tutela del Territorio e del Mare, 2020. Criteri ambientali minimi per il servizio di gestione del verde pubblico e la fornitura di prodotti per la cura del verde.

Mittermeier, R.A., Turner, W.R., Larsen, F.W., Brooks, T.M., Gascon, C., 2011. Global Biodiversity Conservation: The Critical Role of Hotspots, in: Zachos, F.E., Habel, J.C. (Eds.), Biodiversity Hotspots: Distribution and Protection of Conservation Priority Areas. Springer, Berlin, Heidelberg, pp. 3–22. https://doi.org/10.1007/978-3-642-20992-5_1

Miyoshi, G.T., Imai, N.N., Tommaselli, A.M.G., Honkavaara, E., 2018. Impact of reduction of radiometric resolution in hyperspectral images acquired over forest field. Int. Arch. Photogramm. Remote Sens. Spat. Inf. Sci. XLII–1, 301–305. https://doi.org/10.5194/isprs-archives-XLII-1-301-2018

Mori, A.S., Lertzman, K.P., Gustafsson, L., 2017. Biodiversity and ecosystem services in forest ecosystems: a research agenda for applied forest ecology. J. Appl. Ecol. 54, 12–27. https://doi.org/10.1111/1365-2664.12669

Morin, E., Herrault, P.-A., Guinard, Y., Grandjean, F., Bech, N., 2022. The promising combination of a remote sensing approach and landscape connectivity modelling at a fine scale in urban planning. Ecol. Indic. 139, 108930. https://doi.org/10.1016/j.ecolind.2022.108930
Mullaney, J., Lucke, T., Trueman, S.J., 2015. A review of benefits and challenges in growing street trees in paved urban environments. Landsc. Urban Plan. 134, 157–166. https://doi.org/10.1016/j.landurbplan.2014.10.013
Müllerová, J., Brůna, J., Bartaloš, T., Dvořák, P., Vítková, M., Pyšek, P., 2017. Timing Is Important: Unmanned Aircraft vs. Satellite Imagery in Plant Invasion Monitoring. Front. Plant Sci. 8, 887. https://doi.org/10.3389/fpls.2017.00887
Naidoo, L., Cho, M.A., Mathieu, R., Asner, G., 2012. Classification of savanna tree species, in the Greater Kruger National Park region, by integrating hyperspectral and LiDAR data in a Random Forest data mining environment. ISPRS J. Photogramm. Remote Sens. 69, 167–179. https://doi.org/10.1016/j.isprsjprs.2012.03.005
Naidu, G., Zuva, T., Sibanda, E.M., 2023. A Review of Evaluation Metrics in Machine Learning Algorithms, in: Silhavy, R., Silhavy, P. (Eds.), Artificial Intelligence Application in Networks and Systems. Springer International Publishing, Cham, pp. 15–25. https://doi.org/10.1007/978-3-031-35314-7_2
NASA, 2019. Surface Biology and Geology (SBG) - NASA Science. URL https://science.nasa.gov/earth-science/decadal-surveys/decadal-sbg/ (accessed 8.25.25).
New urban agenda: H III: Habitat III: Quito 17-20 October 2016, 2017. . Presented at the United Nations Conference on Housing and Sustainable Urban Development, United Nations (UN), Quito, Ecuador.
Nguyen-Van-Anh, V., Hoang-Phi, P., Nguyen-Kim, T., Lam-Dao, N., Vu, T., 2021. The influence of satellite image spatial resolution on mapping land use/land cover: a case study of Ho Chi Minh City, Vietnam. IOP Conf. Ser. Earth Environ. Sci. 652, 012002. https://doi.org/10.1088/1755-1315/652/1/012002

Nieke, J., Despoisse, L., Gabriele, A., Weber, H., Strese, H., Ghasemi, N., Gascon, F., Alonso, K., Boccia, V., Tsonevska, B., Choukroun, P., Ottavianelli, G., Celesti, M., 2023. The copernicus hyperspectral imaging mission for the environment (CHIME): an overview of its mission, system and planning status, in: Sensors, Systems, and Next-Generation Satellites XXVII. Presented at the Sensors, Systems, and Next-Generation Satellites XXVII, SPIE, pp. 21–40. https://doi.org/10.1117/12.2679977

Nowak, D.J., Hirabayashi, S., Bodine, A., Greenfield, E., 2014. Tree and forest effects on air quality and human health in the United States. Environ. Pollut. 193, 119–129. https://doi.org/10.1016/j.envpol.2014.05.028

OSgeo, 2023. QGIS Geographic Information System. QGIS Association.

Pallotta, E., Boccia, L., Rossi, C.M., Ripa, M.N., 2022. Forest Dynamic in the Italian Apennines. Appl. Sci. Switz. 12. https://doi.org/10.3390/app12052474

Palsson, B., Sigurdsson, J., Sveinsson, J.R., Ulfarsson, M.O., 2018. Hyperspectral Unmixing Using a Neural Network Autoencoder. IEEE Access 6, 25646–25656. https://doi.org/10.1109/ACCESS.2018.2818280

Pan, Y., Birdsey, R.A., Phillips, O.L., Houghton, R.A., Fang, J., Kauppi, P.E., Keith, H., Kurz, W.A., Ito, A., Lewis, S.L., Nabuurs, G.-J., Shvidenko, A., Hashimoto, S., Lerink, B., Schepaschenko, D., Castanho, A., Murdiyarso, D., 2024. The enduring world forest carbon sink. Nature 631, 563–569. https://doi.org/10.1038/s41586-024-07602-x

Pandey, P.C., Balzter, H., Srivastava, P.K., Petropoulos, G.P., Bhattacharya, B., 2020. Future perspectives and challenges in hyperspectral remote sensing, in: Hyperspectral Remote Sensing. Elsevier, pp. 429–439. https://doi.org/10.1016/B978-0-08-102894-0.00021-8

Pandian, J.A., Gupta, S.Kr., Kumar, R., Hazra, S., Kanchanadevi, K., 2022. Classification of Land Cover Hyperspectral Images Using Deep Convolutional Neural Network, in: Shaw, R.N., Das, S., Piuri, V., Bianchini, M. (Eds.), Advanced Computing and

Intelligent Technologies, Lecture Notes in Electrical Engineering. Springer Nature Singapore, Singapore, pp. 89–97. https://doi.org/10.1007/978-981-19-2980-9_8
Paoletti, M.E., Haut, J.M., Plaza, J., Plaza, A., 2019. Deep learning classifiers for hyperspectral imaging: A review. ISPRS J. Photogramm. Remote Sens. 158, 279–317. https://doi.org/10.1016/j.isprsjprs.2019.09.006
Pelorosso, R., Leone, A., Boccia, L., 2009. Land cover and land use change in the Italian central Apennines: A comparison of assessment methods. Appl. Geogr. 29, 35–48. https://doi.org/10.1016/j.apgeog.2008.07.003
Pepe, M., Pompilio, L., Gioli, B., Busetto, L., Boschetti, M., 2020. Detection and Classification of Non-Photosynthetic Vegetation from PRISMA Hyperspectral Data in Croplands. Remote Sens. 12, 3903. https://doi.org/10.3390/rs12233903
Perko, R., Raggam, H., Schardt, M., Roth, P.M., 2018. Very High Resolution Mapping with the Pléiades Satellite Constellation. Am. J. Remote Sens. 6, 89–99. https://doi.org/10.11648/j.ajrs.20180602.14
Perretta, M., Delogu, G., Funsten, C., Patriarca, A., Caputi, E., Boccia, L., 2024. Testing the Impact of Pansharpening Using PRISMA Hyperspectral Data: A Case Study Classifying Urban Trees in Naples, Italy. Remote Sens. 16, 3730. https://doi.org/10.3390/rs16193730
Persson, M., Lindberg, E., Reese, H., 2018. Tree Species Classification with Multi-Temporal Sentinel-2 Data. Remote Sens. 10, 1794. https://doi.org/10.3390/rs10111794
Petroncelli, E., 2005. Pianificazione territoriale. Principi e fondamenti.
Pfeifer, M., Disney, M., Quaife, T., Marchant, R., 2012. Terrestrial ecosystems from space: a review of earth observation products for macroecology applications. Glob. Ecol. Biogeogr. 21, 603–624. https://doi.org/10.1111/j.1466-8238.2011.00712.x
Phiri, D., Simwanda, M., Salekin, S., Nyirenda, V.R., Murayama, Y., Ranagalage, M., 2020. Sentinel-2 Data for Land Cover/Use Mapping: A Review. Remote Sens. 12, 2291. https://doi.org/10.3390/rs12142291

Pignatti Sandro, 2003. Guida alla classificazione della vegetazione forestale. INFC2003 – Inventario Nazionale delle Foreste e dei Serbatoi Forestali di Carbonio. - Guide to the classification of forest vegetation. INFC2003 – Second National Inventory of Forests and Forest Carbon Reservoirs. Trento.

Pleniou, M., Koutsias, N., 2025. The role of spectral vs spatial resolution of satellite data on the accuracy of mapping unburned vegetation within fire scar perimeters. Sci. Remote Sens. 11, 100241. https://doi.org/10.1016/j.srs.2025.100241

Pretzsch, H., Moser-Reischl, A., Rahman, M.A., Pauleit, S., Rötzer, T., 2023. Towards sustainable management of the stock and ecosystem services of urban trees. From theory to model and application. Trees 37, 177–196. https://doi.org/10.1007/s00468-021-02100-3

PRISMA, 2020. PRISMA Products Specification [WWW Document]. PRISMA Prod. Specif. URL https://prisma.asi.it/missionselect/docs/ (accessed 7.30.24).

PRISMA Algorithm Theoretical Basis Document (ATBD) [WWW Document], 2020. URL https://prisma.asi.it/missionselect/docs/ (accessed 7.30.24).

Pu, R., 2021. Mapping Tree Species Using Advanced Remote Sensing Technologies: A State-of-the-Art Review and Perspective. J. Remote Sens. 2021. https://doi.org/10.34133/2021/9812624

QField App, 2023. QField App [WWW Document]. URL https://qfield.org/ (accessed 11.4.24).

Qian, S.-E., 2021. Hyperspectral Satellites, Evolution, and Development History. IEEE J. Sel. Top. Appl. Earth Obs. Remote Sens. 14, 7032–7056. https://doi.org/10.1109/JSTARS.2021.3090256

R Core Team, 2021. R Core Team. R Core Team (2021). R: A language and environment for statistical computing. R Foundation for Statistical Computing.

Rana, P., Prieur, J.-F., Budei, B.C., St-Onge, B., 2018. Towards a Generalized Method for Tree Species Classification Using Multispectral Airborne Laser Scanning in Ontario, Canada, in: IGARSS 2018 - 2018 IEEE International Geoscience and Remote

Sensing Symposium. Presented at the IGARSS 2018 - 2018 IEEE International Geoscience and Remote Sensing Symposium, IEEE, Valencia, pp. 5–8749. https://doi.org/10.1109/IGARSS.2018.8517991

Randin, C.F., Ashcroft, M.B., Bolliger, J., Cavender-Bares, J., Coops, N.C., Dullinger, S., Dirnböck, T., Eckert, S., Ellis, E., Fernández, N., Giuliani, G., Guisan, A., Jetz, W., Joost, S., Karger, D., Lembrechts, J., Lenoir, J., Luoto, M., Morin, X., Price, B., Rocchini, D., Schaepman, M., Schmid, B., Verburg, P., Wilson, A., Woodcock, P., Yoccoz, N., Payne, D., 2020. Monitoring biodiversity in the Anthropocene using remote sensing in species distribution models. Remote Sens. Environ. 239. https://doi.org/10.1016/j.rse.2019.111626

Rapacciuolo, G., Young, A., Johnson, R., 2021. Deriving indicators of biodiversity change from unstructured community-contributed data. Oikos 130, 1225–1239. https://doi.org/10.1111/oik.08215

Rast, M., Painter, T.H., 2019. Earth Observation Imaging Spectroscopy for Terrestrial Systems: An Overview of Its History, Techniques, and Applications of Its Missions. Surv. Geophys. 40, 303–331. https://doi.org/10.1007/s10712-019-09517-z

Rasti, B., Hong, D., Hang, R., Ghamisi, P., Kang, X., Chanussot, J., Benediktsson, J.A., 2020. Feature Extraction for Hyperspectral Imagery: The Evolution From Shallow to Deep: Overview and Toolbox. IEEE Geosci. Remote Sens. Mag. 8, 60–88. https://doi.org/10.1109/MGRS.2020.2979764

Recanatesi, F., Giuliani, C., Piccinno, M., Cucca, B., Rossi, C., Ripa, M., 2020. An innovative environmental risk assessment approach to a Mediterranean coastal forest: the Presidential Estate of Castelporziano (Rome) case study. Ann. Silvic. Res. 44. https://doi.org/10.12899/asr-1884

Recanatesi, F., Giuliani, C., Rossi, C.M., Ripa, M.N., 2019. A Remote Sensing-Assisted Risk Rating Study to Monitor Pinewood Forest Decline: The Study Case of the Castelporziano State Nature Reserve (Rome), in: Smart Innovation, Systems and

Technologies. Springer International Publishing, Cham, pp. 68–75. https://doi.org/10.1007/978-3-319-92099-3_9
Richards, J.A., Jia, X., 2006. Remote sensing digital image analysis: an introduction, 4. ed. ed. Springer, Berlin Heidelberg.
Rogers, J.A., Robertson, K.M., Hawbaker, T.J., Sousa, D.J., 2024. Classifying Plant Communities in the North American Coastal Plain With PRISMA Spaceborne Hyperspectral Imagery and the Spectral Mixture Residual. J. Geophys. Res. Biogeosciences 129, e2024JG008217. https://doi.org/10.1029/2024JG008217
Rosentreter, J., Hagensieker, R., Okujeni, A., Roscher, R., Wagner, P.D., Waske, B., 2017. Subpixel Mapping of Urban Areas Using EnMAP Data and Multioutput Support Vector Regression. IEEE J. Sel. Top. Appl. Earth Obs. Remote Sens. 10, 1938–1948. https://doi.org/10.1109/JSTARS.2017.2652726
Rossi, L., Menconi, M.E., Grohmann, D., Brunori, A., Nowak, D.J., 2022. Urban Planning Insights from Tree Inventories and Their Regulating Ecosystem Services Assessment. Sustainability 14, 1684. https://doi.org/10.3390/su14031684
Rubel, F., Brugger, K., Haslinger, K., Auer, I., 2017. The climate of the European Alps: Shift of very high resolution Köppen-Geiger climate zones 1800–2100. Meteorol. Z. 115–125. https://doi.org/10.1127/metz/2016/0816
Sánchez, S., Plaza, A., 2014. Fast determination of the number of endmembers for real-time hyperspectral unmixing on GPUs. J. Real-Time Image Process. 9, 397–405. https://doi.org/10.1007/s11554-012-0276-3
Santarsiero, V., Nolè, G., Lanorte, A., Tucci, B., Cillis, G., Murgante, B., 2022. Remote Sensing and Spatial Analysis for Land-Take Assessment in Basilicata Region (Southern Italy). Remote Sens. 14, 1692. https://doi.org/10.3390/rs14071692
Sarath, T., 2014. A Study on Hyperspectral Remote Sensing Classifications. Int. J. Comput. Appl.
Satalino, G., Balenzano, A., Lovergine, F., Albertini, C., Palmisano, D., Mattia, F., Ruggieri, S., Garofalo, P., Rinaldi, M., Iacobellis, V., Gioia, A., Impedovo, D., Nardella, L., Di Cataldo, M., Noviello, N., Guarini, R., Sacco, P., Virelli, M., Tapete, D., 2024. Earth

Observation for the Early Forecast of Irrigation Needs, in: IGARSS 2024 - 2024 IEEE International Geoscience and Remote Sensing Symposium. Presented at the IGARSS 2024 - 2024 IEEE International Geoscience and Remote Sensing Symposium, pp. 4912–4915. https://doi.org/10.1109/IGARSS53475.2024.10642240

Sawant, S., Prabukumar, M., 2020. A survey of band selection techniques for hyperspectral image classification. J. Spectr. Imaging a5. https://doi.org/10.1255/jsi.2020.a5

Scheffler, D., Hollstein, A., Diedrich, H., Segl, K., Hostert, P., 2017. AROSICS: An Automated and Robust Open-Source Image Co-Registration Software for Multi-Sensor Satellite Data. Remote Sens. 9, 676. https://doi.org/10.3390/rs9070676

Schiavon, E., Taramelli, A., Tornato, A., Lee, C.M., Luvall, J.C., Schollaert Uz, S., Townsend, P.A., Cima, V., Geraldini, S., Nguyen Xuan, A., Valentini, E., Miller, C.E., 2023. Maximizing Societal Benefit Across Multiple Hyperspectral Earth Observation Missions: A User Needs Approach. J. Geophys. Res. Biogeosciences 128, e2023JG007569. https://doi.org/10.1029/2023JG007569

Sciortino, M., De Felice, M., De Cecco, L., Borfecchia, F., 2020. Remote sensing for monitoring and mapping Land Productivity in Italy: A rapid assessment methodology. https://doi.org/10.1016/j.catena.2019.104375

Sen, O., Keles, H.Y., 2020. On the Evaluation of CNN Models in Remote-Sensing Scene Classification Domain. PFG – J. Photogramm. Remote Sens. Geoinformation Sci. 88, 477–492. https://doi.org/10.1007/s41064-020-00129-6

Shahtahmassebi, A.R., Li, C., Fan, Y., Wu, Y., lin, Y., Gan, M., Wang, K., Malik, A., Blackburn, G.A., 2021. Remote sensing of urban green spaces: A review. Urban For. Urban Green. 57, 126946. https://doi.org/10.1016/j.ufug.2020.126946

Shaik, R., Periasamy, S., Zeng, W., 2023. Potential Assessment of PRISMA Hyperspectral Imagery for Remote Sensing Applications. Remote Sens. 15, 1378. https://doi.org/10.3390/rs15051378

Shaik, R.U., Laneve, G., Fusilli, L., 2022. An Automatic Procedure for Forest Fire Fuel Mapping Using Hyperspectral (PRISMA) Imagery: A Semi-Supervised Classification Approach. Remote Sens. 14. https://doi.org/10.3390/rs14051264

Signoroni, A., Savardi, M., Baronio, A., Benini, S., 2019. Deep Learning Meets Hyperspectral Image Analysis: A Multidisciplinary Review. J. Imaging 5, 52. https://doi.org/10.3390/jimaging5050052

Siviglia, M., 2023. Biodiversità nel Parco Regionale delle Serre Calabresi. Territorio, siti naturali, graniti, cave, piante arboree, flora, funghi. Rubbettino.

Sothe, C., De Almeida, C.M., Schimalski, M.B., La Rosa, L.E.C., Castro, J.D.B., Feitosa, R.Q., Dalponte, M., Lima, C.L., Liesenberg, V., Miyoshi, G.T., Tommaselli, A.M.G., 2020. Comparative performance of convolutional neural network weighted and conventional support vector machine and random forest for classifying tree species using hyperspectral and photogrammetric data. GIScience Remote Sens. 57, 369–394. https://doi.org/10.1080/15481603.2020.1712102

Sozzi, M., Kayad, A., Gobbo, S., Cogato, A., Sartori, L., Marinello, F., 2021. Economic Comparison of Satellite, Plane and UAV-Acquired NDVI Images for Site-Specific Nitrogen Application: Observations from Italy. Agronomy 11, 2098. https://doi.org/10.3390/agronomy11112098

Spiller, D., Ansalone, L., Carotenuto, F., Mathieu, P.P., 2021. Crop Type Mapping Using Prisma Hyperspectral Images and One-Dimensional Convolutional Neural Network, in: 2021 IEEE International Geoscience and Remote Sensing Symposium IGARSS. Presented at the IGARSS 2021 - 2021 IEEE International Geoscience and Remote Sensing Symposium, IEEE, Brussels, Belgium, pp. 8166–8169. https://doi.org/10.1109/IGARSS47720.2021.9554175

Stehman, S.V., Foody, G.M., 2019. Key issues in rigorous accuracy assessment of land cover products. Remote Sens. Environ. 231, 111199. https://doi.org/10.1016/j.rse.2019.05.018

Storch, T., Honold, H.-P., Chabrillat, S., Habermeyer, M., Tucker, P., Brell, M., Ohndorf, A., Wirth, K., Betz, M., Kuchler, M., Mühle, H., Carmona, E., Baur, S., Mücke, M., Löw, S., Schulze, D., Zimmermann, S., Lenzen, C., Wiesner, S., Aida, S., Kahle, R., Willburger, P., Hartung, S., Dietrich, D., Plesia, N., Tegler, M., Schork, K., Alonso, K., Marshall, D., Gerasch, B., Schwind, P., Pato, M., Schneider, M., de los Reyes, R., Langheinrich, M., Wenzel, J., Bachmann, M., Holzwarth, S., Pinnel, N., Guanter, L., Segl, K., Scheffler, D., Foerster, S., Bohn, N., Bracher, A., Soppa, M.A., Gascon, F., Green, R., Kokaly, R., Moreno, J., Ong, C., Sornig, M., Wernitz, R., Bagschik, K., Reintsema, D., La Porta, L., Schickling, A., Fischer, S., 2023. The EnMAP imaging spectroscopy mission towards operations. Remote Sens. Environ. 294, 113632. https://doi.org/10.1016/j.rse.2023.113632

Survey, U.S.G., 2024. Landsat Next (No. 2024–3005), Fact Sheet. U.S. Geological Survey. https://doi.org/10.3133/fs20243005

Sustainable Cities and Communities - Goal 11 [WWW Document], 2015. . U. N. U. N. Sustain. Dev. Goals. URL https://sdgs.un.org/goals/goal11 (accessed 8.1.24).

Tagliabue, G., Boschetti, M., Bramati, G., Candiani, G., Colombo, R., Nutini, F., Pompilio, L., Rivera-Caicedo, J.P., Rossi, M., Rossini, M., Verrelst, J., Panigada, C., 2022. Hybrid retrieval of crop traits from multi-temporal PRISMA hyperspectral imagery. ISPRS J. Photogramm. Remote Sens. 187, 362–377. https://doi.org/10.1016/j.isprsjprs.2022.03.014

Tanoori, G., Soltani, A., Modiri, A., 2024. Predicting Urban Land Use and Mitigating Land Surface Temperature: Exploring the Role of Urban Configuration with Convolutional Neural Networks. J. Urban Plan. Dev. 150, 04024029. https://doi.org/10.1061/JUPDDM.UPENG-5010

Tassi, A., Vizzari, M., 2020. Object-Oriented LULC Classification in Google Earth Engine Combining SNIC, GLCM, and Machine Learning Algorithms. Remote Sens. 12, 3776. https://doi.org/10.3390/rs12223776

Telesca, L., Lovallo, M., Cardettini, G., Aromando, A., Abate, N., Proto, M., Loperte, A., Masini, N., Lasaponara, R., 2023. Urban and

Peri-Urban Vegetation Monitoring Using Satellite MODIS NDVI Time Series, Singular Spectrum Analysis, and Fisher–Shannon Statistical Method. Sustainability 15, 11039. https://doi.org/10.3390/su151411039

Thenkabail, P.S., Enclona, E.A., Ashton, M.S., Legg, C., De Dieu, M.J., 2004. Hyperion, IKONOS, ALI, and ETM+ sensors in the study of African rainforests. Remote Sens. Environ. 90, 23–43. https://doi.org/10.1016/j.rse.2003.11.018

Thenkabail, P.S., Teluguntla, P., Gumma, M.K., Dheeravath, V., 2015. Hyperspectral remote sensing for terrestrial applications. Environ. Monit. Assess. 201–233.

Thomlinson, J.R., Bolstad, P.V., Cohen, W.B., 1999. Coordinating Methodologies for Scaling Landcover Classifications from Site-Specific to Global: Steps toward Validating Global Map Products. Remote Sens. Environ. 70, 16–28. https://doi.org/10.1016/S0034-4257(99)00055-3

Thompson, E., Herian, M., Rosenbaum, D., 2021. The Economic Footprint and Quality-of-Life Benefits of Urban Forestry in the United States. University of Nebrasca - Lincoln.

Townshend, J.R., 1994. Global data sets for land applications from the advanced very high resolution radiometer: An introduction. Int. J. Remote Sens. 15, 3319–3332. https://doi.org/10.1080/01431169408954333

Transforming our world: the 2030 Agenda for Sustainable Development, 2015.

Tripathi, P., Garg, R.D., 2021. Feature extraction of desis and prisma hyperspectral remote sensing datasets for geological applications. Presented at the International Archives of the Photogrammetry, Remote Sensing and Spatial Information Sciences - ISPRS Archives, pp. 169–173. https://doi.org/10.5194/isprs-archives-XLIV-M-3-2021-169-2021

UNEP (Ed.), 2019. Global Environment Outlook – GEO-6: Summary for Policymakers:, 1st ed. Cambridge University Press. https://doi.org/10.1017/9781108639217

Ungar, S.G., Pearlman, J.S., Mendenhall, J.A., Reuter, D., 2003. Overview of the Earth Observing One (EO-1) mission. IEEE Trans. Geosci. Remote Sens. 41, 1149–1159. https://doi.org/10.1109/TGRS.2003.815999

United Nations, 2019. World Urbanization Prospects: The 2018 Revision - United Nations Department of Economic and Social Affairs. United Nations. https://doi.org/10.18356/b9e995fe-en

UNITED NATIONS, E.C.F.E., 2021. Sustainable Urban and Peri-urban Forestry: an Integrative and Inclusive Nature-Based Solution for Green Recovery and Sustainable, Healthy and Resilient Cities. UNECE, Geneva Switzerland.

Urban environment and health - NBFC [WWW Document], n.d. . NBFC. URL https://www.nbfc.it/en/environments (accessed 7.31.24).

Ustin, S.L., Middleton, E.M., 2024. Current and Near-Term Earth-Observing Environmental Satellites, Their Missions, Characteristics, Instruments, and Applications. Sensors 24, 3488. https://doi.org/10.3390/s24113488

Valeri, S., Zavattero, L., Capotorti, G., 2021. Ecological Connectivity in Agricultural Green Infrastructure: Suggested Criteria for Fine Scale Assessment and Planning. Land 10, 807. https://doi.org/10.3390/land10080807

Van Der Linden, S., Rabe, A., Held, M., Jakimow, B., Leitão, P.J., Okujeni, A., Schwieder, M., Suess, S., Hostert, P., 2015. The EnMAP-box-A toolbox and application programming interface for EnMAP data processing. Remote Sens. 7, 11249–11266. https://doi.org/10.3390/rs70911249

van der Velde, M., Goeau, H., Bonnet, P., d'Andrimont, R., Yordanov, M., Affouard, A., Claverie, M., Czucz, B., Elvekjaer, N., Martinez-Sanchez, L., Rotllan-Puig, X., Sima, A., Verhegghen, A., Joly, A., 2023. Pl@ntNet Crops: merging citizen science observations and structured survey data to improve crop recognition for agri-food-environment applications. Environ. Res. Lett. 18. https://doi.org/10.1088/1748-9326/acadf3

Vangi, E., D'amico, G., Francini, S., Giannetti, F., Lasserre, B., Marchetti, M., Chirici, G., 2021. The new hyperspectral satellite prisma: Imagery for forest types discrimination. Sens. Switz. 21, 1–19. https://doi.org/10.3390/s21041182

Vanguri, R., Laneve, G., Hościło, A., 2024. Mapping forest tree species and its biodiversity using EnMAP hyperspectral data along with Sentinel-2 temporal data: An approach of tree species classification and diversity indices. Ecol. Indic. 167, 112671. https://doi.org/10.1016/j.ecolind.2024.112671

Vavassori, A., Oxoli, D., Venuti, G., Brovelli, M.A., Mohamed, A.B.E.A., Moazzam, A., Siciliani de Cumis, M., Sacco, P., Tapete, D., 2024. PRISMA Hyperspectral Satellite Imagery Application to Local Climate Zones Mapping. Int. Arch. Photogramm. Remote Sens. Spat. Inf. Sci. XLVIII-1–2024, 643–648. https://doi.org/10.5194/isprs-archives-XLVIII-1-2024-643-2024

Verde, N., Mallinis, G., Tsakiri-Strati, M., Georgiadis, C., Patias, P., 2018. Assessment of Radiometric Resolution Impact on Remote Sensing Data Classification Accuracy. Remote Sens. 10, 1267. https://doi.org/10.3390/rs10081267

Verde, S., Dell'Acqua, F., Losasso, M., 2024. Environmental Data, Modeling and Digital Simulation for the Evaluation of Climate Adaptation and Mitigation Strategies in the Urban Environment. Sustainability 16, 2179. https://doi.org/10.3390/su16052179

Vihervaara, P., Auvinen, A.-P., Mononen, L., Törmä, M., Ahlroth, P., Anttila, S., Böttcher, K., Forsius, M., Heino, J., Heliölä, J., Koskelainen, M., Kuussaari, M., Meissner, K., Ojala, O., Tuominen, S., Viitasalo, M., Virkkala, R., 2017. How Essential Biodiversity Variables and remote sensing can help national biodiversity monitoring. Glob. Ecol. Conserv. 10, 43–59. https://doi.org/10.1016/j.gecco.2017.01.007

Wang, Y., Zhang, W., Gao, R., Jin, Z., Wang, X., 2021. Recent advances in the application of deep learning methods to forestry. Wood Sci. Technol. 55, 1171–1202. https://doi.org/10.1007/s00226-021-01309-2

Weather data archive [WWW Document], 2024. URL https://www.meteonetwork.eu/it/weather-station/clb110-stazione-meteorologica-di/archive (accessed 11.4.24).

Wegler, M., Kacic, P., Thonfeld, F., Holzwarth, S., Jaggy, N., Gessner, U., Kuenzer, C., 2025. Tree species from space: a new product for Germany based on Sentinel-1 and -2 time series. Int. J. Remote Sens. 0, 1–34. https://doi.org/10.1080/01431161.2025.2530236

Wilson, D.R., Martinez, T.R., 2001. The need for small learning rates on large problems, in: IJCNN'01. International Joint Conference on Neural Networks. Proceedings (Cat. No.01CH37222). Presented at the IJCNN'01. International Joint Conference on Neural Networks. Proceedings (Cat. No.01CH37222), pp. 115–119 vol.1. https://doi.org/10.1109/IJCNN.2001.939002

WMO, 2024. State of the Global Climate 2024 (No. 1368). Geneva, Switzerland.

Wu, X., Xiao, Q., Wen, J., You, D., Hueni, A., 2019. Advances in quantitative remote sensing product validation: Overview and current status. Earth-Sci. Rev. 196, 102875. https://doi.org/10.1016/j.earscirev.2019.102875

Yang, H., Chen, M., Wu, G., Wang, J., Wang, Y., Hong, Z., 2023. Double Deep Q-Network for Hyperspectral Image Band Selection in Land Cover Classification Applications. Remote Sens. 15, 682. https://doi.org/10.3390/rs15030682

Zhang, B., Zhao, L., Zhang, X., 2020. Three-dimensional convolutional neural network model for tree species classification using airborne hyperspectral images. Remote Sens. Environ. 247, 111938. https://doi.org/10.1016/j.rse.2020.111938

Zhang, L., Liu, Q., Lin, H., Sun, H., Chen, S., 2010. The land cover mapping with airborne hyperspectral remote sensing imagery in Yanhe river valley, in: 2010 18th International Conference on Geoinformatics. Presented at the 2010 18th International Conference on Geoinformatics, pp. 1–5. https://doi.org/10.1109/GEOINFORMATICS.2010.5567482

Zhang, W., Li, X., Zhao, L., 2018. Band Priority Index: A Feature Selection Framework for Hyperspectral Imagery. Remote Sens. 10, 1095. https://doi.org/10.3390/rs10071095

Zhong, L., Dai, Z., Fang, P., Cao, Y., Wang, L., 2024. A Review: Tree Species Classification Based on Remote Sensing Data and Classic Deep Learning-Based Methods. Forests 15, 852. https://doi.org/10.3390/f15050852

List of figures

List of tables

List of Acronyms

Acronym	Definition
AI	Artificial Intelligence
ANN	Artificial Neural Network
AROSICS	Automated and Robust Open-Source Image Co-Registration Software
ASI	Italian Space Agency
AVHYAS	Advanced Hyperspectral Data Analysis
CAP	Central Apennines
CEAL	Central-Eastern Alps
CHIME	Copernicus Hyperspectral Imaging Mission
CLC	Corine Land Cover
CNN	Convolutional Neural Network
CP	Castel Porziano
CUAS	Agricultural Land Use Map of Campania Region
Cube_O	PRISMA 234-bands Hyperspectral Cube in Chapter 4
Cube_S	Cube-O subsetted to the ROI in Chapter 4
Cube-O	240-bands PRISMA Hyperspectral Cube in Chapter 2
Cube-R1	Reduced 156-bands hyperspectral cube in Chapter 2
Cube-R1	Reduced 205-bands hyperspectral cube in Chapter 4
Cube-R1_M	Cube-R1_N masked on areas with NDVI > 0.4 in Chapter 4
Cube-R1_N	Cube-R1 normalized in Chapter 4
Cube-R2	Reduced 20-bands hyperspectral cube in Chapter 2
DEM	Digital Elevation Model
DL	Deep Learning
DLR	German Aerospace Center
DN	Digital Numbers

DS_1	First dataset of labeled data in Chapter 4
DS_2	Second dataset of labeled data in Chapter 4
DSM	Digital Surface Model
DTM	Digital Terrain Model
EnMAP	Environmental Mapping and Analysis Program
EO	Earth Observation
ESA	European Space Agency
F1	F1 score
FORCE	Framework for Operational Radiometric Correction for Environmental Monitoring
FOV	Field Of View
GCPs	Ground Control Points
GIS	Geographic Information Systems
GNSS	Global Navigation Satellite System
GPS	Global Positioning System
GSD	Ground Sampling Distance
GTPs	Ground Truth Points
GTs	Ground Truths
HS_DS	Hyperspectral dataset in Chapter 3
HSI	Hyperspectral imagery
HSI_1	HSI with original spatial resolution of 30 m in Chapter 3
HSI_2	HSI with increased spatial resolution of 5 m in Chapter 3
HSI_mask	Mask of the hyperspectral dataset with forested areas in Chapter 3
IFOV	Instantaneous Field Of View
K	Cohen's kappa coefficient
LC	Land Cover
LiDAR	Light Detection And Ranging
LSN	Landsat Next
LU	Land Use
MAT	Matese National Park
ML	Machine Learning
MS	Multispectral
MS_DS	Multispectral Dataset in Chapter 3
N.I.	National Forest Inventory in Chapter 4
NASA	National Aeronautics and Space Administration
NBFC	National Biodiversity Future Center

nDSM	Normalized Difference between the DSM and the DTM
NDVI	Normalized Difference Vegetation Index
NFI	National Forest Inventory in Chapter 5
NIR	Near-InfraRed
NRRP	National Recovery and Resilience Plan
OA	Overall Accuracy
OOB	Out-Of-Bag
OSGeo	Open-Source Geospatial Foundation
PA	Producer's Accuracy
PAN	Panchromatic
PCA	Principal Component Analysis
PRISMA	PRecursore IperSpettrale della Missione Operativa - Hyperspectral Precursor of the Application Mission
RBF	Weighted ensemble of radial basis convolution filters
RF	Random Forest
RFE	Recursive Feature Elimination
ROI	Region Of Interest
RS	Remote Sensing
S2	Sentinel-2
SAC	Special Area of Conservation
SAP	South Apennines
SAR	Synthetic-Aperture Radar
SBG	Surface Biology and Geology
SDG	Sustainable Development Goal
SER	Serre Regional Park
SNR	Signal-to-Noise Ratio
SVM	Support Vector Machine
SWIR	Short-Wavelength InfraRed
T	Single Trial in Chapter 3
TOA	Top Of Atmosphere
UA	User's Accuracy
UAV	Unmanned Aerial Vehicle
UN	United Nations
VHR	Very High Resolution
VNIR	Visible and Near-InfraRed
WMO	World Meteorological Organization